



AMERICAN UNIVERSITY OF BEIRUT

THE INTERPLAY BETWEEN THE LOWER HYBRID  
HEATING AND PLASMA TURBULENCE IN THE  
SCRAPE-OFF LAYER OF THE TORE SUPRA TOKAMAK

by

ALI EL REZA GHULAM ASGHAR

A thesis  
submitted in partial fulfillment of the requirements  
for the degree of Master of Science  
to the Department of Physics  
of the Faculty of Arts and Sciences  
at the American University of Beirut

Beirut, Lebanon  
July 2014

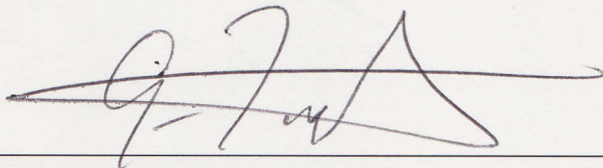
AMERICAN UNIVERSITY OF BEIRUT

THE INTERPLAY BETWEEN THE LOWER HYBRID  
HEATING AND PLASMA TURBULENCE IN THE  
SCRAPE-OFF LAYER OF THE TORE SUPRA TOKAMAK

by

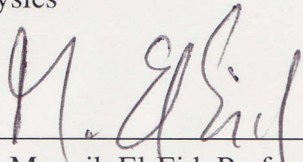
ALI EL REZA GHULAM ASGHAR

Approved by:



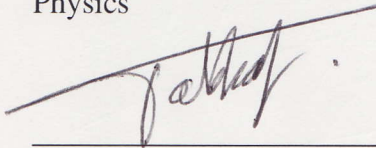
Dr. Ghassan Antar, Associate Professor  
Physics

Advisor



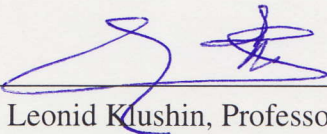
Dr. Mounib El-Eid, Professor  
Physics

Committee Member



Dr. Malek Tabbal, Professor  
Physics

Committee Member



Dr. Leonid Klushin, Professor  
Physics

Committee Member

Date of thesis defense: July 11, 2014

AMERICAN UNIVERSITY OF BEIRUT

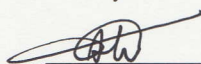
THESIS, DISSERTATION, PROJECT RELEASE FORM

Student Name: ASGHAR ALI EL REZA GHULAM  
Last First Middle

Master's Thesis       Master's Project       Doctoral Dissertation

I authorize the American University of Beirut to: (a) reproduce hard or electronic copies of my thesis, dissertation, or project; (b) include such copies in the archives and digital repositories of the University; and (c) make freely available such copies to third parties for research or educational purposes.

I authorize the American University of Beirut, **three years after the date of submitting my thesis, dissertation, or project**, to: (a) reproduce hard or electronic copies of it; (b) include such copies in the archives and digital repositories of the University; and (c) make freely available such copies to third parties for research or educational purposes.



July 11, 2014

Signature

Date

This form is signed when submitting the thesis, dissertation, or project to the University Libraries

## ACKNOWLEDGEMENTS

My first thanks goes naturally to God, who has been generous to aid me by the hand throughout each moment of my life on its own.

A special thanks to my devoted advisor Prof. Ghassan Antar for his precious teachings, help, encouragement, criticisms; and, above all, his infinite trust in my abilities.

I would also like to thank the members of the committee: Prof. Mounib El-Eid, Prof. Malek Tabbal and Prof. Leonid Klusion; whose profundity, fairness, and professionalism upon evaluating this thesis have been astounding.

A bunch of thanks goes to each and every one of my friends, colleagues, and teachers; who all have supported me and contributed to my study and work in one way or another.

On a personal level, I am ultimately grateful to my family: my siblings, my father, my fiancée, and specially my lovely mother; whose blessings have paved the way for my work to fruit and my dreams to come true.

Finally, though no words would ever live up to as much gratitude as he deserves, I dedicate a humble, sincere thanks to my mentor who, from behind the scenes, has invaluable acted - and still - as a luminous source of hope and inspiration; or, the way I prefer to refer to him, as the 'Right Hand of God'!

# AN ABSTRACT OF THE THESIS OF

Ali El Reza Ghulam Asghar for Master of Science  
Major: Physics

Title: The Interplay between the lower hybrid heating and plasma turbulence in the scrape-off layer of the Tore Supra tokamak

Thermonuclear fusion is one of the most promising options for generating energy in the future. Lower hybrid (LH) current drive waves has proved to be one of the most efficient techniques regarding current drive in plasma fusion devices called tokamaks. LH propagation into closed field lines and mainly the interaction with the edge and the scrape-off layer (SOL) decreases its efficiency in driving current. For this reason, it is important to understand and quantify the interaction between the LH waves and the plasma edge. This interaction is characterized in the SOL by electrostatic probes. Using DFLUC data acquisition resolving frequencies below 0.5 MHz, we characterize the SOL properties in the presence of LH waves. The normalized level of fluctuations is found independent of the power and average density. The intermittent events reflecting convective transport decrease as LH power is increased while remaining unchanged with respect to the plasma density. The convective velocity, detected by the cross-correlation is found to increase with  $P_{LH}$ , but the distribution of turbulence among the scales was not found to be modified. As the core density is increased, the convective velocity and the typical scales did not change. Using the DCEDRE data acquisition, resolving frequencies  $0.1 < f < 100$  MHz, the existence of an ion sound quasi-mode was detected. The propagation velocity as well as the wavelength of this mode were calculated and found in agreement with the theory. Moreover, the amplitude of this mode increased to the square of the LH power clearly showing that it is caused by a Parametric Decay Instability. The level of turbulence was found about 10 times that of the coherent mode and it is decreasing with increasing LH power and is increasing with increasing plasma density.

# CONTENTS

	Page
<b>ACKNOWLEDGEMENTS</b> . . . . .	<b>v</b>
<b>ABSTRACT</b> . . . . .	<b>vi</b>
A. Thesis Outline . . . . .	1
<b>I. Introduction</b> . . . . .	<b>2</b>
A. Thermonuclear Fusion . . . . .	2
B. Tokamaks . . . . .	4
1. Plasma Edge . . . . .	7
2. The Tore Supra Tokamak . . . . .	9
C. Transport and turbulence . . . . .	11
1. Classical transport . . . . .	11
2. Neo-classical transport . . . . .	13
D. Plasma Instabilities . . . . .	14
1. Turbulence . . . . .	18
E. Langmuir probe . . . . .	20
<b>II. Introduction to statistical analysis</b> . . . . .	<b>24</b>
A. Introduction . . . . .	24
B. The Probability Density Function (PDF) . . . . .	25
1. Moments of the PDF . . . . .	27
a. The Mean value . . . . .	27
b. The Variance and the standard deviation . . . . .	27
c. Skewness . . . . .	28
d. Flatness (Kurtosis) . . . . .	29

C. Power spectrum . . . . .	30
D. The Cross-correlation, $Cx_{12}$ . . . . .	33
<b>III. The Lower Hybrid Current Drive (LHCD) . . . . .</b>	<b>36</b>
A. The need for a non-inductive current drive method . . . . .	36
1. The plasma current . . . . .	36
2. Lower hybrid waves . . . . .	39
3. Dispersion Relation . . . . .	40
4. The momenta transfer and parallel velocity . . . . .	43
5. Current Drive efficiency . . . . .	44
6. LHCD efficiency in experiments . . . . .	46
B. The experimental setup for the LHCD . . . . .	47
1. The Lower hybrid Grill . . . . .	47
2. The $n_{\parallel}$ spectrum . . . . .	51
C. Ion Sound waves . . . . .	53
1. Introduction . . . . .	53
2. Equations of motion . . . . .	53
3. Acoustic wave dispersion relation . . . . .	55
D. Parametric Decay Instability . . . . .	57
1. The PDI near the LH frequency . . . . .	59
E. Ion sound waves and PDI in the LH range . . . . .	61
<b>IV. The Interplay between the lower hybrid heating and plasma turbulence in the scrape-off layer of the Tore Supra tokamak . . . . .</b>	<b>63</b>
A. Introduction . . . . .	63
B. The experimental scenarios . . . . .	65
C. Scrape-off layer properties as a function of the LH power . . . . .	66



1. First two order moments dependence on the LH power . . . . .	68
2. The PDF, the skewness and the Flatness behavior with the LH power . . . . .	70
3. The power spectra $S(f)$ as a function of power . . . . .	71
4. The cross-correlation dependence on the LH power . . . . .	75
D. Scrape-off layer properties <i>vs.</i> edge density in the presence of the LH power . . . . .	80
1. First two order moments dependence on $n_{edge}$ . . . . .	81
2. The skewness and the Flatness . . . . .	83
3. The power spectra $S(f)$ as a function of $n_{edge}$ . . . . .	84
4. The cross-correlation dependence on the edge density . . . . .	86
V. Conclusion . . . . .	<b>89</b>

Appendix

## A. Thesis Outline

This thesis is organized in a slightly ‘unusual’ form from a normal thesis. We will present the basic part of our results that will be submitted for publication in a peer reviewed journal. The results are new and are seen **for the first time**. The other part of the results will remain under study where more analysis needs to be performed.

The data analyzed here were taken from the Tore Supra tokamak. More than hundred and fifty discharges were analyzed using different data processing techniques. We studied different behaviors of the SOL plasma parameters in the presence of the LH waves.

The thesis is divided into four main chapters and a conclusion including the future work.

A general introduction is presented in the first chapter focusing on general features that concern our work such as fusion and tokamaks.

In chapter 2 we present an introduction to statistical analysis. We present various statistical techniques that are used in analyzing the data. Basic parametric analysis of the SOL properties is done to investigate modifications that SOL turbulence undergoes in the presence of the LH waves.

In chapter 3, we explain briefly the different aspects of the LHCD and the phenomena that occur during LHCD experiments.

Discussions and **part of the results**, that are to be published as journal articles, are presented in chapter 4. This chapter illustrates the behavior of the SOL properties in the presence of the LH waves. It studies SOL turbulence in the low and high frequency domains as a function of the total power and the average density.

In chapter 5, conclusions and further discussions on the obtained results are presented and future work is proposed.

# CHAPTER I

## INTRODUCTION

### A. Thermonuclear Fusion

The world present reserve of energy resources may hold for only 100 years of oil, 60 years of gas and 200 years of coal. Renewable energy systems such as wind, solar, hydro-electric and biomass are estimated to be able to supply about 30% of demand at best [1]. Besides, human energy requirements are rapidly increasing as the global population rises and nations become more industrialized. With growing concerns over the finite size of the fossil fuel supplies and their contribution to climate change, the need for a clean, safe, carbon-neutral and politically-neutral form of electricity generation is clear. Controlled thermonuclear fusion has long been recognized as an ideal solution.

Fusion is the process that powers the Sun. During the reaction, nuclei fuse together and the mass of the reaction products is less than the mass of the reactants. Due to this small mass loss, as well as Einstein's famous mass-energy equivalence  $E = mc^2$ , energy is released. The fusion of nuclei relies primarily on the nuclear force, which is attractive on very small spatial scales. Nuclei, however, are positively charged and experience mutual electrostatic repulsion. Thus for the fusion reaction to proceed, an electrostatic potential barrier must be overcome.

The size of the potential barrier depends on the reactants. It is conventional to work in terms of a reaction cross-section, which measures the likelihood of a reaction. Some cross-sections for candidate reactions are shown in Fig. 1. The most promising reaction with the highest cross-section is deuterium-tritium (D-T) at an energy of 100 keV. The reaction is as follows,

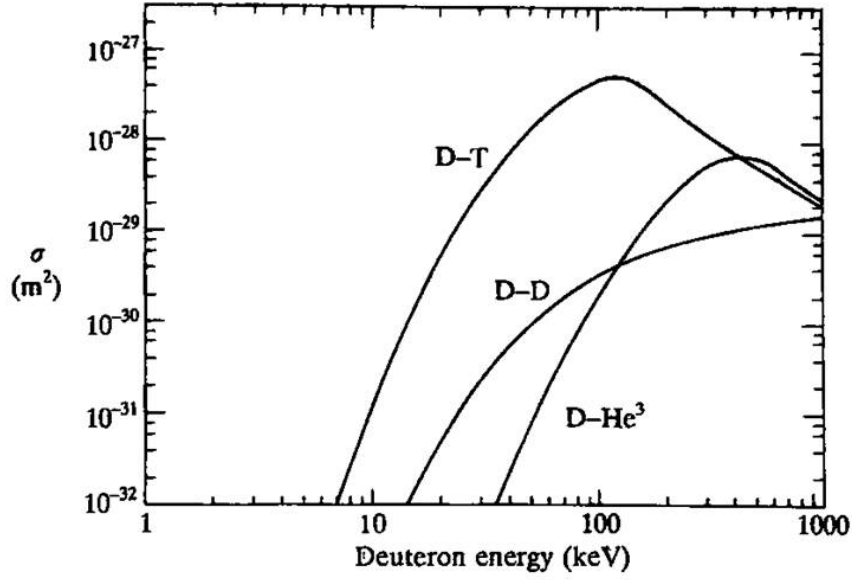
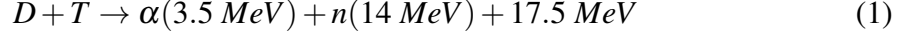


Figure 1: Cross-sections for the reactions D-T, D-D and D-He3. The two D-D reactions have similar cross-sections, the graph gives their sum.



D and T nuclei fuse together creating an alpha particle and a neutron. Moreover, it releases 17.5 MeV of energy. Deuterium and tritium are abundant. Tritium can be created from lithium while deuterium is found in sea water. Hence, deuterium and tritium will be the fuel generation of fusion reactors. It is important to mention that the fusion reaction cannot lead to a catastrophic runaway event and it produces little radioactive waste unlike fission nuclear reactions. In fact, small quantities of short-lived radioactive waste would be produced indirectly due to the activation of the device by neutron bombardment.

Thermonuclear fusion occurs when the fuel is heated sufficiently so that the thermal velocities of the particles are large enough to produce the required fusion reactions. The optimum temperature for D-T thermonuclear fusion is around 30 keV, less than the 100 keV peak in Fig. 1 since a significant fraction of the fusion reactions can occur in the high energy tail of the Maxwellian [2]. At such high temperatures, the fuel will be a fully

ionized plasma.

To produce significant amounts of energy, sufficient amounts of the plasma fuel must be confined for a sufficiently long time, *i.e.*, the product of the density of fusing nuclei  $n$  and the time-scale of confinement  $\tau_e$  must be large. This energy confinement time is defined as  $\tau_e = W/P$ , where  $W$  is the energy content of the plasma and  $P$  is the rate of energy loss. The plasma is said to reach ignition when all energy losses are balanced by alpha particle heating and no external energy inputs are needed to maintain the fusion reaction. The relevant criterion was derived by Lawson and expressed in terms of  $n\tau_e$ . At a temperature of 30 keV, the Lawson criterion for ignition is:

$$n\tau_e > 1.5 \times 10^{20} \text{ sm}^{-3} \quad (2)$$

In general, two approaches, the inertial and the magnetic confinement, are being conducted nowadays trying to satisfy this inequality condition. Inertial confinement uses high powered lasers that rapidly compress small fuel pellets of hydrogen isotopes, aiming to produce extremely high density  $n$  and a short confinement time  $\tau_e$  [see NIF (National Ignition Facility)]. On the other hand, magnetic confinement uses magnetic fields to confine the hot fusion fuel in the form of a plasma, which are electrically conductive and react strongly to electromagnetic fields, at relatively low density  $n$  and for long confinement time  $\tau_e$ .

## **B. Tokamaks**

The tokamak is the most promoted system that is based on the magnetic confinement, for the design of the future fusion reactor. It was originally developed in Russia in the late 1950's. The word 'tokamak' is derived from Russian acronym, "toroidalnaya kamera and magnitnaya katushka", which means "toroidal chamber with magnetic coils".

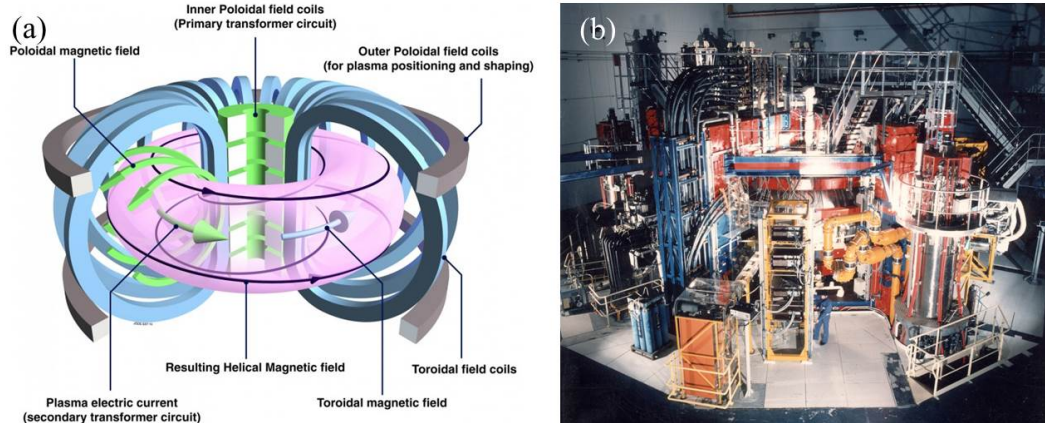


Figure 2: (a), shows the tokamak design. A central solenoid (primary transformer circuit) creates the plasma current indirectly. The poloidal magnetic field is created by the plasma current itself. The toroidal magnets create the a magnetic field in the toroidal direction. The resultant is a Helical magnetic field. The outer poloidal field coils are responsible for the plasma positioning and shaping. (b) shows the Tore Supra tokamak.

In order to control the plasmas motion, external coils, the toroidal electromagnetic coils, surround the torus acquiring the toroidal magnetic field  $B_\phi$ . These magnets are traversed by extremely high current to produce high magnetic field that reaches few Tesla's at the center of the plasma. This way, the plasma are confined in the toroidal direction. Achieving a stable plasma equilibrium, in which the plasma pressure is balanced by the magnetic forces, requires magnetic field lines that move in a helical shape. Such a helical shape can be generated by adding to the toroidal magnetic field  $B_\phi$  a poloidal magnetic field  $B_\theta$ . The poloidal magnetic field encircles the torus in a direction perpendicular to the toroidal field. By Ampere's law, when a wire is traversed by an electric current, a magnetic field is created where it encircles the wire. Plasmas are electrically conductive and could be considered as a wire. When the plasma current traverses the plasma, the poloidal magnetic field  $B_\theta$  is directly created. Consequently,  $B_\theta$  is mainly produced in tokamaks by the plasma current itself. The combination of these two magnetic fields gives rise to magnetic field lines having a helical trajectory shape around the torus.

The plasma pressure is the product of the temperature and the density of the particles. The pressure in a reactor is high due to the fact that the reactivity of the plasma increases with both the plasma density and temperature. The pressure which can be con-

fined is determined by stability considerations and increases with the strength of the magnetic field. However, the magnitude of the toroidal field is limited by technological factors. In laboratory experiments with copper coils both the requirement for cooling and the magnetic forces put a limit on the magnetic field which they can produce. Furthermore, superconducting coils are more competitive to be the toroidal coils due to huge losses from heating in the normal coils which is unacceptable.

There is a loss of superconductivity above a critical magnetic field and this presents another limitation. With present technology it seems likely that the maximum magnetic field at the coils would be limited to around 12 T, but improved conductors with fields up to 16 T are also considered. This maximum toroidal field appears at the inboard side of the toroidal field coil. Since the toroidal magnetic field is inversely proportional to the major radius the resulting field at the center of the plasma would be around 6-8 T. The toroidal fields in present large tokamaks are somewhat lower than this value.

Another limitation arises for the superconducting coils where losses start above a critical magnetic field. Nowadays, magnetic fields are limited to be at maximum 12 Tesla. More recent improvements have increased this limit to about 16 T. The toroidal magnetic field is inversely proportional to the major radius. Hence, the resulting field at the plasma center might reach around 6-8 T. An 8 T magnetic field was achieved at several tokamaks as in the ALCATOR C-Mod located in the USA and the FTU (Frascati Tokamak Upgrade) tokamak which is located in Italy. On the other hand, the toroidal magnetic field at the Tore Supra tokamak, located in France, record a 4.2 T magnetic field strength.

The plasma pressure, for a given  $B_\phi$ , increase with the plasma current up to a certain critical value. The poloidal field  $B_\theta$  resulting from the plasma current is smaller than  $B_\phi$  by an order of magnitude.

The plasma current is usually driven in tokamaks by a central solenoid (primary transformer circuit in Fig. 2(a)) located at the center of the torus. A linearly increasing current traversing the solenoid creates a variable magnetic field with lines in the poloidal

trajectory as seen in Fig. 1. Consequently, this field induces a current in the conducting plasmas. However, a non-inductive method is discovered to generate the current in the plasma non-inductively. More will be discussed later on.

The shape and the position of the plasma are controlled by additional toroidal currents. These currents are driven by the outer poloidal magnets which are situated for the aim of the plasma positioning and shaping.

In order to reach fusion reaction, plasmas must be heated to high temperatures in the order of 10 keV. The ohmic heating, that is due to interaction between plasma particles, heats the plasmas to few keV but then this heating drops rapidly due to energy losses. So, external heating is needed. Several methods are used for heating in today's tokamaks such as the Ion cyclotron resonance heating (ICRH), the Electron cyclotron resonance heating (ECRH) and the Neutral beam injection (NBI) and other techniques.

### ***1. Plasma Edge***

The typical plasma densities in tokamaks nowadays are in the range of  $10^{19} - 10^{20} \text{ m}^{-3}$ , which is less than the atmosphere by a factor of  $10^6$ . Plasmas are contained in a vacuum vessel with low background pressures must be maintained to minimize impurities. Impurities in plasmas allow losses due to radiation. The restriction of their entry into the plasma therefore plays a fundamental role in the successful operation of tokamaks. To separate the plasma from the vacuum vessel, there are two common techniques that are widely used. The first is known as the "limiter" configuration which defines an outer boundary of the plasma with a material limiter as shown in Fig. 3(a). The second is to keep the particles away from the vacuum vessel by modifying the magnetic field shape to produce a magnetic divertor Fig. 3(b). The area between the Last closed flux surface (LCFS), or separatrix, and the vacuum vessel wall is known as the scrap-off layer (SOL) where magnetic field lines are open in contrast to the closed field lines in the confinement



zone.

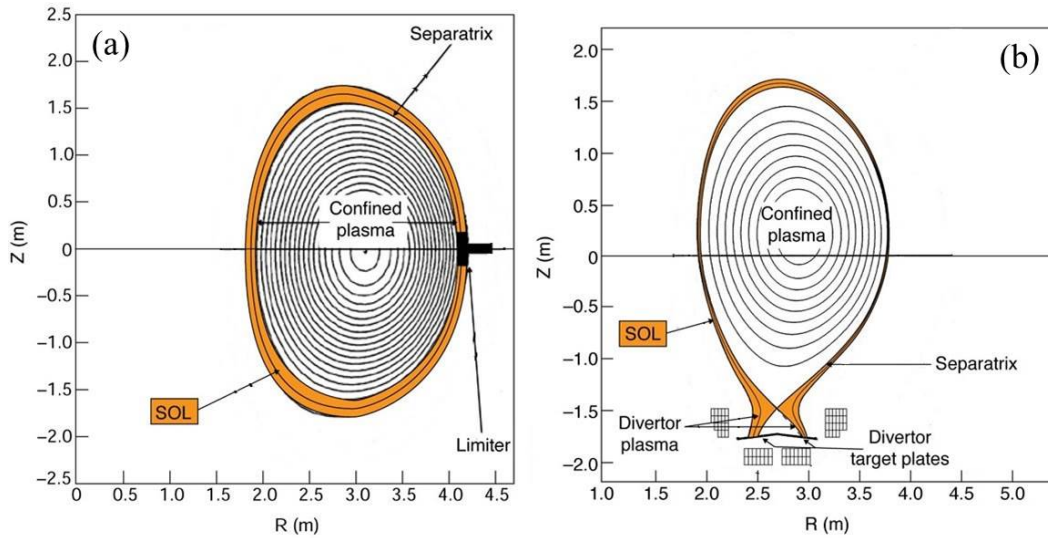


Figure 3: (a) shows the limiter configuration of the JET tokamak, while (b) represents the new JET configuration after the divertor installation. The Separatrix defines the last closed flux surface (LCFS) and eventually the plasma edge. The shots are plotted in the R-Z plane where R is the major radius and Z is the elevation.

The LCFS is commonly used to define the plasma edge. The edge region plays an important role in understanding the whole plasma confinement. For instance, in several tokamaks, there are two main confinement regimes: the L-mode (low confinement) and the H-mode (high confinement). Certain conditions on the operations improve the confinement from the L- mode to the H-mode. So, large temperature and density gradients build up near the plasma edge. This is what is known as the transport barriers. The H-mode is usually accompanied by edge gradients which lead to relaxation process, known as the edge-localized mode (ELM). The latter can cause damage to the device due to intense heat loads [3, 2]. The ELM is a minor disruptive instability occurring in the edge region of a tokamak due to the quasi-periodic relaxation of a transport barrier previously formed during an L-H transition. It was first observed in the ASDEX tokamak in 1981 [4].

The ITER tokamak was designed to achieve ignition in H-mode and many ELM mitigation techniques are proposed. An ignited device operating in L-mode would be much larger and therefore more expensive.

## 2. *The Tore Supra Tokamak*

The Tore Supra Tokamak, which operates in L-mode, shown in Fig. 4 is situated at the nuclear center of Cadarache, France. Its name comes from the two words torus and superconductor. It is the first of the largest tokamaks in the world that has superconducting toroidal magnets. This type of magnets allows for the creation of a strong permanent toroidal magnetic field. Tore Supra started operation in 1988. In 2003, a new record was achieved for the longest plasma duration time for a tokamak. It recorded 6 minutes and 30 seconds with over 1000 MJ of injected and extracted energy. Tore Supra is mainly dedicated to the study of physics and technology to produce long lasting plasmas. It has been instrumental in investigating the active cooling of materials that face the plasma. These facts are vital for the upcoming ITER tokamak.

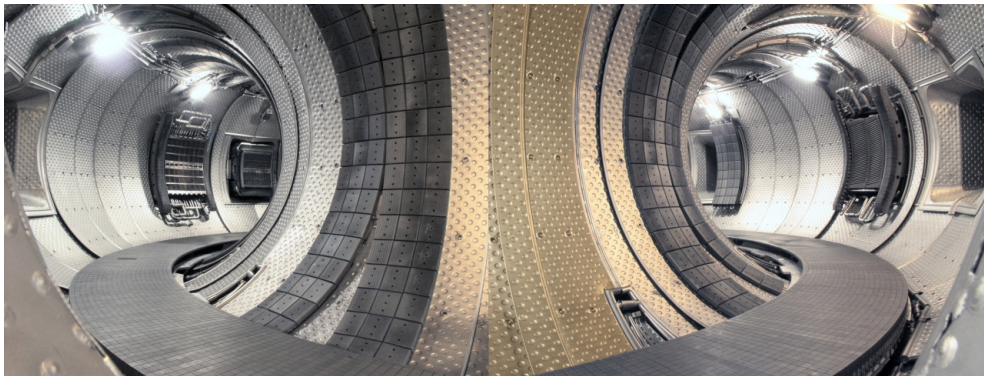


Figure 4: An inside view of the Tore Supra tokamak torus.

With a large radius of 2.4 m (from the center of the torus to the center of the plasma) and a minor radius of 0.7 m (the inner radius of the torus), Tore Supra is considered one of the largest tokamaks in the world. The superconducting toroidal magnets, the actively cooled plasma facing components, and long pulse operations are its main features of.

The superconducting magnets are cooled by super-fluid helium at 1.8 K. It can generate strong permanent toroidal magnetic field that can reach 4.2 T at the center of the plasma. ITER will also have superconducting magnets.

The actively cooled plasma facing components are made of carbon fiber com-

posite reinforced graphite elements, brazed on a metallic substrate and cooled by a pressurized water loop. It allows the extraction of heat in the steady-state conditions.

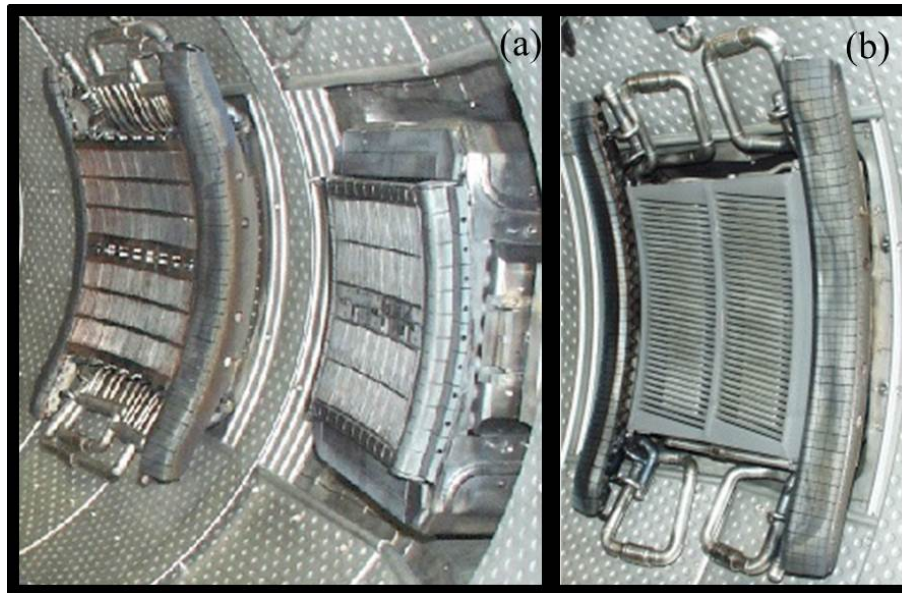


Figure 5: (a), The two LH antennas situated in the torus of the Tore Supra tokamak. To the left is the so-called Passive-Active Multijunction (PAM) while to the right is the LH coupler. (b), An Ion Cyclotron Resonance Frequency (ICRF) antenna on the Tore Supra tokamak.

The lower hybrid waves launched at 3.7 GHz (8 cm wavelength), with power generators of 8 MW are used to drive plasma current non-inductively. It has 16 klystrons, tube amplifiers, with a unit capacity of 500 kW, with a yield of 45% and 50 dB of gain. There are two antennas that are positioned horizontally in the torus as shown in Fig. 5(a). The antennas 1 and 2 allow the injection of 2 and 4 MW per unit area. More details on the LHCD are presented in section (LHCD). Discharges lasting 120 s were produced with a 0.8 MA current, with a central electron density of  $2 \times 10^{19} \text{ m}^{-3}$  using 2.5 MW of LH power [2, 5].

The ion cyclotron resonance heating (ICRH) is used for plasma heating. The heating system consists of a set of six generators in the 30-80 MHz range, transmission lines and three antennas. The generators convert electric power into electromagnetic waves that ranges between 30 and 80 MHz. Each generator has a cascade of 3 A tetrodes (an electronic device having four active electrodes) connected in series to achieve an out-

put power of 2 MW. The front of the antenna (Faraday shield) is coated with boron carbide ( $B_4C$ , low  $Z$  material) to protect the particle bombardment from the plasma and to avoid contaminating the plasma with metallic impurities. The antenna is protected by the right and left elements that allow actively cooled system to intercept the convected heat flux along the magnetic field lines that rely on these protections. All elements on the front of the antenna are cooled by the water system pressure (35 bar) at  $220^\circ\text{C}$  (max). Three antennas of this type, shown in Fig. 5(b) are installed on Tore Supra. Each can inject up to 4 MW between 40 and 80 MHz.

A new project called WEST was launched to modify the Tore Supra tokamak. This project will change Tore Supra from a limiter tokamak to a divertor configuration tokamak Fig. 6. The aim is to adapt Tore Supra in a way to test ITER divertor where an ITER-like full tungsten divertor will be installed in Tore Supra [5]. Thus, this step will contribute to reduce risk and to save time and money for ITER.

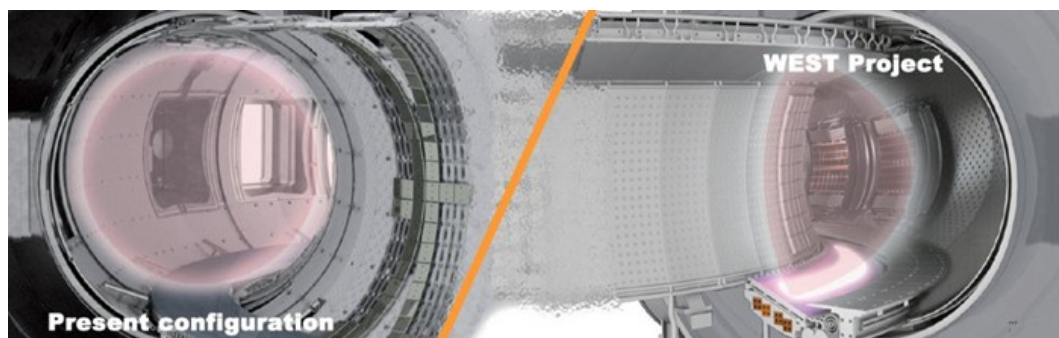


Figure 6: A expected configuration change of the Tore Supra Tokamak from a limiter-like (to the left) to a divertor-like (to the right) tokamak.

## C. Transport and turbulence

### 1. Classical transport

Collisions in plasmas cause stochastic forces that lead the particles to undergo random walks. These collisions can cause resistance to the flow of the current. The effects of collisions can be understood from the magnetohydrodynamics (MHD) treatment. The

MHD equations for zero resistivity are:

$$\frac{\partial \rho}{\partial t} + \nabla_{\perp} \cdot (\rho \mathbf{u}_{\perp}) = 0 \quad (3)$$

is the mass conservation equation.

$$\rho \frac{d\mathbf{u}}{dt} = \mathbf{J} \times \mathbf{B} \quad (4)$$

For collisions effects, we consider ohm's law, where the resistivity  $\eta$  appears as,

$$\mathbf{E} + \mathbf{u} \times \mathbf{B} = \eta \mathbf{J}, \quad (5)$$

where  $\rho$  is the mass density [6].

Thus, the perpendicular component of the velocity is

$$\mathbf{u}_{\perp} = \frac{\mathbf{E} \times \mathbf{B}}{B^2} - \frac{\eta_{\perp}}{B^2} \nabla p. \quad (6)$$

The first part of this velocity is the  $\mathbf{E} \times \mathbf{B}$  drift, while the second part is in the  $\nabla p$  direction which is perpendicular to the confining magnetic field. Thus collisions cause a cross-field transport of plasma particles down the pressure gradient, *i.e.*, collisions cause a reduction in the level of confinement. The flux associated with the velocity is

$$\Gamma_{\perp} = n\mathbf{u}_{\perp} = -\frac{n\eta_{\perp}}{B^2} \nabla p = -\frac{n\eta_{\perp} T}{B^2} \nabla n. \quad (7)$$

Fick's law has, in general, a diffusive coefficient  $D \sim (\Delta x)^2 / \Delta t$ . So, if we look to equation (7), we can recognize that it looks exactly like Fick's law with a diffusion coefficient

$$D_{\perp} = \frac{n\eta_{\perp}T}{B^2}, \quad (8)$$

where  $\Delta x$  is the mean spatial size and  $\Delta t$  is the mean step time. In this case, the step size is the Larmor radius  $\rho_L$  and the step time is the electron collision time. Hence, particle collisions are causing particle diffusion and it is the so-called classical diffusion or the classical transport.

## 2. *Neo-classical transport*

Geometric effects can cause an increase in the level of classical transport and this is referred to as neoclassical transport. In order to understand this type of transport, let us consider the magnetic mirror effect that leads to neoclassical banana diffusion. Consider a particle of charge  $q$  and mass  $m$  in a uniform magnetic field  $B$  and in the absence of an electric field. Thus the motion of the particle consists of a uniform velocity parallel to  $B$  and gyration perpendicular to  $B$  with cyclotron (or gyro) frequency

$$\omega_c = \frac{qB}{m}$$

and a Larmor radius

$$\rho = \frac{mv_{\perp}}{qB}$$

where  $v_{\perp}$  is the component of the velocity perpendicular to the magnetic field  $B$ . Thus the particle is in a helical motion. This kind of motion can be described as a rapid gyration around a guiding center that moves at constant velocity parallel to  $B$ . Consequently, this circulating charge constitutes a current loop of a magnetic moment  $\mu$  defined as

$$\mu = \frac{mv_{\perp}^2}{2B}. \quad (9)$$

It can be shown that the magnetic moment  $\mu$  is constant for  $B$  varying slowly in space or time, in other words  $\mu$  is adiabatically invariant.

Therefore, if the particle moves into a region of higher  $B$ ,  $v_{\perp}$  must increase in order to keep  $\mu$  constant. The total energy of the particle is constant and can be written as

$$E = \frac{mv_{\parallel}^2}{2} + \frac{mv_{\perp}^2}{2}, \quad (10)$$

where  $v_{\parallel}$  is the component of the velocity parallel to the magnetic field. Consequently, any increase in  $v_{\perp}$  must be accompanied by a decrease in  $v_{\parallel}$ . If  $B$  is large enough, there will come a point at which  $v_{\parallel}$  will tend to zero and the particle is reflected. In tokamaks, the magnetic field strength falls off with the major radius as  $1/R$  so that it is higher on the inboard side (near the axis of symmetry) than the outboard side. Thus particles moving in helical orbits experience an increase in magnetic field strength as they move from the outboard side to the inboard side. Particles with insufficient energy will be reflected and trapped in banana-shape orbits. Particles with sufficient energy to complete a full circuit around the tokamak are called passing particles. For the fraction of particles that are trapped in non-circulating banana orbits, the diffusion coefficient will have a banana orbit. Consequently, diffusion is increased to neoclassical levels. Other neoclassical effects lead to plateau and Pfirsch-Schluter diffusion [2].

#### **D. Plasma Instabilities**

In magnetic confinement, the gradients in the pressure are balanced by the strong magnetic field. The balanced equation is defined as:

$$\nabla p = \mathbf{J} \times \mathbf{B}, \quad (11)$$

where  $\mathbf{J}$  is the plasma current density. These pressure gradients can provide a free source of energy. As a result, it drives instabilities and, eventually, causes turbulence. Turbulent motion can modify the original gradients due to non-linear interactions. Instabilities on a macro-scale, such as MHD instabilities, can cause a disruption to the plasma and the plasma confinement may be completely lost. Smaller scale micro-instabilities, as scales of the ion Larmor radius, tend to degrade confinement by driving micro-scale turbulence. An important instability relevant to turbulent transport in the edge region of magnetically confined plasmas is the drift wave instability.

Drift wave instabilities act on the micro-scale and are thought to be responsible for the majority of anomalous transport in tokamaks. They have low frequencies compared to the ion cyclotron frequency ( $\omega_{ci}$ ) waves which are driven by gradients in density or temperature. They are generally electrostatic in nature,  $\mathbf{E} = -\nabla\phi$ , and involve two fluid physics. In the two fluid physics, ions and electrons are treated as two separate species. Each species has its own fluid equations that describe its motion. Thus we have two fluid equations, one for the electrons and another for the ions [7].

Let us take the electrostatic drift waves with an electric field  $\mathbf{E}$ . We shall proceed in the description found in Ref. [8]. We will try to derive the dispersion relation of the drift wave assuming an electrostatic approximation. This approximation assumes that the components of the perturbed electric field  $\mathbf{E}_1$  are related to each other by

$$\nabla \times \mathbf{E} = 0$$

. Thus the electric field can be written as the gradient of a scalar potential  $\phi$ ,

$$\mathbf{E} = -\nabla\phi. \tag{12}$$

The generalized Ohm's law for the first order perturbation is



$$\mathbf{E}_1 + \mathbf{u}_1 \times \mathbf{B}_0 = \eta \mathbf{j}_1 + \frac{1}{ne} (\mathbf{j} \times \mathbf{B} - \nabla p_e)_1. \quad (13)$$

where  $B_0$  is the unperturbed magnetic field and it is in the  $z$ -direction.  $1$  denotes the perturbed quantities.

This equation has two components, a perpendicular component and a parallel component to the magnetic field  $B$ . The perpendicular component approximates to

$$\mathbf{u}_\perp = \frac{\mathbf{E} \times \mathbf{B}}{B^2}, \quad (14)$$

and the parallel component is

$$E_\parallel = \eta j_\parallel - \frac{1}{ne} \nabla_\parallel p_e. \quad (15)$$

Recall that  $B_0$  is in the  $z$ -direction. Bearing in mind that we are dealing with wave components, all oscillating quantities can be represented in ‘exponential notation’. For instance, the density perturbations could be

$$n_1 = \bar{n}_1 \exp[i(\mathbf{k} \cdot \mathbf{x} - \omega t + \delta_n)]$$

, where  $\bar{n}_1$  is the real part,  $\mathbf{k}$  is the wave-vector and  $\delta_n$  is the phase-shift. Moreover, the operator  $\nabla$  becomes  $\hat{\mathbf{x}} \partial / \partial x$ . If we take all of our first-order quantities to vary as  $\exp[i(k \cdot x - \omega t)]$ , then  $\partial / \partial x$  becomes  $ik$  and  $\partial / \partial t$  becomes  $-i\omega$ . We neglect the magnetic field perturbations and the linearized equation (15) is written as

$$E_z = \eta j_z - \frac{ik_z p_{e1}}{ne}. \quad (16)$$

Using the electrostatic approximation in equation (14), equation (16) becomes

$$k_z B_{z0} u_x = k_y \left( \eta j_z - \frac{ik_z p_{e1}}{ne} \right) = k_y \left( \eta j_z - \frac{ik_z T_{e0}}{ne} n_{e1} \right). \quad (17)$$

The second form of equation (17) is written under the assumption that the electron temperature  $T_{e0}$  must remain uniform along the magnetic field.

Now using the continuity equation

$$-i\omega n_{e1} + u_x \frac{dn_{e0}}{dx} + ik_z n_{e0} u_z = 0$$

and the parallel component of equation of motion

$$-i\omega \rho_0 u_z = -ik_z T_{e0} n_{e1},$$

one can determine the density perturbations in terms of the parallel velocity. Finally, substituting this equation gives,

$$\left( 1 - \frac{k_y v_{de}}{\omega - k_z^2 C_s^2 / \omega} \right) u_x = \frac{k_y \eta}{k_z B_{z0}} j_z, \quad (18)$$

where we will use this equation to determine the dispersion relation of the electrostatic drift wave. It relates the mass velocity  $u_z$  to the current density  $j_z$ .

Using the  $x$  and  $y$  components of the perturbed equation of motion, we relate the perturbed density  $j_z$  to the mass velocity. Knowing that the perturbed current density is divergence-free,  $\nabla \cdot j = 0$ , the relation is

$$-i\omega \left( \frac{\partial}{\partial x} (\rho_0 u_y) - ik_y \rho_0 u_x \right) = -ik_z B_{z0} j_z, \quad (19)$$

where  $v_{de} = -\frac{T_{e0}}{n_{e0} e B_{z0}} \frac{dn_{e0}}{dx}$  is the electron diamagnetic drift velocity.

Finally, using the WKB approximation, we get

$$j_z = \frac{i\omega\rho_0}{k_y k_z B_{z0}} k_{\perp}^2 u_x, \quad (20)$$

where  $k_{\perp}^2 = k_x^2 + k_y^2$ . We use this result in equation (18) to end up by the dispersion relation

$$\omega - k_y v_{de} - \frac{k_z^2 C_s^2}{\omega} = \frac{i\eta k_{\perp}^2}{\mu_0} \frac{\omega^2 - k_z^2 C_s^2}{k_z^2 v_A^2}, \quad (21)$$

where  $v_A$  is the Alfvén speed. In the case where  $k_y v_{de} \ll k_z C_s$ , the frequency of the drift wave becomes simply

$$\omega \approx k_y v_{de}$$

and the growth rate of the instability is written as,

$$\gamma = \frac{\eta k_{\perp}^2 v_{de}^2}{\mu_0 k_z^2 v_A^2}. \quad (22)$$

Hence, the drift wave is produced by the perturbed electric field. Its perpendicular component gives rise to perpendicular plasma flows, while its parallel component is balanced self-consistently by the perturbed electron pressure gradient along the magnetic field.

## 1. Turbulence

“The study of turbulence in these plasmas is emphasized by the fact that turbulent fluctuations enhance the radial transport perpendicular to the magnetic field lines and thus reduce considerably the confinement times of particles and energy” [9].

Turbulence is a state of fluid motion or plasma characterized by unpredictability over a wide range of temporal and spatial scales. It is often referred to as the last great unsolved problem of classical physics since the governing equations are deterministic and have been studied since the 19<sup>th</sup> century.

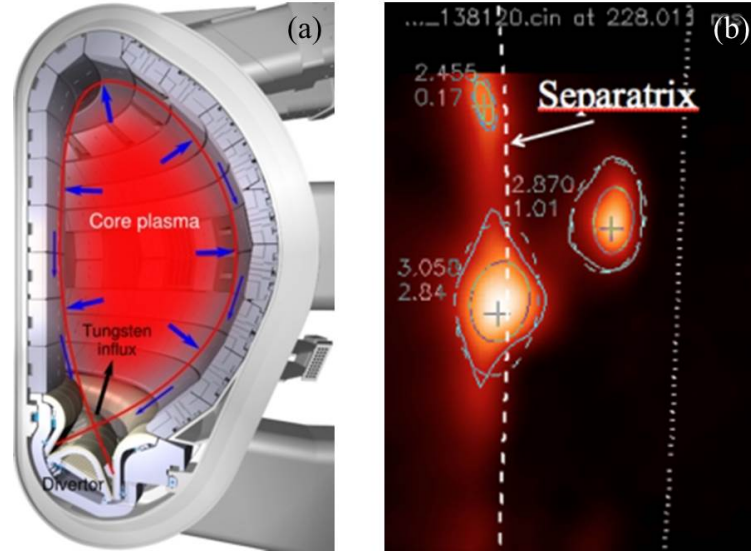


Figure 7: (a), shows a toroidal cut of a tokamak. Due to instabilities and turbulence, the plasma tends to escape the core radially, on average, as presented by the blue arrows and eventually loose the confinement. (b) shows a shot taken by a 2-D fast camera at the National Spherical Torus Experiment (NSTX) located at the Princeton Plasma Physics Laboratory. The shot shows how turbulent structures (blobs) radially, on average, escape the confinement zone, defined by the separatrix, which is the last closed magnetic field line

Turbulence in plasmas is a major problem. It causes the plasma to escape the confinement area. Thus, reaching the walls of the container, *i.e.*, the vacuum vessel in toroidal devices. If this happens, the walls will interact with the fuel causing impurities and leading to the failure in achieving fusion temperatures.

In fluid dynamics, a simple balance in the momentum balance equation of the non-linear and dissipative terms can yield the so-called *Reynolds* number. The Reynolds number is defined as:

$$Re = \frac{vL}{\nu}, \quad (23)$$

where  $v$  is the typical fluid velocity,  $L$  is the typical length scale and  $\nu$  is the viscosity in the system. In hydrodynamics, the transition from a laminar flow to a turbulent flow occurs for large values of Reynolds number. On the other hand, for magnetized plasmas, similar parameters are often used. Consequently, one can define the Reynolds number  $Re$

and its counterpart  $R_m$ , the magnetized Reynolds number [3]. Nevertheless, it is important to realize that these constructs are not identical due to non-diffusive dissipation processes such as Landau damping. These dissipative processes act on scales much smaller than the actual collisional dissipation.

Superposition of waves can also cause turbulence. Waves are driven by an underlying linear instability and the linear mode structure of the waves reflects the nature of the instability. When the linear instability has driven waves to sufficiently large amplitudes, waves may interact with each other through nonlinear interactions in the system. This wave-wave interaction acts in distributing the energy in a wave vector space. In the case of weak turbulence, the nonlinear coupling between waves is so weak and the energy may be distributed in a relatively narrow range of wave vectors. This effect leads to the broadening of the linear mode structure. In the case of strong turbulence, waves interact strongly and the energy can be distributed to a broadband range of wave vectors, and the linear mode structure may be lost [7].

### **E. Langmuir probe**

Due to turbulence and different types of instabilities occurring, radial transport allows particle leakage leading to the loss of confinement. Different processes happening are to be detected in order to understand the different phenomena leading to this confinement loss. The experimentally determined energy and particle transport coefficients in a tokamak greatly exceed those calculated from collision theory. It is generally accepted that the plasma turbulence is responsible for this. A considerable experimental effort has been made trying to understand the anomalous transport operating to distinguish between different theoretical models.

Electrostatic fluctuations affect both particle transport and heat conduction. The average particle flux may be written as:

$$\Gamma_{\perp} = \langle \tilde{u}_{\perp} \tilde{n} \rangle, \quad (24)$$

where  $\tilde{u}_{\perp}$  and  $\tilde{n}$  are the fluctuating parts of the velocity and the particle density respectively. The heat flux is also affected and the turbulence gives rise to the term

$$q_j = \frac{3}{2} n_j \langle \tilde{u}_{\perp} \tilde{T}_j \rangle, \quad (25)$$

where  $\tilde{T}_j$  is the temperature fluctuation.

In order to properly evaluate the importance of fluctuations, measurements of  $\tilde{n}$ ,  $\tilde{T}_j$  and other parameters is required which is clearly a complicated and tough task. The most comprehensive measurements have been made at the plasma edge where the fluctuations are at their highest. Much of this work has been done using magnetic and Langmuir probes in the SOL. As for the plasma center, this technique will not work. The probes may cause perturbations to the plasma too greatly and would be melted by the high heat fluxes. At the center more limited data is available from scattering experiments and heavy ion beam probes.

As for our experiments, data are measured using fixed Langmuir probes situated on the  $C_4$  lower hybrid coupler at the mid-plane in-between the two ICRH antennas  $Q_5$  and  $Q_1$  on the Tore Supra tokamak. The setup is shown in Fig. 8

Quantitative characterization of plasma edge turbulence can be achieved with Langmuir probes. A Langmuir probe (Fig. 9) is a device used to determine different plasma parameters as electron temperature, electron density, and electric potential of a plasma. It works by inserting one or more electrodes into the plasma, with a constant or time-varying electric potential between the various electrodes or between them and the surrounding vessel. The measured currents and potentials in this system allow the determination of the physical properties of the plasma.

Langmuir probes are restricted to the edge of fusion plasmas due to the high

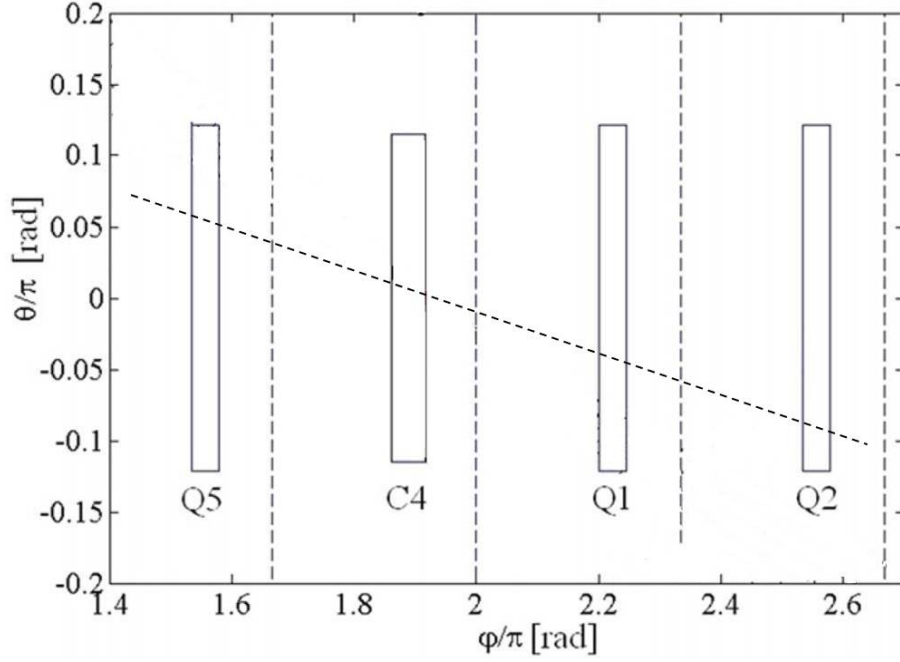


Figure 8: This figure shows the position of the  $C_4$  coupler on the Tore Supra tokamak in the  $\theta$ - $\phi$  plane . The oblique dashed (- -) line represents a closed field line.  $\theta$  and  $\phi$  are, respectively, the poloidal and toroidal angles. As shown in the figure,  $C_4$  is situated between the two ICRH antennas  $Q_5$  and  $Q_1$ . [10]

temperatures of the central regions. The current  $I$  to a probe biased at voltage  $V$  is given by:

$$I = J_i(1 - e^{(V-V_f)/k_B T_e})A, \quad (26)$$

where  $J_i$  is the ion current density,  $A$  is the surface area of the probe and  $V_f$  is the floating potential (the applied potential at which current drops to zero) [2].

If the probe is sufficiently negatively biased all electrons within a narrow sheath will be repelled and only an ion current is left. This so-called ion saturation current is independent of the voltage,

$$I_{sat} = en_e A \sqrt{T_e/m_i}. \quad (27)$$

It was found in the tokamak SOL that temperature fluctuations are much less

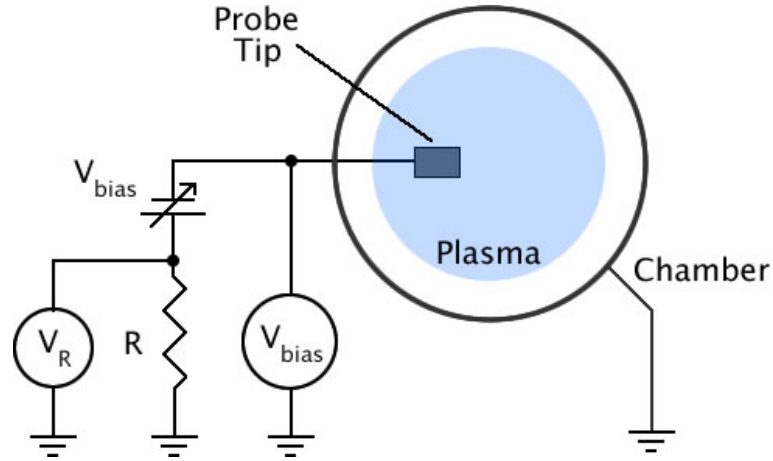


Figure 9: The electrical mechanism by which the probe measures the plasma properties.

than density fluctuations, *i.e.*,

$$\frac{\tilde{T}}{\bar{T}} \ll \frac{\tilde{n}}{\bar{n}}$$

but since we have

$$\frac{\tilde{I}}{\bar{I}} \approx \frac{1}{2} \frac{\tilde{T}}{\bar{T}} + \frac{\tilde{n}}{\bar{n}}$$

finally we end up by,

$$\frac{\tilde{I}}{\bar{I}} \approx \frac{\tilde{n}}{\bar{n}}$$

This relation shows how the data the ion saturation current reflects are mainly those for density fluctuations.

Data taken from the Langmuir probes aiming to measure the fluctuations generally has much higher time resolution than data from other more complicated plasma diagnostics. This makes it ideal for statistical analysis.

The Langmuir probes on the Tore Supra Tokamak are flush mounted with a diameter of 5 mm and their radial position is 3.164 m from the torus axis.



## CHAPTER II

### INTRODUCTION TO STATISTICAL ANALYSIS

#### A. Introduction

Statistical analysis is the study of the collection, organization, analysis, interpretation and presentation of a certain set of measured or recorded data. It deals with all aspects of data including the planning of data collection in terms of the design of surveys, scientific data processing and experiments. It is the science of exploring, collecting and presenting large amount of data to discover underlying patterns and trends. This kind of studies is applied every day in different branches of research in order to have a more scientific view on different decisions that need to be made. Hence, whenever we perform an experiment, we will need certain tools in order to interpret the collected data; these tools are the statistical tools. The precision of the equipment that we use defines the accuracy of our measurements. In many cases and processes that are under investigation, stochastic nature emerges, *i.e.*, not predictable with arbitrary precision. So, we are forced to present the results in the form of estimates with error intervals. Estimates accompanied by an uncertainty interval allow testing scientific hypotheses. This helps in averaging the results of different experiments to improve continuously the accuracy. By this procedure, a constant progress in experimental sciences and their applications was achieved.

Plasma transport in the edge and in the tokamak SOL is an active field of research. Statistical analysis is a main tool in understanding the causes and effects of different phenomena causing this transport for the tokamak design and operation. The ability to model and control plasma transport across the magnetic field in the SOL is critical for the optimal design of divertors and for predicting the lifespan of plasma facing components [11]. For instance, edge and SOL physics impact the plasma transport through

the level of impurities generated by plasma-wall interaction as shown in Ref. [12]. From different experiments aiming in transport study, the data taken in the SOL shows that it is bursty and intermittent. Besides, the fluctuations probability distributions in plasma parameters are non-Gaussian [13, 14, 15].

All these features lead to inaccurate results, and hence the statistical tools will serve in a further understanding of the measurements. In our study, data taken on the Tore Supra tokamak are aimed in studying the SOL properties under the effect of the injected LH waves. Several discharges are done to acquire a wide range of data. These discharges will allow the statistical analysis of the different phenomena with highest precision possible. The discharges are sampled with two different ranges of acquisition frequencies. One is called DFLUC, where the ion saturation current is acquired at 1 MHz, with 13600 points per trigger per channel. The other is called DCEDRE which is acquired at 200 MHz, with 100,000 points per trigger per channel. A high-pass filter is installed on the data acquisition damping fluctuations below 100 kHz. Consequently, DFLUC allows the study of electrostatic turbulent fluctuations occurring at frequencies below 100 kHz. DCEDRE, on the other hand, allows the study of fluctuations between 0.1 – 100 MHz.

Three different types of statistical analysis are used to analyze the ion saturation current  $I_{sat}$  data taken from the edge region of the Tore Supra tokamak. We start by the probability density function (PDF) and its first four order moments. Next, we study the power spectrum  $S(f)$ , also called the power spectral density, and its integration. Finally we study the cross-correlation coefficients,  $Cx_{12}$ , and its properties.

## **B. The Probability Density Function (PDF)**

The probability density function (PDF) of any random variable  $X$ ,  $P(x)$ , is a function that describes the relative likelihood for  $X$  to take on a given value. The probability that  $X$  lies within  $\delta x$  of  $x$  is  $P(x)\delta x$ .

The probability that  $X$  takes on a value in the interval  $[a, b]$  is the area above this interval and under the graph of the density function defined as:

$$P(a \leq b) = \int_a^b P(x)dx \quad (28)$$

as shown in Fig. 10

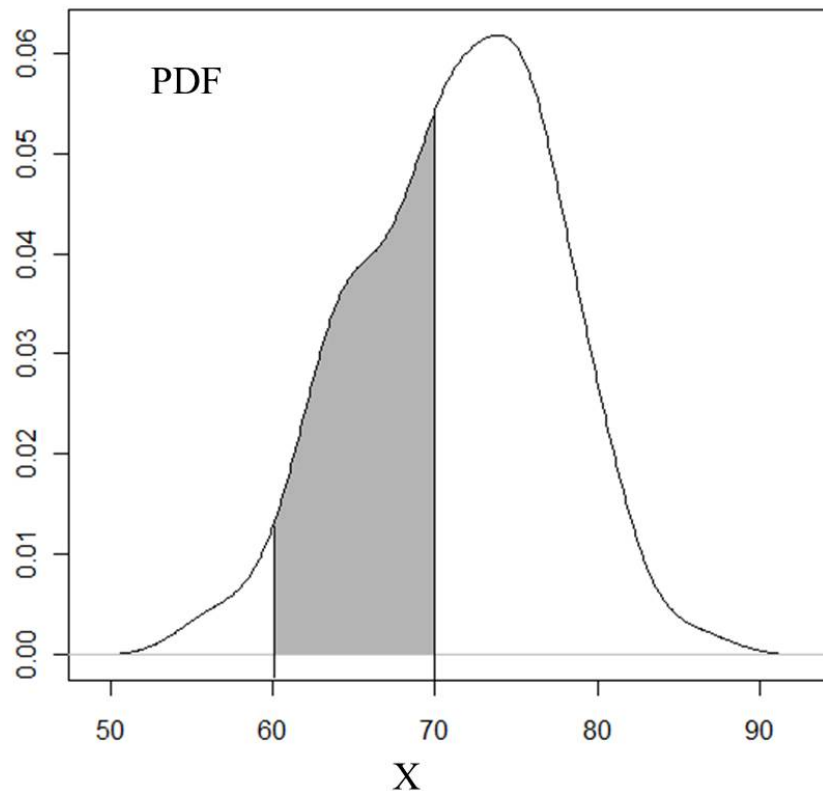


Figure 10: The probability density function of the random variable  $X$  between 60 and 70. It shows that the PDF is the area under the distribution.

In general, the probability density function has several order moments. These moments specify the higher order properties of the PDF. The  $n$ th order moment of  $P(x)$  is defined as:

$$m_n = \langle x^n \rangle = \int_{-\infty}^{+\infty} x^n P(x)dx. \quad (29)$$

## 1. Moments of the PDF

### a. The Mean value

The average value, or the mean value, is the first order moment of the PDF. It is the expected outcome, which is the statistical average, from a certain distribution and it is defined as the  $n = 1$  moment of the PDF as:

$$\mu = \langle x \rangle = \int_{-\infty}^{+\infty} xP(x)dx. \quad (30)$$

For the ion saturation current  $I_{sat}$ , the average value is denoted as  $\langle I_{sat} \rangle$ . The notation  $\langle \rangle$  is the temporal average and is defined for a certain variable  $x$  as

$$\langle x \rangle = \frac{1}{T} \int_0^T x(t)dt$$

which is not exactly as the statistical average mentioned above. Consequently, for a steady state system, the two averages become similar with the same outcome

$$\langle \langle \rangle \rangle_t = \langle \langle \rangle \rangle_{stat}.$$

The higher order moments of the PDF about the mean are thus defined as

$$\mu_n = \langle (x - \langle x \rangle)^n \rangle = \int_{-\infty}^{+\infty} \langle (x - \langle x \rangle)^n \rangle P(x)dx. \quad (31)$$

### b. The Variance and the standard deviation

The second order moment of the PDF is called the variance,  $Var(x)$ . It measures how  $P(x)$  spreads around the mean. It is defined as:

$$Var(x) = \langle (x - \langle x \rangle)^2 \rangle = \int_{-\infty}^{+\infty} \langle (x - \langle x \rangle)^2 \rangle P(x) dx. \quad (32)$$

From the  $Var(x)$ , one can calculate the standard deviation  $\sigma_x$ , which can also be defined as the second moment of the PDF. The standard deviation is defined as the square-root of the variance:

$$\sigma_x = \sqrt{Var(x)}.$$

For the ion saturation current  $I_{sat}$ , the standard deviation which measures the level of fluctuations is denoted as  $\delta I_{sat}$ . It provides critical understanding on the behavior of the turbulent structures. Moreover, we will be presenting the normalized level of fluctuations,  $\delta I_{sat}/I_{sat}$  which reflects modifications on the level of turbulence.

### c. Skewness

The third order moment,  $n=3$ , allows us to determine the skewness factor,  $S$ , of the PDF. The third order moment is defined in statistics as:

$$\mu_3 = \langle (x - \langle x \rangle)^3 \rangle = \int_{-\infty}^{+\infty} \langle (x - \langle x \rangle)^3 \rangle P(x) dx. \quad (33)$$

The skewness factor is the normalized third order moment of the PDF and thus defined for the ion saturation current  $I_{sat}$  as

$$S = \langle I_{sat}^3 \rangle / \langle I_{sat}^2 \rangle^{3/2}. \quad (34)$$

The skewness measures the asymmetry of the distribution around the average value. For a Gaussian distribution, the skewness factor has a value 0 reflecting a symmetric distribution of the data around the mean as illustrated Fig. 11(a). If the peak is toward

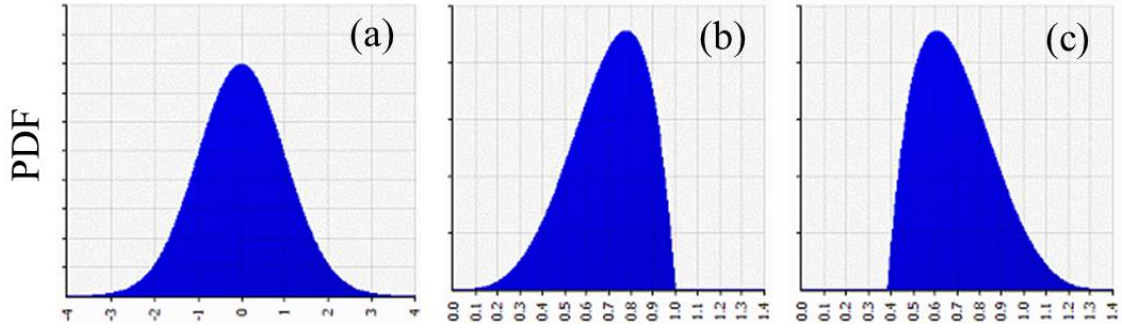


Figure 11: (a) shows the PDF of a Gaussian distribution with  $S=0$ . Notice that it is symmetric around the mean. (b) and (c) show the PDF of a negatively ( $S=-0.54$ ) and positively ( $S=+0.54$ ) skewed distributions respectively.

the right and the left tail is longer, we say that the distribution is skewed left or negatively skewed [Fig. 11(b)]. If the bulk of the data is at the left and the right tail is longer, we say that the distribution is skewed right or positively skewed [Fig. 11(c)].

#### d. Flatness (Kurtosis)

The Flatness, or also known as Kurtosis, is the normalized fourth order,  $n=4$ , moment of the PDF. The fourth order moment in statistics is defined as

$$\mu_4 = \langle (x - \langle x \rangle)^4 \rangle = \int_{-\infty}^{+\infty} \langle (x - \langle x \rangle)^4 \rangle P(x) dx. \quad (35)$$

Thus, the flatness for the ion saturation current  $I_{sat}$  is

$$F = \langle I_{sat}^4 \rangle / \langle I_{sat}^2 \rangle^2. \quad (36)$$

The flatness characterizes height and sharpness of the peak and the weight of the tail of a certain distribution. Increasing kurtosis is associated with the “movement of probability mass from the shoulders of a distribution into its center and tails” [16]. Furthermore, The flatness for a Gaussian distribution is 3. So, the more the shift of data

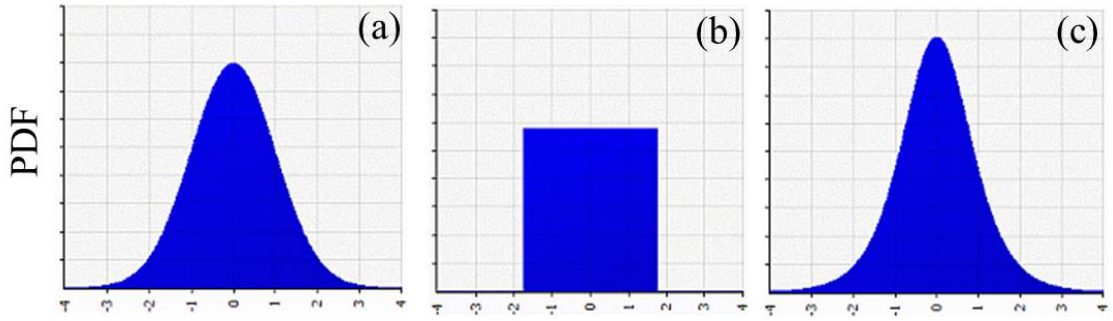


Figure 12: (a) shows the PDF of a Gaussian distribution with  $F=3$ . (b) is the PDF of a distribution with  $F=1.8$ . (c) is the PDF of a distribution with  $F=4.2$ .

to the tail the more the flatness will be.

In our analysis, the skewness and the flatness gives important details on how turbulent structures are modified in the presence of the LH power. A denser tail means more shift of the turbulent structures from the bulk which reflects more high-intensity events. It was found in the ohmic case that SOL turbulence contains intermittent bursts which are caused by large-scale structures that exit the plasma with high radial velocities that reach one-tenth of the sound speed. These bursts will result in positively skewed PDFs with skewness and flatness values greater than 0 and 3 respectively [17, 18].

### C. Power spectrum

The power spectrum, known also as the power spectral density, is a powerful tool that helps in studying and analyzing any signal. The power spectrum of any signal measures the frequency content of a process (random or coherent) and helps identify periodicities and energies associated to each frequency. The power spectrum of a signal identifies how much of the signal is present at each frequency. It is simply related to the amplitude of the Fourier transforms. Every physical phenomenon, whether it is an electromagnetic, thermal, mechanical, hydraulic or any other system, has a spectrum associated with it. The power spectrum is calculated from the Fourier-transform of the signal. It thus transforms any signal from its space-time domain into the wavenumber-Frequency

domain. Hence, when calculating the spectrum of any signal, we will be analyzing its properties in the frequency domain. The Fourier transform  $y(\omega)$  of a signal  $y(t)$  is

$$y(\omega) = \int_{-\infty}^{+\infty} y(t)e^{-j\omega t} dt. \quad (37)$$

The power spectrum is then

$$P(\omega) = \langle |\tilde{y}(\omega)|^2 \rangle, \quad (38)$$

where  $\omega$  defines the angular frequency.

For instance, let us take sine wave signal  $y(t) = \sin(\omega_0 t)$  with  $\omega_0 = 120\pi$  (shown in Fig. 13(a)). Taking the number of points of the signal to be 1024 points, and using MATLAB code we can calculate the power spectrum of this signal.

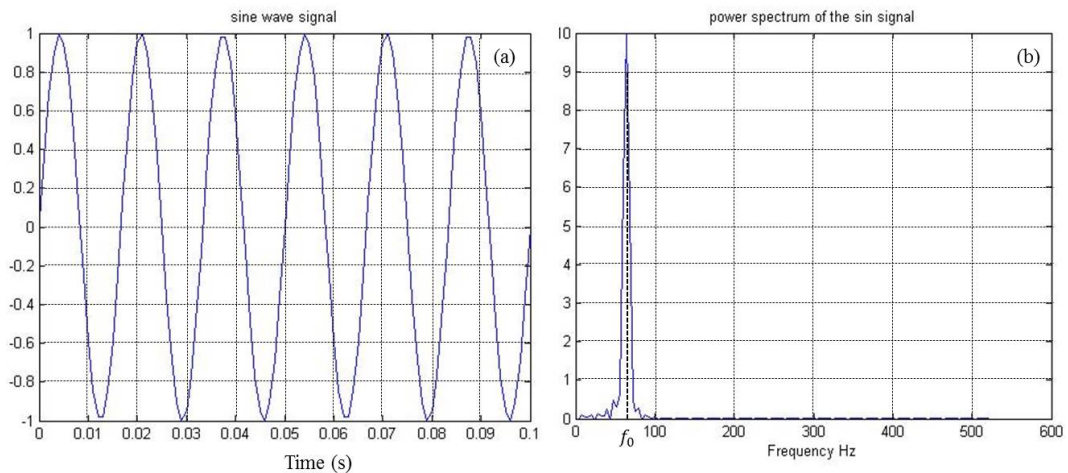


Figure 13: (a) shows the sine wave plot in time. (b) is the power spectrum of the sine wave. Notice the delta function peaked at  $f_0 = 60$  Hz.

In Fig. 13(b), the power spectrum is plotted in the frequency domain. Now we can see the relation between the time domain and the frequency domain. The frequency domain illustrates the distribution of the signal over the frequency.  $y(t)$  oscillating with a frequency  $f_0 = 60$  Hz, is reflected in the frequency domain by a delta function peaked at  $f_0 = 60$  Hz. If we try to solve the problem analytically, we calculate the power spectrum



for the sine wave signal:

$$\tilde{y}(\omega) = \int_{-\infty}^{+\infty} y(t)e^{-j\omega t} dt = \int_{-\infty}^{+\infty} \sin(\omega_0 t)e^{-j\omega t} dt. \quad (39)$$

Using the relation:

$$\sin(\omega_0 t) = \frac{e^{j\omega_0 t} - e^{-j\omega_0 t}}{2j}, \quad (40)$$

we hence get:

$$\tilde{y}(\omega) = \int_{-\infty}^{+\infty} e^{j(\omega \pm \omega_0)t} dt. \quad (41)$$

This is the delta function  $\delta(\omega - \omega_0)$  which states that:

$$\begin{cases} 1 & \text{for } \omega = \omega_0 \\ 0 & \text{otherwise.} \end{cases} \quad (42)$$

Hence, this verifies the plot of the power spectrum in Fig. 13(b) to be a delta function peaked at  $f_0 = 60$  Hz. Recall that  $\omega_0 = 2\pi f_0$ .

The power spectrum is defined for the normalized ion saturation current  $I_{sat}/\delta I_{sat}$  such that  $\int dfS(I_{sat}/\delta I_{sat}) = 1$ . Hence, when calculating the power spectrum, we are interested in the distribution of the turbulent fluctuation frequencies as function of the LH power.

The power spectrum is quantified by calculating its area under the graph, *i.e.*, its integration  $\int dfS(f)$ . When using the power integration, a more representative analysis of the power spectrum will be presented since the maximum number of discharges will

be plotted as a function of power. Hence, global averaging will result and this will allow us to understand the underlying phenomena that the power spectrum encounters.

#### D. The Cross-correlation, $Cx_{12}$

The cross-correlation in signal processing is defined as the measure of similarity of two waveforms as a function of a time-lag applied to one of them. It is a standard method of estimating the degree to which two series are correlated.

In general, the cross-correlation for two continuous functions  $f$  and  $g$  measured as a function of time is defined as

$$Cx(\tau) = (f \star g)(\tau) = \int_{-\infty}^{+\infty} f^*(t)g(t + \tau)dt = \int_{-\infty}^{+\infty} f^*(x)g(x + r)dr, \quad (43)$$

where the last part of the equation is the cross-correlation in space with a shift  $r$ .  $\tau$  is the time lag between the two signals and  $f^*$  is the complex conjugate of  $f$ .

To understand the concept of the cross-correlation, let us take two real valued functions  $f$  and  $g$  that differ only by an unknown shift along the x-axis. One can use the cross-correlation to find how much  $g$  must be shifted along the x-axis to make it identical to  $f$ .

The formula essentially slides the  $g$  function along the x-axis as shown in Fig. 14, calculating the integral of their product at each position. When the functions match, the value of  $(f \star g)$  is maximized. This is because when peaks (positive areas) are aligned, they make a large contribution to the integral. Similarly, when troughs (negative areas) align, they also make a positive contribution to the integral because the product of two negative numbers is positive.

The cross-correlation can be defined also from the covariance of two variables  $X$

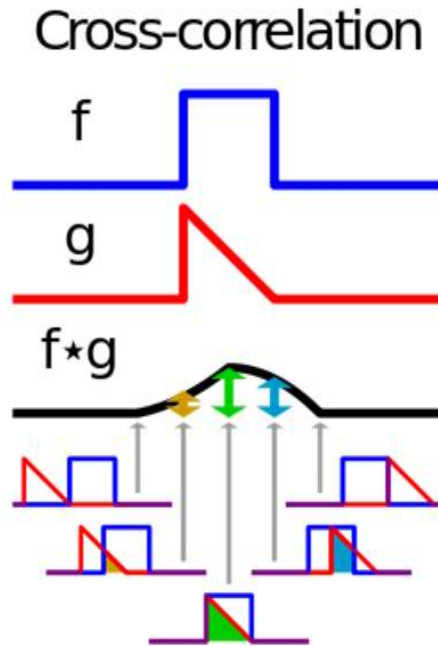


Figure 14: The cross-correlation between the two signals  $f$  and  $g$ . Notice how the two functions are related and that the maximum relation when they coincide.

and  $Y$ . The covariance is defined as:

$$cov(X, Y) = \langle (x - \langle x \rangle)(y - \langle y \rangle) \rangle = \langle xy \rangle - \langle x \rangle \langle y \rangle, \quad (44)$$

and the cross-correlation is

$$corr(X, Y) = \frac{\langle (x - \langle x \rangle)(y - \langle y \rangle) \rangle}{\sigma_x \sigma_y} = \frac{cov(X, Y)}{\sqrt{cov(X, X) cov(Y, Y)}}. \quad (45)$$

This is the normalized measure of the degree of dependence of  $X$  and  $Y$  on each other. When  $corr(X, Y)=0$ , then  $X$  and  $Y$  are independent. If  $corr(X, Y)=1$ , then  $X$  and  $Y$  are perfectly correlated and if  $corr(X, Y)=-1$ , then  $X$  and  $Y$  are perfectly anti-correlated.

As for the ion saturation current  $I_{sat}$  in our measurements, the cross-correlation is done between the two Langmuir probes. It is defined as:

$$Cx_{12} = \frac{\langle I_{sat1}(t)I_{sat2}(t + \tau) \rangle}{\langle I_{sat1}^2 \rangle^{1/2} \langle I_{sat2}^2 \rangle^{1/2}}, \quad (46)$$

where  $\tau$  is the time lag.

In our experiments, the cross-correlation is done between the data taken by the two probes which are situated in the torus of the Tore Supra tokamak. The probes are separated toroidally by 1 cm. The cross-correlation is a powerful tool in studying the modification of turbulence with LHCD, and it gives a critical understanding about variations in turbulent structures.

## CHAPTER III

### THE LOWER HYBRID CURRENT DRIVE (LHCD)

#### A. The need for a non-inductive current drive method

##### 1. The plasma current

Usually in tokamaks the central solenoid plays the role in creating the inductive plasma current and that is when a changing current flows through this solenoid, the plasma itself acts as a secondary winding and has a large current induced in it. In other words, the current in the solenoid ( $I_s$ ) creates a magnetic field which affects the plasmas, that are highly conductive material, and due to this magnetic field a current is driven through an opposite circulation of the electrons and the ions which creates a potential difference and thus driving a large plasma current ( $I_p$ ). Note that vectors are presented as bold characters. The current density equations [8] for the electrons and ions are respectively:

$$\mathbf{j}_e = -en_e\mathbf{v}_e \quad (47)$$

$$\mathbf{j}_i = en_i\mathbf{v}_i. \quad (48)$$

Hence the total current density of the plasma is:

$$\mathbf{J}_T = \mathbf{j}_i + \mathbf{j}_e = en_i\mathbf{v}_i - en_e\mathbf{v}_e. \quad (49)$$

We assume that the electrons and the ions have roughly the same density, in other words,  $n_e = n_i = n$ . The total current density becomes

$$\mathbf{J}_T = en(\mathbf{v}_i - \mathbf{v}_e). \quad (50)$$

It is well known that a magnetic field encircling a conducting wire generates an electric current through this wire. As the plasma is a conducting fluid, it can be treated as this wire. As the magnetic field created by the central solenoid,  $B_s$ , encircles the plasma, the plasma current  $I_P$  is generated.

The variable current in the solenoid  $I_s$  creates this variable magnetic field  $B_s$ . According to Faraday, the potential difference created in the solenoid, also called electromotive force (e.m.f.), is limited to a variable magnetic flux.

Since most of the magnetic field lines of the solenoid are intercepted by the plasma in the torus, the magnetic flux in the plasma is mostly the magnetic flux of the solenoid, *i.e.*,

$$\phi_{Plasma} \simeq \phi_{solenoid}$$

From Faraday's law, the e.m.f. created in the plasma is proportional to the variations of the magnetic flux which is in this case  $\phi_s$  the flux generated by the solenoid magnetic field. So, the e.m.f. in the plasma is

$$\mathcal{E}_P = -\frac{d\phi_s}{dt} = RI_P. \quad (51)$$

The second part of the equation is the Ohm's law where  $R$  is the resistance of the plasma. For a constant  $I_P$  and  $R$ , we can integrate equation (51) to get

$$\phi_s = RI_P t. \quad (52)$$

On the other hand, the magnetic flux in the plasma, which is equal to the solenoid magnetic flux, through a certain area  $A$  can be calculated as follows:

$$\phi_P = \phi_s = NB_s A \sin(\mathbf{B}_s, \mathbf{A}) = B_s A, \quad (53)$$

where  $A$  is the cross-section area of the solenoid.

From Ampere's Law, the magnetic field  $B_s$  created by the solenoid through a conductive volume due to the central solenoid current  $I_s$  is

$$B_s = \mu_0 n I_s. \quad (54)$$

Hence, by substituting this value of  $B_s$  in equation (53), the magnetic flux becomes:

$$\phi_s = BA = \mu_0 n I_s A. \quad (55)$$

Finally, we equate equations (52) and (55) to get the central solenoid current  $I_s$  in terms of the plasma current  $I_P$  as:

$$I_s = \frac{R I_P}{\mu_0 n I_s A} t. \quad (56)$$

For steady state operations and to have a constant plasma current  $I_P$ , the current in the solenoid  $I_s$  should be increasing linearly with time according to:

$$I_P \approx \frac{dI_s}{dt} = \text{constant}. \quad (57)$$

Due to limits in energy sources, and since the current that must be generated in plasma tokamaks is in the order of Mega Amperes (MA), the search for non-inductive plasma current generation is crucially important.

Electromagnetic wave heating has proved to be effective in heating and current

drive. RF heating, Ion Cyclotron Resonance Heating (ICRH), Electron Cyclotron Resonance Heating (ECRH), Lower Hybrid Heating (LH) and other methods have been tested.

As for the current drive, the most extensive evidence has been accumulated for the lower hybrid current drive effect. While LH waves are not very successful at plasma heating, they have proven excellent at driving plasma current.

## 2. Lower hybrid waves

A lower hybrid wave is a longitudinal wave of ions and electrons in magnetized plasma. The direction of propagation must be very nearly perpendicular to the stationary magnetic field, within about  $\sqrt{m_e/m_i}$  radians. Otherwise, the electrons can move along the field lines fast enough to shield the oscillations in potential, the case in which an electrostatic ion cyclotron wave results. The frequency of oscillation is:

$$\omega_{LH} = [(\omega_{ci}\omega_{ce})^{-1} + \omega_{pi}^{-2}]^{-1/2}, \quad (58)$$

where  $\omega_{ci}$  is the ion cyclotron frequency,  $\omega_{ce}$  is the electron cyclotron frequency and  $\omega_{pi}^{-2}$  is the ion plasma frequency. This is the lower hybrid frequency, so called because it is a “hybrid”, or mixture, of two frequencies. There are also an upper hybrid frequency and hence, an upper hybrid wave.

There are many other resonant frequencies in tokamak plasmas but experiments have found some to be inefficient or impractical while others simply cannot penetrate through the plasma edge region in order to generate currents.

The so-called “hybrid” is because it results from force interplay between ions and electrons, so that their frequencies lie between ion cyclotron and electron cyclotron ones. It is found that the lower hybrid wave can drive electric current. Thanks to the fact that it has an electric component parallel to magnetic field lines.



One would perhaps expect that the very rapidly alternating electric field of electromagnetic waves could not generate a constant electric current, but this common sense proves to be false. Plasma electrons, with thermal velocities slightly slower than the wave propagation velocity, can actually “surf” on the uprising electric potential and thus increase their velocity in the direction of the wave. Consequently, there are more electrons which are accelerated rather than decelerated so that in total a net generation of current is obtained when electrons in the tail of the distribution are accelerated by the wave preferentially in one direction. Though the effect looks minute on the electron velocity distribution, in terms of electric drag it is significant.

### 3. Dispersion Relation

In this part we calculate the dispersion relation of the lower hybrid wave. The electromagnetic wave needs to be absorbed by the plasma in order to generate current. So, by calculating the dispersion relation of this wave, we can find the conditions of absorption. To calculate the dispersion relation [19] we start by the cold plasma wave equation:

$$\mathbf{n} \times (\mathbf{n} \times \mathbf{E}) + K \cdot \mathbf{E} = 0, \quad (59)$$

where  $\mathbf{n} = (\frac{c}{\omega})\mathbf{k} = n_{\perp}\hat{\mathbf{e}}_{\perp} + n_{\parallel}\hat{\mathbf{e}}_{\parallel}$  is the index of refraction of the plasma and  $\mathbf{E}$  is the electric field of the wave. The tensor  $K$  has the form

$$K = \begin{pmatrix} S & -iD & 0 \\ iD & S & 0 \\ 0 & 0 & P \end{pmatrix}$$

where

$$D = \frac{\omega_{pi}^2 \omega_{ci}}{\omega(\omega^2 - \omega_{ci}^2)} - \frac{\omega_{pe}^2 \omega_{ce}}{\omega(\omega^2 - \omega_{ce}^2)}$$

$$S = 1 - \frac{\omega_{pi}^2}{\omega^2 - \omega_{ci}^2} - \frac{\omega_{pe}^2}{\omega^2 - \omega_{ce}^2}$$

$$P = 1 - \frac{\omega_{pi}^2}{\omega^2} - \frac{\omega_{pe}^2}{\omega^2}.$$

We Recall that  $\omega_{ci}$  and  $\omega_{ce}$  are respectively the ion and the electron cyclotron frequencies, while  $\omega_{pi}$  and  $\omega_{pe}$  are the ion and the electron plasma frequencies respectively.

When dealing with such equation, we have the parallel ( $\parallel$ ) part, *i.e.*, parallel to the path of the total magnetic field lines, and the perpendicular ( $\perp$ ) part, *i.e.*, perpendicular to the path of the total magnetic field lines. We set the coefficients of the wave equation to zero in order to find the dispersion relation. Consequently, we get the following equation

$$\beta n_{\perp}^4 - \gamma n_{\perp}^2 + \delta = 0 \quad (60)$$

where

$$\beta = S,$$

$$\gamma = RL + PS - (P + S)n_{\parallel}^2,$$

$$\delta = P(R - n_{\parallel}^2)(L - n_{\parallel}^2),$$

$$R = S + D,$$

$$L = S - D.$$

From equation (60), we can calculate  $n_{\perp}^2$  for the two branches:

1- The fast wave which is specified by the relation

$$n_{\perp}^2 = (\gamma - \sqrt{\gamma^2 - 4\beta\delta})/2\beta; \quad (61)$$

2- The slow wave which is specified by the relation:

$$n_{\perp}^2 = (\gamma + \sqrt{\gamma^2 - 4\beta\delta})/2\beta. \quad (62)$$

We are interested in the slow branch since at  $\beta=0$  equation (62) has a resonance. Then by setting  $\beta$  to 0, we get the following equation:

$$\omega^4 - (\omega_{ce}^2 + \omega_{pe}^2)\omega^2 + (\omega_{ci}^2 + \omega_{pi}^2)\omega_{ce}^2 = 0. \quad (63)$$

Note that we can neglect the terms of  $m_e/m_i$  order, and hence leading to the following resonance frequencies:

$$\omega_{UH}^2 = \omega_{ce}^2 + \omega_{pe}^2 \quad (64)$$

$$\omega_{LH}^2 = \omega_{ce}^2 \frac{\omega_{ci}^2 + \omega_{pi}^2}{\omega_{ce}^2 + \omega_{pe}^2}, \quad (65)$$

where  $\omega_{UH}$  and  $\omega_{LH}$  corresponds to the so-called upper hybrid frequencies and the lower hybrid frequencies respectively.

Moreover, considering that the ion cyclotron frequency is much smaller when compared to the ion plasma frequency due to mass of the ions  $\omega_{ci} \ll \omega_{pi}$ , we neglect the  $\omega_{ci}^2$  to get the final dispersion relation for the Lower hybrid waves

$$\omega_{LH}^2 \simeq \frac{\omega_{pi}^2}{1 + \omega_{pe}^2/\omega_{ce}^2}. \quad (66)$$

It is called ‘‘hybrid’’ because it is a combination of the cyclotron and plasma frequencies of the ions and electrons. Consequently, at  $\omega = \omega_{LH}$ , we have  $n_{\perp} = 0$  reflecting that the plasma absorb the wave power emitted by the antennas. The absorbed power in

general may be used to either plasma heating or current drive. As for the LH waves, it is well known that they are inefficient for heating but quite efficient for current drive due to the Landau damping process according to which electrons at the tail of the distribution gain energies from the waves. Hence, electrons are accelerated in one toroidal direction and the net flow of these preferentially accelerated electrons generates plasma current in the toroidal direction.

#### ***4. The momenta transfer and parallel velocity***

By using a phased waveguide array antenna, power may be coupled to lower hybrid waves with high phase velocity parallel to the magnetic field. These waves are resonant with high energy electrons having a parallel velocity which matches the phase velocity of the wave and absorption takes place through Landau damping. The phased array antenna ensures that most of the power is coupled to waves propagating in a particular toroidal direction so that the wave-particle interaction occurs preferentially with electrons traveling in that direction. In the simplest picture, the lower hybrid waves directly impart momentum to these electrons which, in steady state, leads to the generation of a current determined by the balance between the momentum input and the loss by collisions to the ions. However, a more important effect is that the accelerated electrons become less collisional and lose momentum at a slower rate. Since electrons moving in a particular toroidal direction are preferentially heated, this gives rise to a so-called ‘asymmetric resistivity’ and could account for 100% of the driven current. The action of the lower hybrid wave is to accelerate electrons from a velocity  $v_{\parallel}$  parallel to the magnetic field, to a velocity  $v_{\parallel} + \Delta v_{\parallel}$ . This requires an incremental energy input per unit volume

$$\Delta E = n_e m_e v_{\parallel} \Delta v_{\parallel}. \quad (67)$$

Assuming that the velocity of an electron  $v$  is randomized by collisions on a

momentum destruction timescale  $1/\nu(v)$ , this incremental energy input produces an incremental current density  $j$  that persists for a time  $1/\nu$ :

$$j = n_e e \Delta v_{\parallel} = \frac{\Delta E e}{m_e \nu_{\parallel}}. \quad (68)$$

The power density required to refresh this current at time intervals of  $1/\nu$  is

$$p_d = \nu \Delta E. \quad (69)$$

Hence, the current drive efficiency is given by:

$$\frac{j}{p_d} = \frac{e}{m_e \nu_{\parallel} \nu}. \quad (70)$$

Assuming that the thermal velocity of the electron is negligible compared to  $v_{\parallel}$ , *i.e.*,  $v_{\parallel} \gg v_{Te}$ , and  $\nu \propto 1/\nu_{\parallel}^3$  we get:

$$\frac{j}{p_d} \propto \nu_{\parallel}^2. \quad (71)$$

## 5. Current Drive efficiency

This simple treatment in the previous section serves to illustrate the important influence of collisionality leading to a strong dependence of the current drive efficiency on the parallel electron velocity and hence the parallel wave phase velocity (since the parallel phase velocity  $\omega/k_{\parallel} = v_{\parallel}$  at Landau resonance, where  $k_{\parallel}$  is the parallel component of the wave-vector).

To find the current drive efficiency [2]  $\eta_{CD}$  we treat the velocity in a two-dimensional space and we present the normalized parameters

$$u = \frac{v}{v_{Te}}, \quad J = \frac{j}{n_e e v_{Te}} \quad \text{and} \quad P_d = p_d / (n_e m_e v_0 v_{Te}^2).$$

Applying the LH wave condition where the propagation in the perpendicular direction is negligible with respect to the parallel direction,  $u_{\parallel} \gg u_{\perp}$ , we get

$$\frac{J}{P_d} \propto u_{\parallel}^2 \propto \frac{(\omega/k_{\parallel})}{v_{Te}^2}. \quad (72)$$

So, the efficiency  $\eta_{CD}$  of any current drive method in practical units is:

$$\eta_{CD} = \frac{I_P}{P} = \frac{A j}{2\pi R A P_d}, \quad (73)$$

or

$$\eta_{CD} = \frac{I}{P} = 0.061 \frac{T_e}{R(n_e/10^{20}) \ln \Lambda} \left(\frac{J}{P}\right) \text{AW}^{-1}, \quad (74)$$

where  $I_P$ : The total driven current in the plasma in amperes.

$P$ : Total power in watts.

$A$ : The plasma cross-section area in  $\text{m}^2$ .

$R$ : The major radius of the tokamak.

This is not the case for most other schemes which do not generate supra-thermal electrons and so have a favorable scaling with the electron temperature  $T_e$ . However, the capability of lower hybrid waves to give high current drive efficiency even in moderate temperature plasmas, due to strong Landau damping on supra-thermal electrons, has resulted in an abundant database of results compared with other schemes, giving rise to the convention of defining a current drive figure of merit in terms of the scaling for supra-thermal electrons, namely

$$\eta_{CD} = \frac{RI_P}{P} \frac{\bar{n}_e}{10^{20}} \text{ m}^{-2} \text{ AW}^{-1}, \quad (75)$$

where  $\bar{n}_e$  is the line average electron density.

### 6. LHCD efficiency in experiments

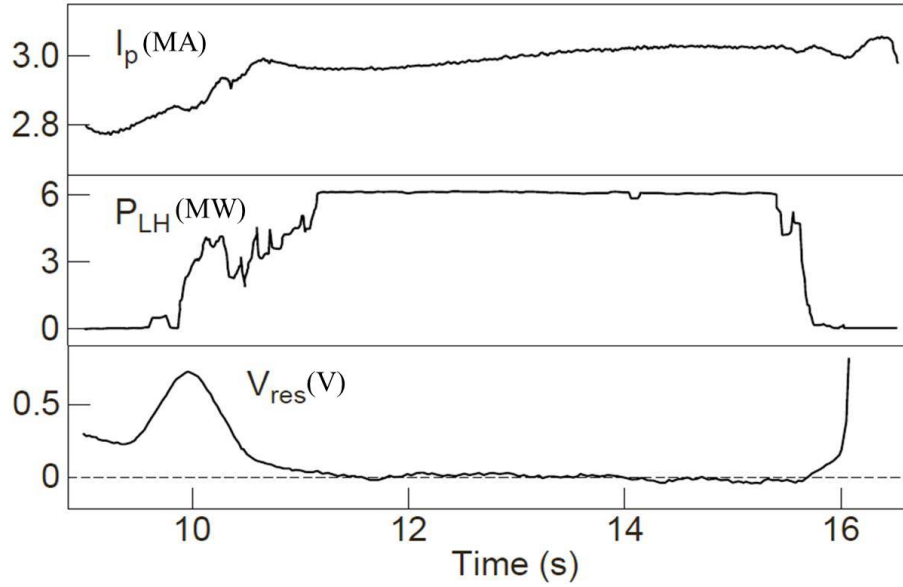


Figure 15: Full sustainment of the plasma current of a 3 MA discharge by the LHCD on JET tokamak.  $I_P$  is the plasma current.  $P_{LH}$  is the lower hybrid power.  $V_{res}$  is the resistive loop voltage, *i.e.*, the corrected loop voltage for inductive effects. It represents the voltage required for the  $I_P$  sustainment. When  $V_{res}=0$ , this means that  $I_P$  is fully sustained by the LH waves [20].

Total plasma current has been driven by the lower hybrid waves in many tokamak experiments. Some experiments have also demonstrated discharge start-up by lower hybrid waves. Plasma currents of 3.6 and 3 MA have been fully sustained by lower hybrid current drive in JT-60U and JET (see Fig. 15), respectively. A current drive figure of merit  $\eta_{CD} > 0.3 \text{ AW}^{-1} \text{ m}^{-2}$  has been achieved in these devices. In TRIAM-1M, a plasma current of 20 kA was sustained for 2 hours while in Tore-Supra a plasma current of 0.8 MA was sustained for 2 minutes by lower hybrid waves. Current drive at high density,  $\sim 10^{20} \text{ m}^{-3}$ , has been demonstrated using high frequency lower hybrid waves in

ALCATOR-C and FTU tokamaks. In present experiments lower hybrid waves typically transit the plasma many times before full absorption occurs. Nevertheless, the effectiveness of lower hybrid waves for control of the radial profile of plasma current has been demonstrated in many tokamaks. As shown above, waves with the highest phase velocity give the highest current drive efficiency but these waves also have the poorest penetration. Although lower hybrid waves are expected to be absorbed in a single pass for plasma parameters characteristic of a fusion reactor, strong Landau damping and mode conversion are expected to limit penetration of the waves to the outer half of the plasma in this case.

## **B. The experimental setup for the LHCD**

### *1. The Lower hybrid Grill*

Lower hybrid waves are launched, in nowadays tokamaks, into the plasma via a phased waveguide array. This mechanism was first suggested by Lallia [21]. The LH grill consists of an array of properly phased waveguides. The wave generators, or Klystrons, are used to feed the waveguides with a transverse electric ( $TE_{10}$ ) mode. In order to have an asymmetric wave spectrum which is necessary for current drive, the phasing between the adjacent waveguides in the same row should be  $\pi/2$  or  $\pi/3$ . It was thought that the vertically adjacent waveguides, that form rows, should be in phase. However, it has been shown that this thought is not mandatory, where no absorption effect was detected for the poloidal wave number [21].

The launching structure as a grill is important since the wave source can be far behind the mouth. The waves are then transmitted to the plasma facing structure through waveguides. A dielectric window separates the vacuum area inside the plasma chamber from the pressurized area outside it. An advantage arises when this window is placed far away from the plasma. This leads to a reduction of the heat and neutron fluxes on the window. Furthermore, the grill can be made of the same material as that of the wall or the



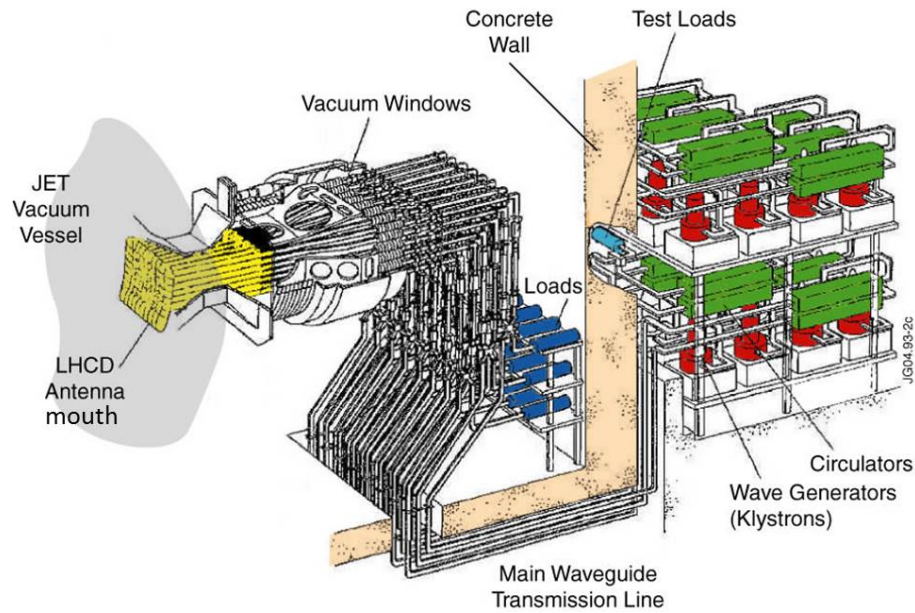


Figure 16: The LH antenna structure on the JET tokamak.

poloidal limiters in front of which it usually is not moved. However, to ensure good RF conductivity, the inner part of the grill must be made of copper. The whole LH antenna is presented in Fig. 16

In large tokamaks, the LH grill that is made of waveguides fed independently would need a few hundreds of waveguides. This is an extremely complex and demanding grill structure to design. Thus, multi-junction grills which was suggested in Ref. [21], is much easier. The waveguides in the multi-junction grill is divided into secondary, but smaller, waveguides with metal walls parallel to the wall of the main waveguide. The height of the secondary waveguides is chosen so that the correct output phasing is obtained for the grill [22].

In the multi-junction grill, the main waveguide is fed with the  $TE_{10}$  mode. This mode is converted inside the waveguides into a  $TE_{30}$  mode in the poloidal mode converters. The power in the incident waveguides is divided into poloidal and toroidal multi-junctions. This division is done by the magnetic and the electric field plane junctions. The  $TE_{10}$  mode is the mode that reaches the grill mouth, due to the division in the poloidal direction into three.

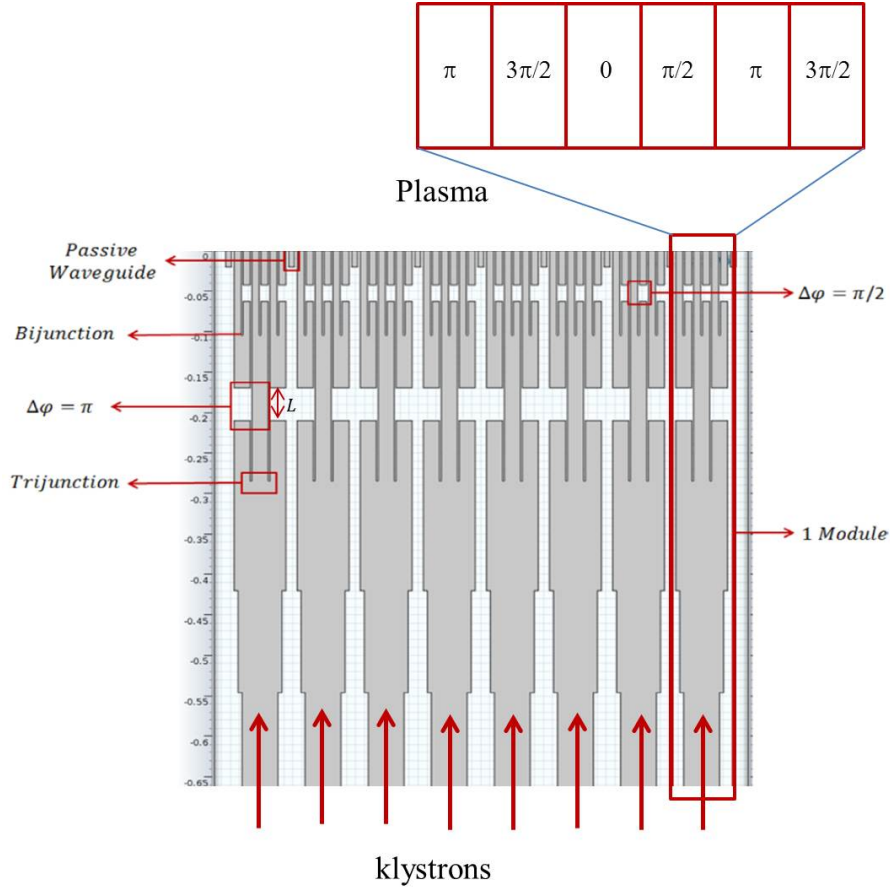


Figure 17: The geometry of the FAM antenna in PICCOLO-2D. One row of eight modules is represented [23].  $\Delta\phi$  is the phase difference between the waveguides. It shows how the klystrons feed the waveguides that form the  $N_{\parallel}$  wave which is necessary for the current drive.

On the Tore Supra tokamak, two LH antennas are installed as shown in Fig. 5. To the right is the  $C_3$  while that on the left is the  $C_4$ . The waveguide rows, mouth and limiters can be clearly seen.

$C_3$  antenna is formed of 4 rows with each having 32 waveguides [5]. The waveguides are divided into modules consisting of two rows of four waveguides. For the multi-junction structure, the toroidal phase difference is  $\pi/2$  between the adjacent waveguides in a module Fig. 17. Moreover, there is a phase shift between the modules which can be varied from 0 up to  $2\pi$ . A  $\pi/2$  phase difference between each waveguide is the result of a zero phase difference between the modules. This case is more favorable for current drive since it optimizes the directivity and the self-matching properties of the

multi-junction [24].

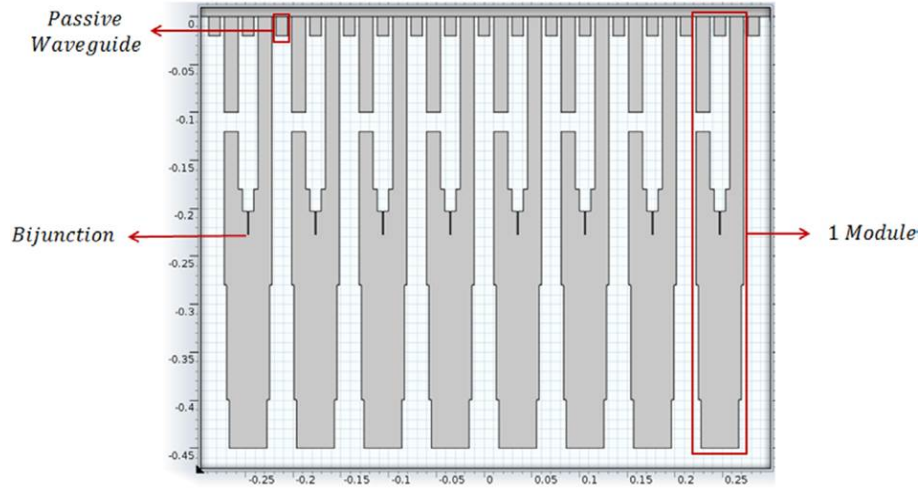


Figure 18: The geometry of the PAM antenna in PICCOLO-2D. One row of eight modules is represented [23].

The grill of the  $C_4$  antenna is made of  $48 \times 6$  waveguides. For this antenna, passive waveguides are used between each module and at the end of the launcher. The passive waveguides are not fed by klystrons. A klystron is a specialized linear-beam vacuum tube used as an amplifier for high frequencies. A klystron amplifies RF signals by converting the kinetic energy in a DC electron beam into radio frequency power. A lower coupled power is resulted from the larger radiating surface in the  $C_4$  launcher with same input power. The density is  $I_{in} = 25 \text{ MW}/m^2$  at 3.7 GHz. Long pulses are allowed from the decreased power density that helps to avoid RF-breakdowns.

The design of the LH grill of the ITER and ITER-like tokamaks is based on the Passive Active Multijunction (PAM). It allows good coupling of the wave and it is efficient in cooling the plasma facing part of the grill [25, 26]. The whole grill for ITER is constructed of four PAM modules. Each module consists of 12 rows of 24 active and 25 passive waveguides in a row [26]. The phase difference between adjacent active waveguides in the row is  $3\pi/2$ .

The issue of launching the  $N_{||}$  spectrum is presented in figures (17) and (18) for the FAM and the PAM launchers. The passive waveguides shown are short waveguides

terminated by a short circuit. The phase shift between the waveguides is obtained by varying the effective length of the adjacent waveguides  $L$ . When a waveguide is shortened by a length  $L = \varphi \times \lambda_0/2\pi$ , the wave phase is changed by  $\varphi$ . The trick is to create a difference in length between the waveguides. For example, if we want to have a phase shift of  $\pi/2$  between two adjacent waveguides, one of the two waveguides will be cut over the distance  $L$  necessary to create a phase delay due to a longer guided propagation in the second waveguide, as described in Fig. (17). A condition of electric field continuity is used to connect the broken waveguide.

## 2. *The $n_{\parallel}$ spectrum*

The dimensions and the frequency of the launcher with the phase difference between the radiating waveguides determine the spectrum of the wave launched by the grill. One can find the main peak that carries most of the power from the following equation:

$$n_{\parallel 0} = \frac{\lambda_0 \Delta\phi}{\Delta z 2\pi}. \quad (76)$$

$\lambda_0 = c/f$  is the vacuum wavelength of the driven wave,  $\Delta z$  is the width of the geometric period of the grill and  $\Delta\phi$  is the phase difference between the two radiating elements. The width of the waveguide, including the wall between the two adjacent waveguides, defines the geometric period.

The position of the peaks of a simple multi-junction with a phase difference  $\Delta\phi = \pi/2$  can be determined from the following formula

$$n_{\parallel m} = \frac{c}{fL_4}m, \quad (77)$$

where  $m$  is the mode number and  $L_4$  is the shortest period of the grill, in other words, the width of 4 waveguides. For a phase difference  $\pi/2$ , the spectrum is asymmetric with only

the odd harmonic present [27], while the even ones are suppressed. As a result, the mode number is  $m = 1 \pm 4\sigma$  with  $\sigma = 1, 2, 3, \dots$

The half width of the peak is also determined from the grill geometry. The full width is inversely proportional to the toroidal width of the launcher [28]

$$\Delta n_{\parallel} = \frac{c}{fL_G}. \quad (78)$$

$\Delta n_{\parallel}$  is the full width at half maximum and  $L_G$  is the full width of the grill. For a PAM,  $L_G = Nd_{act}$  is the width of the actively radiating part of the grill,  $N$  is the number and  $d_{act}$  is the width of the active waveguides. The width is an important parameter for current drive efficiency. The efficiency increases for a smaller width of the main peak. In present day devices, the current efficiency is much better than in the early ones. This is due to that the peak of a 32-waveguide device is narrower than that of a 4-waveguide device [21].

The total launched spectrum will be in the parallel direction with a parallel index of refraction  $N_{\parallel}$ . Figure (19) shows how the  $N_{\parallel}$  spectrum which carries most of the power is launched in the parallel direction [23].

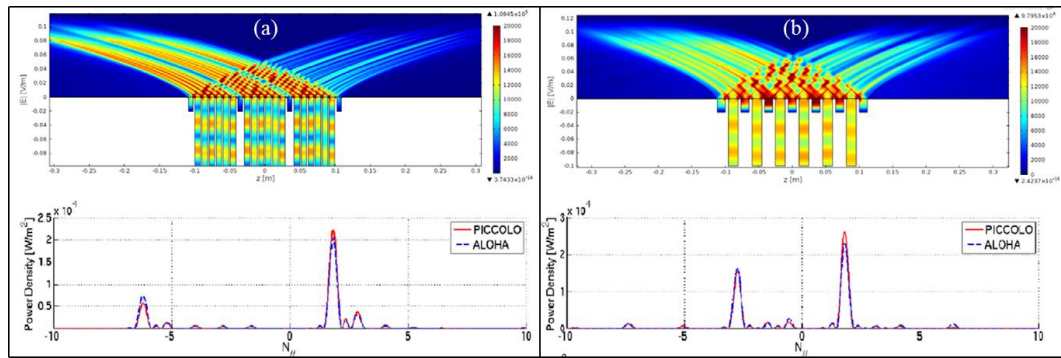


Figure 19: (a), represents the properties of the LH-coupler while (b) represents those of the PAM. The top plots of (a) and (b) represent the amplitude of the electric field in the waveguides and the edge plasma computed by PICCOLO-2D code. The bottom plots shows the spectrum of the electric field at the mouth of the grill [23].

## C. Ion Sound waves

### 1. Introduction

In plasma physics, the ion acoustic wave [8] is one type of longitudinal oscillation of the ions and electrons in a plasma. The ion acoustic waves are the analogy of a compressive sound wave that occurs in air. The ion acoustic waves propagate through positively charged ions. Hence, they can interact with their electromagnetic fields, as well as simple collisions. In plasmas, ion acoustic waves are frequently referred to as acoustic waves or even just sound waves. They commonly govern the evolution of mass density, for instance due to pressure gradients, on time scales longer than the frequency corresponding to the relevant length scale. Ion acoustic waves can occur in unmagnetized plasma or in magnetized plasma parallel to the magnetic field. For single ion species plasma and in the long wavelength limit, the waves can propagate with a speed given by:

$$c_s = \sqrt{\frac{\gamma_e Z k_B T_e + \gamma_i k_B T_i}{M}}. \quad (79)$$

where  $M$  is the ion mass,  $Z$  is its charge,  $k_B$  is the Boltzmann constant and  $T_e$  and  $T_i$  are respectively the electron and ion temperatures.  $\gamma$  is the adiabatic invariant. Next, we derive the dispersion relation of the ion acoustic waves.

### 2. Equations of motion

From the momentum balance equation, one can write the ion equation of motion considering  $n = n_i = n_e$ . We neglect the non-linear term, and hence the equation is,

$$m_i n \frac{\partial \mathbf{v}_i}{\partial t} = en \mathbf{E} - \nabla p_i. \quad (80)$$

using  $\mathbf{E} = -\nabla\phi$  and writing the pressure in terms of the ion temperature  $T_i$  as

$p_i = n_i k_B T_i$ , equation (80) can be written as,

$$m_i n \frac{\partial \mathbf{v}_i}{\partial t} = -en \nabla \phi - \gamma_i k_B T_i \nabla n. \quad (81)$$

Consider the one-dimensional case and assume that all the variables have harmonic solutions, then they are proportional to  $e^{i(\mathbf{k} \cdot \mathbf{r} - \omega t)}$ . The background density is assumed to be isotropic. Neglecting the non-linear terms we finally get

$$-im_i \omega n_0 v_i = -in_0 e k \phi_1 - i\gamma_i k_B T_i k n_1. \quad (82)$$

In the same manner and assumptions, we can write the electron equation after neglecting the non-linear velocity terms,

$$m_e n \frac{\partial \mathbf{v}_e}{\partial t} = en \nabla \phi - \gamma_e k_B T_e \nabla n. \quad (83)$$

Further assumption is made by considering the electron mass is negligible as compared with the ion mass. Thus, we can neglect the term proportional to  $m_e$  on the left of equation (83). The remaining terms give:

$$e \nabla \phi = \gamma_e k_B T_e \frac{\nabla n}{n}, \quad (84)$$

where we can integrate both sides of this equation. Considering the simple one-dimensional case and integrating we get,

$$e \phi = \gamma_e k_B T_e \ln(n) + c \quad (85)$$

The assumption that the electron mass is negligible compared to the ion mass reflects the mobility of the electrons. Hence, electrons are able to equalize any thermal

instability. Thus, electrons behave isothermally, *i.e.*,  $\gamma_e = 1$ . The electron density to the first order obey the Boltzmann-distribution,

$$n_e = n_0 e^{e\phi/k_B T_e} \quad (86)$$

### 3. Acoustic wave dispersion relation

We assume that the perturbations are small relative to the thermal energy. Hence, we can make the previous assumption,  $e\phi \ll k_B T$ , and the Taylor expansion of equation (86) is,

$$n_e = n_0 \left( 1 + \frac{e\phi}{k_B T_e} + \dots \right). \quad (87)$$

Assume that the perturbed density is  $n_1$  and  $n_e = n_0 + n_1$ ,

$$n_1 = n_e - n_0 \approx n_0 \left( 1 + \frac{e\phi}{k_B T_e} \right) - n_0 = n_0 \frac{e\phi}{k_B T_e}. \quad (88)$$

Using the continuity equation which is

$$\frac{\partial n}{\partial t} + \nabla \cdot (n\mathbf{v}) = 0, \quad (89)$$

we expand  $n$  and  $v$  in terms of perturbed quantities to get:

$$\frac{\partial}{\partial t} (n_0 + n_1) + \nabla \cdot ((n_0 + n_1)\mathbf{v}_1) = 0. \quad (90)$$

Neglecting the non-linear term which result from the second term of equation (90), the resulting ion equation for the one-dimensional case is:



$$\frac{\partial n_1}{\partial t} + n_0 \frac{\partial v_i}{\partial x} = 0, \quad (91)$$

where  $x$  is the parallel direction to  $B$ .

Solving this equation for harmonic solutions we get:

$$-\omega n_1 + i k n_0 v_i = 0$$

and hence

$$v_i = \frac{\omega n_1}{k n_0}$$

From equation (88) we finally get the ion velocity in the parallel direction to  $\mathbf{B}$ ,

$$v_i = \frac{\omega e \phi}{k k_B T_e}. \quad (92)$$

We substitute equations (88) and (92) in the ion equation of motion and solve for  $\omega(k)$  to find the dispersion relation as:

$$\omega^2 = k^2 \left( \frac{k_B T_e + \gamma_i k_B T_i}{m_i} \right), \quad (93)$$

or

$$\omega = k \sqrt{\frac{k_B T_e + \gamma_i k_B T_i}{m_i}}. \quad (94)$$

Equation (94) is the dispersion relation for the ion acoustic waves in a plasma. Knowing that the dispersion relation for the usual sound wave is written as

$$\omega = k c_s$$

then the sound speed  $c_s$  is:

$$c_s = \sqrt{\frac{k_B T_e + \gamma_i k_B T_i}{m_i}}.$$

#### D. Parametric Decay Instability

The parametric decay instability (PDI) is a non-linear instability. It was first discovered by Oraevsky and Sagdeev in 1962. The instability starts when the phase and frequency matching are produced for the initial wave, and two other eigenmodes of the system whose amplitudes are initially at the level of thermal fluctuations. The initial wave is usually called the pump wave.

The mechanism of the parametric instability was described by Liu in Ref. [29] as follows: “In the presence of a pump wave the particles acquire an oscillatory velocity  $v_0$ . When this is coupled to a low frequency density perturbation  $n_\omega$ , a nonlinear current  $n_\omega v_0$  is produced which becomes a source to drive the mode at the sideband frequency. The fields and oscillatory velocities at the pump and sideband frequencies beat to produce a low frequency ponderomotive force on the particles, driving the low frequency perturbation.” This ponderomotive force is defined as,

$$\mathbf{F}_p \equiv -m\mathbf{v} \cdot \nabla \mathbf{v} + (q/c)\mathbf{v} \times \mathbf{B}$$

where  $q$  and  $m$  are the charge and mass of the particles,  $\mathbf{B}$  is the magnetic field of the waves.

According to Oraevsky and Sagdeev 1962 [30], the conditions can be illustrated as:

$$\omega_0 = \omega_1 + \omega_2 \tag{95}$$

$$\mathbf{k}_0 = \mathbf{k}_1 + \mathbf{k}_2, \quad (96)$$

where  $\omega_0$  and  $\mathbf{k}_0$  are the frequency and wave vector of the pump wave, while  $\omega_1$ ,  $\mathbf{k}_1$ ,  $\omega_2$  and  $\mathbf{k}_2$  are the corresponding quantities of the eigenmodes of the medium.

This condition is in agreement with the conservation laws of energy and momentum that hold for decays of quasi-particles. Consequently, and after the work of Oraevsky and Sagdeev, this type of instabilities is traditionally referred to as *decay instabilities* [31].

Moreover, in the same year, the theory of stimulated scattering of the waves was discovered independently in the non-linear optics [32, 33]. It was clear then that the decay instability forms the basis of the stimulated Raman wave scattering process. The features of the stimulated Raman wave scattering were not quite understood. But now, it is understood that they are caused by the nature of wave processes under decay instability. The observation of the exponential (non-linear) growth of the amplitudes of both scattered and incident waves shows that it is caused by the decay instability. It is an immediate result of the positive feedback of the incident and scattered waves propagating against the background of the pump wave. This relation is described by the equations that represent a spatial-temporal generalization of the Hill equations. Moreover, the corresponding instabilities are naturally classified as parametric instabilities. In general, these parametric instabilities are of the form:

$$n\omega_0 = \omega_1 + \omega_2 \quad (97)$$

$$n\mathbf{k}_0 = \mathbf{k}_1 + \mathbf{k}_2, \quad (98)$$

with  $n=1, 2, 3 \dots$

Decay instabilities are the first order instabilities, *i.e.*,  $n=1$ . In the absence of

decay instability, second order instabilities arise [34].

Following the qualitative theory presented in Ref. [31] (see Appendix) we can find the dispersion relation of the parametric decay instability. The solution is written using the decay conditions equation. The solution found is

$$\left\{ \begin{array}{l} a_1 \sim \exp[-i\frac{\Delta\omega}{2}t + \nu t] \\ a_2^* \sim \exp[i\frac{\Delta\omega}{2}t + \nu t] \\ \nu = \sqrt{\gamma_D^2 - (\frac{\Delta\omega}{2})^2} \quad \gamma_D^2 \equiv \frac{\epsilon^2 k_1^2 k_2^2 V^2 \Phi_0}{16\omega_1 \omega_2} \end{array} \right. \quad (99)$$

It describes the so-called parametric decay instability. Thus when the conditions for the decay instability are satisfied, the amplitudes of waves  $a_1$  and  $a_2$  will grow exponentially with the increment  $\nu = \gamma_D$ , and thus the product  $\omega_1 \omega_2 > 0$ . Finally, we get the following inequality

$$\omega_1, \omega_2 < \omega_0$$

which tells us that the decay instability excites lower frequencies.

Furthermore, PDI thresholds are determined in the appendix and conditions for instabilities are mentioned.

### ***1. The PDI near the LH frequency***

In Ref. [35] the dispersion relation of the parametric decay instability is derived near the lower hybrid frequency. The calculation of the dispersion relation starting by treating the pump wave in the dipole approximation

$$\mathbf{E} = \mathbf{E}_0 \cos(\omega_0 t), \quad (100)$$

where  $\mathbf{E}_0$  may be either a plane wave or circularly polarized wave, the charge density  $\rho$  is determined by solving the Vlasov and Poisson equations. Then by applying several approximations on the system, the final dispersion relation obtained is

$$\varepsilon(\omega) + \frac{\mu^2}{4} \chi_i(\omega)(1 + \chi_e(\omega)) \left( \frac{1}{\varepsilon(\omega - \omega_0)} + \frac{1}{\varepsilon(\omega + \omega_0)} \right) = 0, \quad (101)$$

where  $\chi_i$  and  $\chi_e$  are respectively the ion and electron susceptibilities.  $\varepsilon(\omega)$  is defined as

$$\varepsilon(\omega) = 1 + \chi_i(\omega) + \chi_e(\omega),$$

and  $\mu$  is the coupling coefficient between the low-frequency modes ( $\omega \ll \omega_0$ ) and high-frequency sidebands ( $\omega \pm \omega_0$ ) where it was assumed in this calculation weak to intermediate coupling  $\mu < 1$ .

Equation (101) is analyzed in Ref. [35] with frequencies  $\omega \simeq \omega_{LH}$  such that  $m_i/m_e \cos^2 \theta \leq 1$ . Several approximations were done to find the threshold and growth rates for the non-resonant decay instabilities.

One of the examples is the kinetic quasi-modes where the condition taken is  $T_i \simeq 0$ . The conditions on the susceptibility are presented in order to find the real and imaginary part to find its value in the dispersion relation equation (101). The first term of equation 101) cancels out according to the lower order expansion of  $\chi_i(\omega)/\varepsilon(\omega)$  to have

$$1 + \frac{\mu^2}{4} \frac{\varepsilon_e}{\varepsilon(\omega - \omega_0)} = 0. \quad (102)$$

For the case of  $\varepsilon(\omega - \omega_0)$  being near the LH waves for  $\omega - \omega_0 = \omega_2$  we get

$$\omega \simeq (\delta_2 - i\gamma_2 - i\gamma) \frac{\partial \varepsilon}{\partial \omega_2}, \quad (103)$$

where

$$\delta_2 = \frac{\varepsilon_R(\omega_2)}{\partial \varepsilon_R / \partial \omega_2}, \quad \gamma_2 = \frac{\varepsilon_{Im}(\omega_2)}{\partial \varepsilon_R / \partial \omega_2},$$

where  $\gamma$  is the growth rate.

$-\gamma$  in equation (103) represents the linear damping of the sideband, and  $\delta_2$  represents a mismatch from exact resonance.

### E. Ion sound waves and PDI in the LH range

In the literature, several papers and publications discussed the parametric decay instability and its relation to the ion sound waves, also known as ion sound quasi-modes (ISQM), in the lower hybrid experiments. Theory of parametric instability near the LH frequency [36, 35] and its excitation of ion sound quasi-modes during LH heating [37] was studied theoretically and numerically. More theory was done on PDI and its excitation in the presence of the LH waves, where dispersion relations were calculated and numerical solutions were presented [37, 38, 39]. Based on its dispersion relation, a parameter study of the PDI during the LH wave was done in Ref. [40, 41, 42]. It was found that the PDI decaying to ISQM dominates at lower  $n_e$ , while at higher  $n_e$  the dominant is the PDI decay to ion cyclotron quasi-mode [40].

On the other hand, experiments have detected the presence of parametric decay instability and ion sound waves (ISQM) during LH experiments. The parametric excitation of ion acoustic waves by high frequency electric field was experimentally observed

in Ref. [43]. Moreover, the parametric decay of lower hybrid pump in the range of low frequencies is also studied [44] where it was shown from the numerical results of the dispersion relation that an (ISQM) can excite a PDI with certain growth rates. The RF power thresholds for the PDIs driven by the (ISQM) were estimated. Besides, a broadening of the pump RF wave due to the PDI excited by the (ISQM) was detected on the FTU tokamak [45, 44, 46, 47, 48]. On the ALCATOR C-MOD, the ion cyclotron PDI is found to be excited at the inner as well as at the outer plasma edge of the tokamak [49].

In the next chapter, we present part of the results that were obtained from our analysis. These results are new and thus will be submitted for publication in a peer reviewed journal. We show that the instability caused by the LH waves interaction with the plasma is a non-linear instability, namely PDI. Moreover, we detect a coherent mode which is revealed in the power spectrum plot and we present its waveform using the cross-correlation coefficients. It turned out that this coherent mode is an ion sound wave or ion sound quasi-mode. The velocity, the frequency and the wavelength of this wave are calculated to assure the ion sound wave properties. A comparison between the effect of SOL turbulence and the effect of this wave is performed. It is thought that a coupling happens between LH pump waves and plasma perturbations leading to a PDI that excites this ion sound quasi-mode (ISQM). Furthermore, a parametric study is done for the SOL turbulence properties in order to investigate its modifications in the presence of the LH waves. All results and discussions are presented in the next chapter.

## CHAPTER IV

# THE INTERPLAY BETWEEN THE LOWER HYBRID HEATING AND PLASMA TURBULENCE IN THE SCRAPE-OFF LAYER OF THE TORE SUPRA TOKAMAK

### A. Introduction

The need for non-inductive plasma current generation and its control are crucial to ITER-like tokamaks. Several methods are used today to this end like the neutral beam injection (NBI) or the electron cyclotron emission (ECE). Lower hybrid (LH) waves [50, 51, 52] have proven to be one of the most efficient techniques for current drive [2]. Due to the Landau damping process, electrons at the tail of the distribution gain energies from these waves. They are accelerated preferentially in one direction resulting in a net current generation. LH waves can also drive off-axis current non-inductively, hence, becoming a key tool not only for sustaining long pulses in the perspective of steady-state operation [53] but also for the current profile control which has an effect on the confinement properties [54].

The launcher is formed of a set of phased waveguide antennas which define the spectrum of the refractive index component along the toroidal direction  $n_{\parallel}$ . The coupling to the lower hybrid plasma wave, which are slow plasma modes, is achieved when the Stix-Golant accessibility condition  $n_{\parallel} > 1 + (\omega_{pe}^2 / \omega_{ce}^2)_{res}$  is satisfied;  $\omega_{pe}$  and  $\omega_{ce}$  are respectively the electron plasma and cyclotron frequency. As the power of the lower hybrid is increased, more attention was paid to the instabilities which lead to a transfer of the LH power to other modes which cannot be used for the current drive. It was suggested that the parametric decay instability (PDI) [35, 55, 56, 29, 37, 44, 46, 57] is an efficient



way for this decrease. The PDI is a non-linear wave interaction between the LH wave with the background of the density fluctuations at the edge. It leads to the broadening of the  $n_{\parallel}$  spectrum. It was observed that the effect of the PDI may become stronger at high densities preventing it from penetrating the plasma core [58, 47]. This issue is critical for ITER-like devices which are operating at relatively high densities.

It is now admitted that the confinement, as long as it remains in L-mode, degrades even more with additional power [59].

The main features of the SOL on the FTU tokamak were studied [60]. They are strongly affected by the injection of the LH waves where the power spectra is strongly modified with a decrease of the lower frequencies and the increase of the high ones in agreement with what was later detected in the SOL during ICRH. The magnitude of the fluctuation amplitude drops significantly. They concluded that governing parameters appear to be the density at last closed flux surface (LCFS), which could determine the perpendicular wave vector of the LH waves and the collisionality.

On the Tore Supra tokamak, the behavior of the edge plasmas during the LHCD experiments was investigated [61]. The SOL was rather briefly analyzed using Langmuir probe where the power spectra of the fluctuations was detected to have higher levels of fluctuations when compared to ohmic and the opposite is for the low frequency part. The usage of a high-frequency data acquisition system allowed the observation of a coherent mode at 1.7 MHz.

The scrape-off layer turbulence and transport in Tokamak Chauffage Alfvén Brésilien (TCABR) before and during the launching of radio frequency excited waves that interact with the boundary plasma. It was found that during the RF period, the plasma turbulence intensity increases as well as the high-frequency components of the fluctuations. On the other hand, the transport radially convected by the intermittent fluctuation bursts also increases when the RF perturbation is present.

This article is dedicated to the characterization of the SOL in the presence of LH

waves. Next section is dedicated to presenting the experiments as a function of density and power. The statistical properties of the turbulence measured by fixed probes in the SOL will be discussed in section 3 as a function of power and those as a function of density in section 4. In the two main sections, we shall be analyzing the probability distribution function (PDF) and its moments, the power spectrum and the cross-correlation between the two toroidally distanced probes. In the conclusion, the main findings are summarized where it is shown that turbulence increase linearly with the power in agreement with the confinement degradation with increasing power.

## B. The experimental scenarios

The experiments studied here are performed on the Tore Supra tokamak with a plasma current of 0.7 MA for the power scan and 1 MA for the density scan. The toroidal magnetic field is  $B_0=3.8$  T, with a major and minor radii of respective magnitudes 2.4 and 0.7 m. For the density scan, the core plasma density range is  $4.5 - 6 \times 10^{19} \text{ m}^{-3}$ , while the SOL plasma density range is  $1.5 - 4.2 \times 10^{19} \text{ m}^{-3}$  leading to a range in density when normalized to the Greenwald density,  $n_G = I_p^2 / \pi a^2$ , equal to  $[0.2 - 0.5]$ . On the other hand, the total power ranges between 0.6 and 3.7 MW for the power scan and it is being done under constant plasma position, density, magnetic field and probe position.

The LH power in the Tore Supra tokamak is delivered by either the PAM (Passive-Active Multi-junction) or by combining the two multi-junction LH launchers  $C_3$  and  $C_4$ . The latter are used in these experiments. The lower hybrid launcher is placed at a toroidal angle  $\phi = 190^\circ$ . The launchers are retracted with respect to the LCFS by a distance varying between 4 and 8 cm. The nominal peak of the  $N_{||0}$  spectrum launched by the PAM is at  $N_{||0} = 1.72$ .

Two fixed Langmuir probes are positioned on the  $C_4$  lower hybrid coupler at the mid-plane in-between the two ICRH antennas  $Q_5$  and  $Q_1$  [10]. Langmuir probes

measure plasma density fluctuations and thus are different from RF probes which measure the electric field perturbations. A constant bias of -100 V is applied, leading to signals reflecting the ion saturation current  $I_{sat}$ . The probes are compensated electrically for the RF fields up to 200 MHz. The probes are flush mounted with a diameter of 5 mm and their radial position is 3.164 m from the torus axis, whereas the lower hybrid launcher side protection tiles are located at 3.156 m, that is 8 mm in front of the probes. The LCFS is at 3.085 m apart from the axis of the torus; hence, the probes are not in direct interaction with the RF field but could detect the effects of the LH waves as the plasma is transported radially into the far SOL.

The discharges are sampled with two different ranges of acquisition frequencies. One is called DFLUC, where the ion saturation current is acquired at 1 MHz, with 13600 points per trigger per channel. The other is called DCE-DRE which is acquired at 200 MHz, with 100,000 points per trigger per channel. A high-pass filter is installed on the data acquisition damping fluctuations below 100 kHz. Consequently, DFLUC allows the study of electrostatic turbulent fluctuations occurring at frequencies below 100 kHz. DCE-DRE, on the other hand, allows the study of fluctuations between 0.1 – 100 MHz.

### C. Scrape-off layer properties as a function of the LH power

This section investigates the modifications of the SOL properties as a function of the LH power in the two sampling frequency ranges obtained from DFLUC and DCE-DRE. Several discharges will allow a clear statistical understanding of the SOL properties in a wide range of LH power ranging between 0.6 and 3.5 MW. The discharges used in our analysis are: 47744, 47745, 47746, 47748, 47749, 47750 till 47757. All properties are plotted as a function of the total power  $P_T = P_{OH} + P_{LH}$ , where  $P_{OH}$  is the ohmic power and  $P_{LH}$  is the LH power.

These discharges are maintained at the same edge density in the range:  $n_{edge} =$

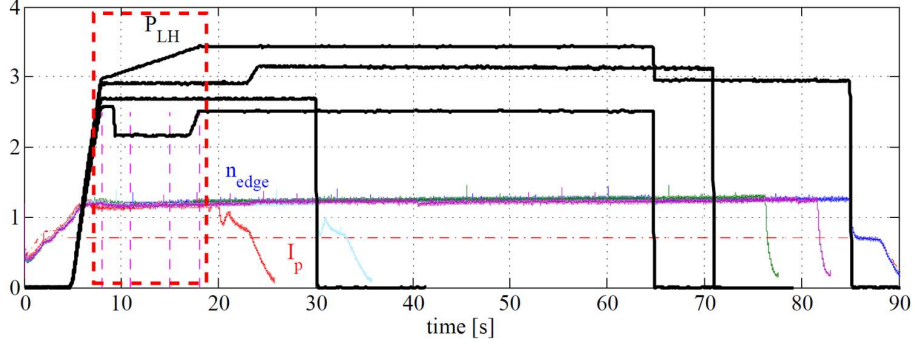


Figure 20: The main plasma parameters are plotted. The vertical dashed pink lines indicates the trigger times at which the data are measured. The edge plasma density  $n_{edge}/10^{19}m^3$  and the plasma current  $I_P$  (in MA) appear to be constant during trigger times. The LH power  $P_{LH}$  (in MW) varies up to a maximum of 3.5 MW for different discharges

$1.1 - 1.2 \times 10^{19} m^{-3}$ . The edge density is obtained from interferometer at  $r/a = 0.8$ . Thus we are inspecting the power dependence without the density contribution. It was verified that the density variations do not affect the results which will be presented as a function of the LH power. Fig. 20 illustrates the main plasma parameters. They are constant over the time domain except for the LH power where multiple discharges are shown for different LH power with a maximum of 3.5 MW. The edge density is plotted for multiple discharges where they are constant with a 10% error. We use three different types of statistical analysis: the PDF and its moments, the frequency spectra  $S(f)$  and the cross-correlation,  $Cx_{12}$ , between the two probes that are toroidally 1 cm apart. The PDF and its moments give strong indications on how the level of fluctuations is modified and how the intermittent bursts are affected when LH power is switched on. The power spectra yield the turbulent structures and their distribution in frequency domain. The cross-correlation is a powerful tool in studying the modification of turbulence with LHCD. It gives a critical understanding about the variations in turbulent structures.

This section consists of four parts. First, we show how the average of  $I_{sat}$  and the level of fluctuations increase in the SOL as LH power increases while the turbulence level remains unchanged. Next, the PDF properties are presented in comparison with normal distribution statistics. Then, we show the modification in the power spectra and

its properties, where an appearance of a coherent mode is detected at 1.7 MHz. Finally, the cross-correlation shows how turbulent structures are affected in their size and velocity below 1 MHz, while a wave form appears for higher frequencies.

### ***1. First two order moments dependence on the LH power***

In order to investigate the turbulence properties in the SOL as LH is turned on, we use DFLUC data which allows us to characterize the turbulent fluctuations in the low frequency range. In this section, we study the first and second order moments of the PDF as a function of the LH power. The first order moment of the PDF is the average value of the ion saturation current  $\langle I_{sat} \rangle = \langle An\sqrt{T_e} \rangle$  which is proportional to the plasma density,  $n$ , and the electron temperature,  $T_e$ . The averages hereafter are taken with respect to time. The second order moment is the standard deviation which is denoted by  $\delta I_{sat}$  representing mainly the amplitude of the density fluctuations in the SOL. We also study the normalized level of fluctuations  $\delta I_{sat} / \langle I_{sat} \rangle$ , which is the turbulence level.

In Fig. 21(a) the average value  $\langle I_{sat} \rangle$  of the plasma edge density is plotted as function of the LH power. The best fit shows an increase with a square root of the LH power. It was verified that the 10% error caused by the density variations between density shots does not affect these results. A similar behavior for the level of fluctuations  $\delta I_{sat}$  is illustrated in Fig. 21(b), where it also increases as the square root of the LH power. The normalized level of fluctuations  $\delta I_{sat} / I_{sat}$  plotted in Fig. 21(c) is unchanged where it remains almost constant at approximately 0.6. Similar behavior for  $\langle I_{sat} \rangle$ ,  $\delta I_{sat}$  and  $\delta I_{sat} / I_{sat}$  was noticed using the PAM-launcher on the Tore Supra tokamak [62]. The level of fluctuations recorded was constant and nearly 0.5.

We recall that the average plasma density at the edge did not change systematically with the LH power and the variations are small. On the other hand, the increase of the edge temperature obtained by the electron emission (ECE) diagnostic did not show a

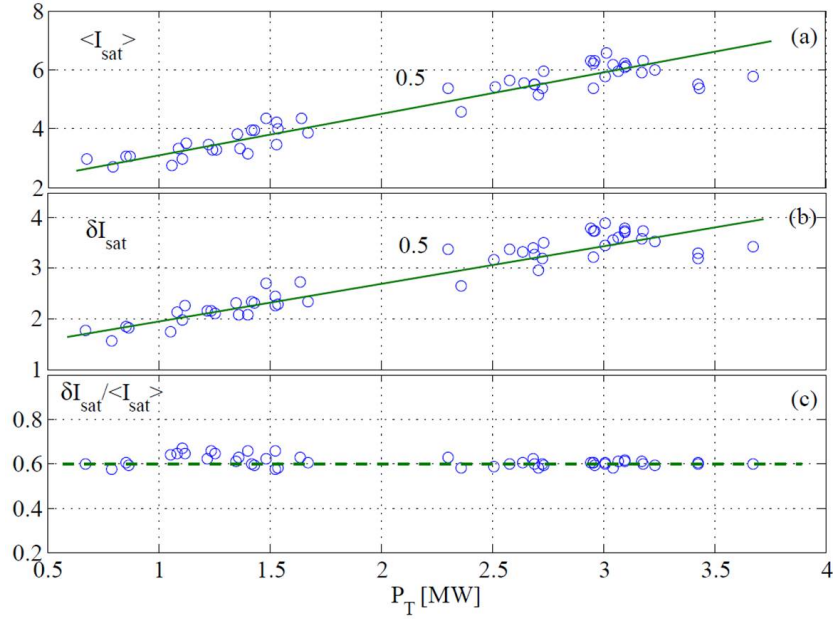


Figure 21: (a), (b) and (c) we respectively plot the average value, the standard deviation (level of fluctuations) and the normalized level of fluctuations of the ion saturation current as a function of the total power  $P_T$ . The circles represent the trigger points while the solid line is their linear fit.

net increase in the edge plasma temperature. The increase in the average value of  $I_{sat}$  may thus have two interpretations: 1- An increase in density or temperature locally in the SOL without propagating into the plasma edge. In this case  $\langle I_{sat} \rangle$ , measured in the SOL, would increase and not  $n_{edge}$  or  $T_{e,edge}$ . 2- A modification in the probe sheath caused by the LH electric field. This would lead to an increase of the effective collection area  $A$  with the LH power.

More work on data is needed in order to pin point which mechanism is responsible for the increase with LH power of  $\langle I_{sat} \rangle$ .  $\delta I_{sat} / I_{sat}$  is constant, reflecting an unchanged level of turbulence, which could be predicted since  $\langle I_{sat} \rangle$  and  $\delta I_{sat}$  increases linearly with the same slope.

## 2. The PDF, the skewness and the Flatness behavior with the LH power

The probability density function (PDF) reflects the occurrence of a signal as a function of the amplitudes. The average value of the ion saturation signal is set to 0 in this study by simply applying:  $I_{sat} = I_{sat} - \langle I_{sat} \rangle$ . In figure Fig. 22(a), some modifications on the shape of the PDF are noticed when the LH power is applied. The graph is semi-logarithmic which allows a more straightforward comparison with the Gaussian distribution that has a parabolic shape. Fig. 22(a) shows that as we increase the LH power, positive values are occurring less frequently while negative values remain unchanged. This leads to a shrinkage in the tail and a slightly more symmetric PDF.

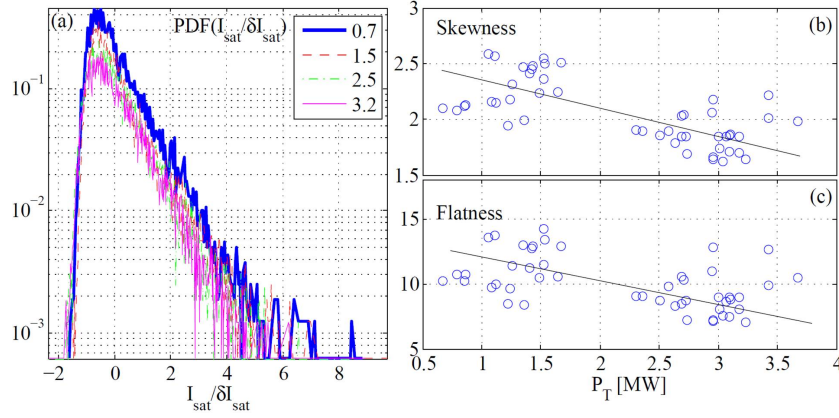


Figure 22: In (a), we plot the PDF of the ion saturation current normalized by its standard deviation for different LH powers. Note that as LH power increases (from thick blue to thin magenta), the probability of positive events decrease while that of negative events slightly increase. In (b) and (c) the skewness and the flatness are shown as function of the total power where the circles indicate the values and the thick lines are their linear fit.

In order to quantify the modifications of the PDF we plot its higher order moments, the skewness and the flatness. The skewness factor is defined as  $S = \langle I_{sat}^3 \rangle / \langle I_{sat}^2 \rangle^{3/2}$ , which is the normalized third order moment of the PDF reflecting the asymmetry of the distribution around the average value. The flatness, also known as the *kurtosis*, is defined as  $F = \langle I_{sat}^4 \rangle / \langle I_{sat}^2 \rangle^2$  is the normalized fourth order moment of the PDF which characterizes the weight of the tail of a certain distribution. We are thus interested in the statistics of high-intensity events. In a Gaussian distribution, which is symmetric and centered around the mean, the skewness and flatness factors are 0 and 3 respectively.

In figure Fig. 22(b) positive values of the skewness reflects a positively skewed PDF from the normal values. The skewness decreases slightly from about 2.5 to about 1.5 tending to be more Gaussian as the LH power increases. The flatness, shown in Fig. 22(c), also drops as we increase the LH power from  $\sim 13$  to about 7 after the LH power is turned on.

As mentioned before, the skewness measures the asymmetry of the distribution around the mean value. The positively skewed values reflect an asymmetric curve that tends to be slightly more symmetric as the LH power increases. Intermittent bursty events, called avaloids or blobs, are the main cause of the positive events. They appear to decrease slightly in the presence of the LH waves. Moreover, the decrease in the flatness values from  $\sim 13$  to  $\sim 7$  reflects values closer to 3. This decrease in the skewness and the flatness in the presence of the LH waves leads to a more symmetric distribution and hence a behavior closer to a Gaussian distribution.

It was found for ohmic plasmas that the SOL turbulence contains intermittent bursts which are caused by large-scale structures that exit the plasma with high radial velocities that reach one-tenth of the sound speed [17, 18]. These bursts will result in positively skewed PDFs with skewness and flatness values greater than 0 and 3 respectively.

The larger the skewness and the flatness are, the more the PDF is asymmetric with more high-intensity events, thus the radial transport is more dominated by convective transport [17]. Hence, this slight drop in skewness and flatness could be interpreted as caused by the injection of the LH power leading to less radial transport due to convection and more contributions to the diffusive transport.

### **3. The power spectra $S(f)$ as a function of power**

In this section we analyze the power spectra for the normalized ion saturation current  $I_{sat}$  which is defined as  $S(f) = \frac{1}{\delta I} \left| \int_{-\infty}^{+\infty} e^{-i\omega t} I(t) dt \right|^2$ . The power spectrum quanti-



fies the distribution of the turbulent fluctuation frequencies as a function of the LH power. In the low frequency range, below 1 MHz, one scaling region in the ohmic L-mode case and even in between ELMs (Edge localized modes) was detected in Ref. [63] with a slope of  $-1.6$ . This was obtained on the FTU tokamak in [64] and later on confirmed on the Tore Supra tokamak in [10].

When using DFLUC, we show how the turbulent structures are modified, and how turbulent events occurring at high and low frequencies are modified. On the other hand, in the high frequency domain, resolved by DCECRE in our case, it was proven that ICRH wave undergoes a parametric decay instability that excites ion sound waves at 1.7 MHz as it interacts with SOL turbulence [65]. We confirm the existence of the ion sound waves at 1.7 MHz when LH waves interact with the SOL turbulence.

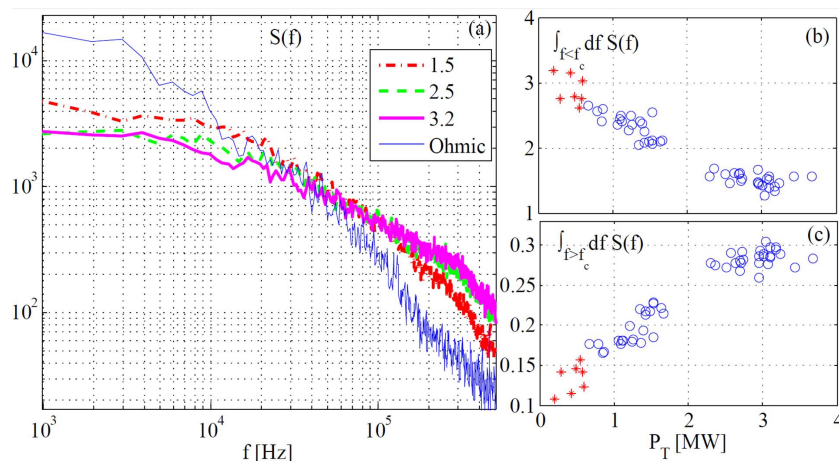


Figure 23: The power spectrum  $S(f)$  using DFLUC for the normalized ion saturation current by its standard deviation is shown for the two cases in a log-log frame. The ohmic case (in thin blue) and with increasing LH power (thick colors), where we notice the decrease in the low-frequency range ( $f < f_c = 50$  kHz) and the increase in the high-frequency range ( $f > f_c = 50$  kHz). This behavior is quantified by the power integration below and above  $f_c = 50$  kHz where the results are plotted in (b) and (c) as a function of  $P_T$ . The stars ‘\*’ denote the ohmic plasmas while the circles ‘o’ denote plasmas with LH power.

In Fig. 23,  $S(f)$  is plotted using DFLUC for different LH powers. It shows that as the LH power increases, low-frequency events decrease while the high-frequency events increase. This modification can be interpreted as a net increase and decrease in the fluctuation amplitudes at low and high frequencies respectively.

The increase and decrease in the two frequency ranges are quantified by integrating the power spectra over frequencies above and below  $f_c = 50$  kHz at which the behavior of  $S(f)$  changes in the presence of the LH power as shown in Fig. 23(b) and (c). The stars indicate the ohmic shots and circles are with LH power. A factor of three is recorded in the decrease and increase of the fluctuation amplitudes below and above  $f_c$  with a linearly decreasing and increasing manner, respectively.

This decrease (increase) in the low (high) frequency events indicates that LH power affects all scales. These modifications of the power spectrum that were quantified through the power integration could be caused by one of these two causes:

- Modifications in the spatial scales of the turbulent structures where a net decrease of the large-scale fluctuations would be happening.
- Modifications of the structures' average velocities which would lead to a shift of the amplitudes from low to high frequency.

In Fig. 24(a)  $S(f)$  is plotted in the frequency domain using DCEDRE ( $1 < f < 10$  MHz) where in the range  $10 < f < 100$  MHz it is verified that no systematic plasma fluctuations are detected. The major indication that can be noticed from the plot is the appearance of a peak at 1.7 MHz.

The frequency spectra decrease till the frequency 1.5 MHz where they undergo a rapid increase forming a spike that is clearly seen at 1.7 MHz. This coherent mode is caused by the injection of the LH power and not due to instrumental noise, where the noise spectrum (thin green), when no plasma is yet created, shows nothing at 1.7 MHz. However, when LH power is switched on, the coherent behavior appears at 1.7 MHz, and as  $P_{LH}$  increases, the amplitude of this mode increases leading to the appearance of another spike at maximum  $P_{LH}$ .

In order to assess the relative amplitude of the peak at 1.7 MHz, we integrate the

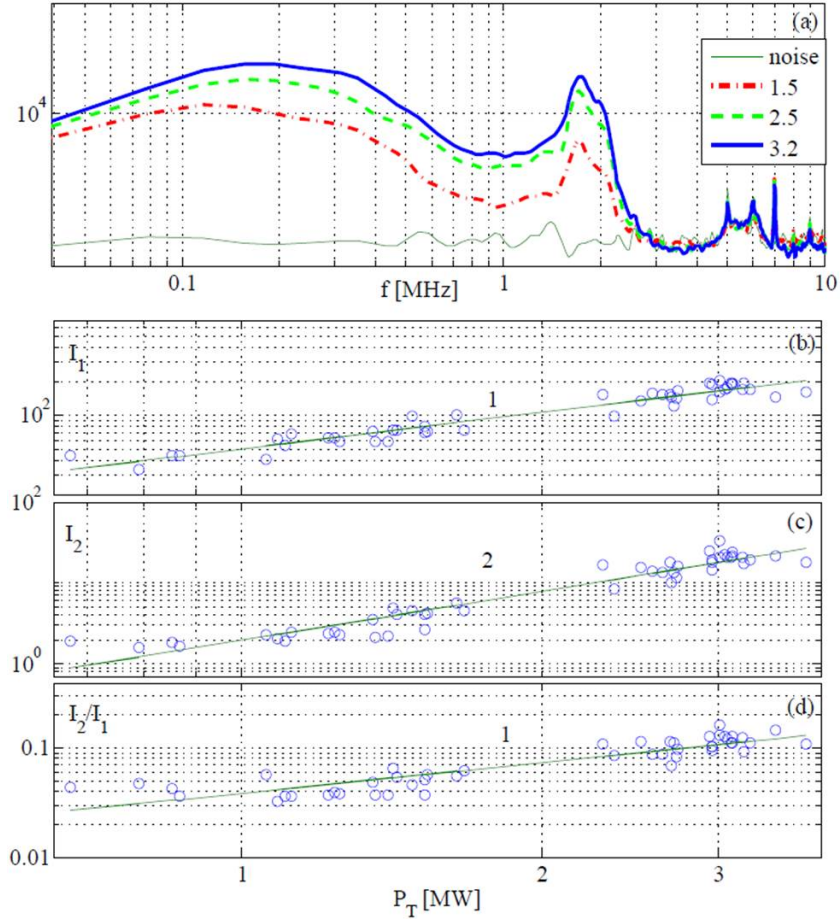


Figure 24: In (a), the power spectrum using DCEDRE for different LH powers and the noise spectrum is plotted in frequency range  $0 < f < 10$  MHz. We assess that the coherent mode at 1.7 MHz is not due to instrumental noise (thin green) but due to the LH power. (b), (c) and (d) respectively show  $I_1$ : the integration of non-normalized  $S(f)$  using DFLUC below 1 MHz,  $I_2$ : the integration of  $S(f)$  using DCEDRE between 1 and 3 MHz, and  $I_2/I_1$  vs.  $P_T$ .

power spectra according to

$$1/(f_2 - f_1) \int_{f_1}^{f_2} S(f) df$$

in the 1-3 MHz frequency range, which is accurately determined by DCEDRE and plotted in Fig. 24(b). On the other hand, the integration determined by DFLUC,  $I_1$ , using the non-normalized spectra in the frequency range 0-0.5 MHz is plotted in Fig. 24(c). The normalization of  $I_2$  by  $I_1$  is plotted in Fig. 24(d). In this way we are interested in the relative intensity of the fluctuations around 1.7 MHz, obtained by  $I_2$ , with respect to turbulence, determined by  $I_1$ . The ratio  $I_2/I_1$  is obtained and shown in Fig. 24(d).

Fig. 24(d) shows a linear increase from about 0.03 to 0.1, which clarifies the importance of the 1.7 MHz peak in affecting the SOL turbulence with a higher contribution to the wave. Consequently, This linear increase in  $I_2/I_1$  assess that as the LH waves interact with SOL turbulence, they undergo a PDI that excites a sound wave at 1.7 MHz.

The power integration is the square of the level of fluctuations, *i.e.*,  $\int S(f)df = \delta I_{sat}^2$ . Using DFLUC, the dependence of the level of fluctuations on power was found to be  $P^{0.5}$ . Thus, it is clear why  $I_1$  increases with a power law  $P^1$ . On the other hand,  $I_2$  dependence on power is  $P^2$ , which reflects a non-linear relation between the spectra integration around 1.7 MHz and the LH power. This non-linear behavior assures that LH waves undergo a PDI that excites a sound wave at 1.7 MHz.  $I_2/I_1$  remains much smaller than unity but at higher LH powers it is expected that the coherent fluctuations could dominate as it was recorded when using ICRH [65].

#### 4. The cross-correlation dependence on the LH power

The cross-correlation coefficient is defined as

$$C_{x12} = \frac{\langle I_1(t)I_2(t + \tau) \rangle}{\langle I_1^2 \rangle^{1/2} \langle I_2^2 \rangle^{1/2}}.$$

It is a powerful statistical tool for studying the effect of the LH power on the SOL turbulence. It shows how turbulent structures are modified as they pass the two probes which are toroidally separated by a distance  $d = 1$  cm. The cross-correlation coefficient reflects the modifications in the turbulent structures as they travel from one point to another. Thus we need both probes in order to calculate cross-correlation values unlike the PDF and the power spectra that were calculated using only one probe.

The cross-correlation is studied in the two frequency domains DFLUC, where the properties of the electrostatic turbulence is investigated, and DCEDRE where the properties of the coherent wave at 1.7 MHz are elucidated. We recall that the mean values of

$\langle I_{sat1} \rangle$  and  $\langle I_{sat2} \rangle$  are set to zero before calculating  $Cx_{12}$ .

In Fig. 25(a),  $Cx_{12}$  is plotted vs. time using DFLUC where a comparison with the ohmic case is done. Two aspects are clearly noticed for the  $Cx_{12}$ : the sharp decrease in the width, and almost unchanged amplitudes.

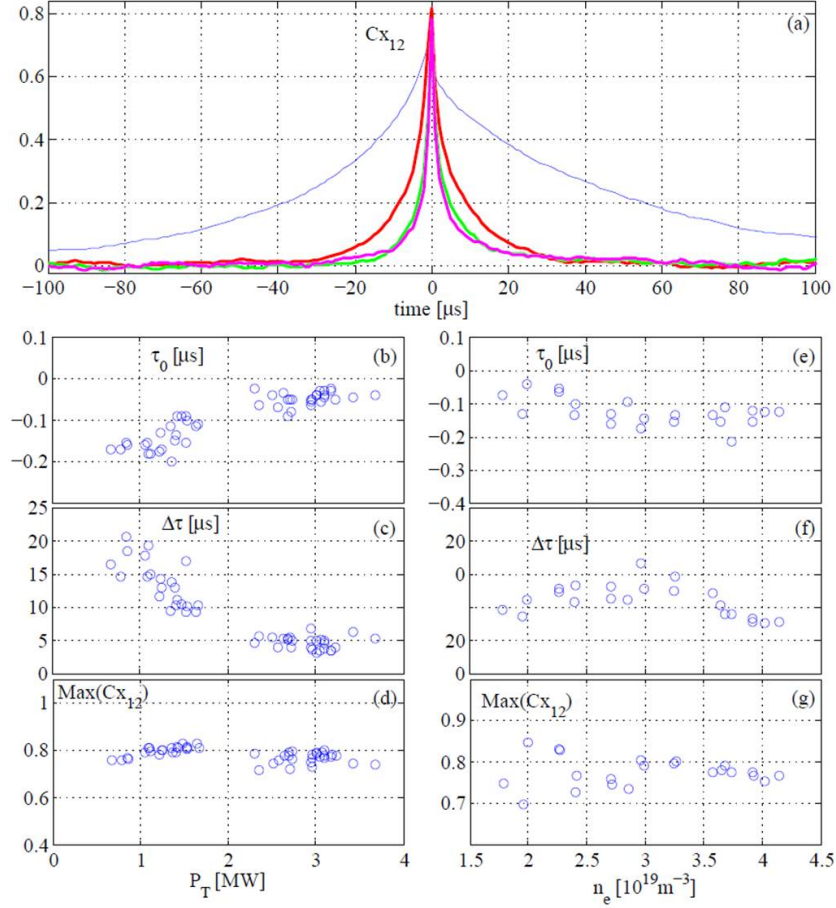


Figure 25: In (a), the cross-correlation coefficient,  $Cx_{12}(\tau)$ , using DFLUC is plotted as a function of time. In (b), (c) and (d) we plot respectively the time corresponding to the maximum amplitude  $\tau_0$ , the width  $\Delta\tau$  of  $Cx_{12}$  and the maximum of  $Cx_{12}$  as a function of  $P_T$ . On the other hand, the same quantities,  $\tau_0$ ,  $\Delta\tau$  and  $Max(Cx_{12})$  are respectively plotted as a function of the edge density  $n_e$  in (e), (f) and (g).

Now, we analyze the cross-correlation properties by plotting  $\tau_0$ ,  $\Delta\tau$  and the cross-correlation maxima  $Max(Cx_{12})$  as a function of the total power using DFLUC. When the LH power is applied,  $\tau_0$  drops, in absolute values, by a factor of three from about -0.15 to -0.05  $\mu s$  as shown in Fig. 25(b). The distance between the two probes is 1 cm, so the calculated toroidal velocities increase from 67 km/s to 200 km/s. These results

are in agreement with the spectroscopic measurements made in the SOL in Ref. [66]. Nevertheless, we can neglect the poloidal velocity contribution which was estimated, for ohmic plasmas, to be  $\simeq 0.5$  km/s [67].

The full width of the cross-correlation  $\Delta\tau$  estimated at  $Max(C_{x_{12}})/e$  is shown in Fig. 25(c). It drops by a factor of 3 from about 18 to about 6  $\mu$ s as the LH power increases. This drop in  $\Delta\tau$  might also reflect the faster convection of the turbulent structures. On the other hand, it also reflects a drop in the spatial size of the turbulent structures or an enhancement for their toroidal velocities or even both since  $\Delta\tau = L/v$  where  $L$  reflects the structure's size and  $v$  is its velocity.

In Fig. 25(c) we plot the maximum values of  $C_{x_{12}}$  where an almost unchanged behavior in the amplitudes is recorded. The amplitude of  $C_{x_{12}}$  is caused by turbulent structures that have an equal or greater size than the distance between the two probes, 1 cm. Moreover, scales of smaller size, yet having high velocities, could be detected by the two probes and hence affecting the cross-correlation amplitudes. Thus, unchanged amplitudes reflect the same number of events that are being detected for different LH powers.

The drop by a factor of three in  $\tau_0$  and  $\Delta\tau$  reflects no change in the spatial size of turbulent structures. This result agrees with the unchanged values of the cross-correlation maxima which reflect size modifications. The increase in the velocity is reflected in the power spectra as a shift which could explain the modifications of  $S(f)$  as seen in Fig. 23(a). On the other hand, modifications on the large and small scales, assuming Taylor's frozen hypothesis, in the power spectrum are not neglected but they appear to be rather minute in the whole frame of the SOL properties analysis. These slight modifications that also agree with those of the skewness and the flatness could be understood in the cross-correlation amplitudes that showed slight modifications. However, the main feature is the increase in the average velocities of these structures that might be causing a constant number of detected events of all sizes.

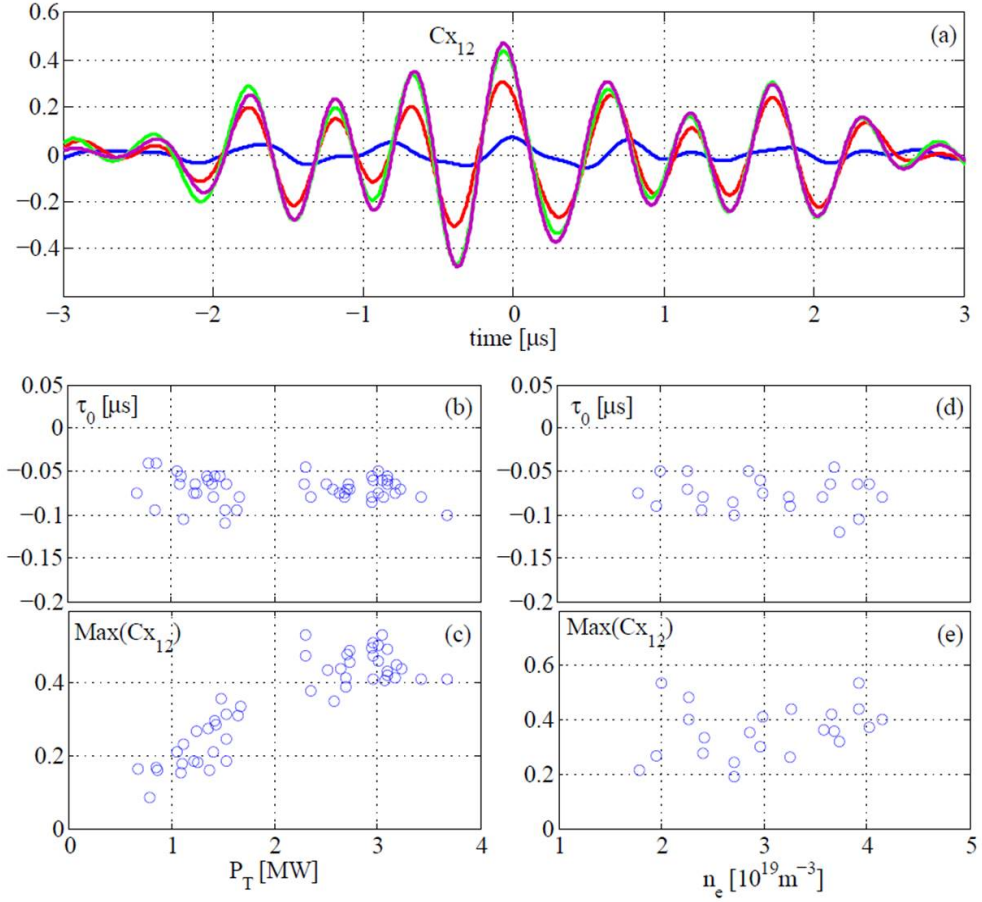


Figure 26: The Cross-correlation,  $Cx_{12}(\tau)$ , for the band-pass filtered data using DCEDRE is plotted in (a) as function of time. The wave structure of  $Cx_{12}$  reflects the appearance of the coherent mode in  $S(f)$  at 1.7 MHz. In (b) and (c) we respectively plot the properties of  $Cx_{12}$  using DCEDRE  $\tau_0$  and the maxima of the cross-correlation coefficients as a function of  $P_T$ , while in (d) and (e), they are respectively plotted, also using DCEDRE, as a function of the edge density  $n_e$ .

In order to understand the properties of the coherent mode that appeared at 1.7 MHz in the power spectrum using DCEDRE, we filter the signal around this frequency then we plot the cross-correlation and its properties in Fig. 26. The first dramatic feature that can be noticed from Fig. 26(a) is the existence of the damped oscillations reflecting a wave structure. This wave can explain the appearance of the peak in the power spectra at 1.7 MHz. However, no oscillations are detected for  $f < 1$  MHz as can be noticed in Fig. 25(a).

The second feature noticed is the negative shift of the time delay  $\tau_0$ . It is defined as the time corresponding to the maximum of the cross-correlation amplitude. It reflects

the average time taken by the structure to move from one probe to another caused by either the toroidal or poloidal motion. Fig. 26(b) shows  $\tau_0$  vs.  $P_T$  that remains unchanged at  $\sim -0.075 \mu\text{s}$  as we increase the LH power leading to average toroidal velocities  $u_0 = d/\tau_0 \simeq 1.3 \times 10^5$  m/s. Thus, we can calculate the wavelength at  $f_s = 1.7$  MHz where it turned out to have a value of  $\lambda_s = u_0/f_s \simeq 7.7$  cm.

The recorded value for  $u_0$  is greater than the observed convective toroidal velocities  $10^4$  m/s and much greater than the poloidal velocities ( $5 \times 10^2$  m/s) [68, 66]. Furthermore, the electron sound wave, the thermal and Alfvén speeds in plasma are so different from our obtained values. The ion sound speed has this order of plasma characteristic velocity ( $\sim 10^5$  m/s), namely  $c_s \simeq 10^3 \sqrt{T_e}$ , where the electron temperature should be  $T_e \sim 100$  eV. This value of  $T_e$  is equivalent to the measured plasma edge temperature and much greater than the SOL temperature. This could mean that the ISQM is excited inside the LCFS and then the perturbations are driven out by radial transport.

On the other hand, the estimated wavelength,  $\sim 7.7$  cm, agrees with the theory where the sound wave excitations are expected after a PDI [69]. Moreover, for tokamak conditions, it was found that the sound wavelength lies between 6 and 10 cm, where the value obtained here experimentally, 7.7 cm, falls within this range. Fig. 25(c) shows an increase in the  $Cx_{12}$  maxima reflecting higher detection of the mode as the LH power is increased, which reflects more contribution to the ion sound quasi-mode with the LH power increase.



#### D. Scrape-off layer properties vs. edge density in the presence of the LH power

The plasma current is set to 1 MA for this study; hence the field lines in front of the fixed mid-plane Langmuir probes are magnetically connected to the active lower hybrid antenna. This section investigates the modifications of the SOL properties as a function of the plasma edge density  $n_{edge}$  in the presence of the LH power. The two sampling frequency ranges, DFLUC and DCEDRE, are studied. Several discharges will allow a clear statistical understanding of the SOL properties in a wide density range  $1.5 < n_{edge} < 4.2 \times 10^{19} \text{ m}^{-3}$  leading to a range in density when normalized to the Greenwald density  $n_G = I_p^2 \times 10^{20} / \pi a^2$  equal to  $[0.2 - 0.5]$ .

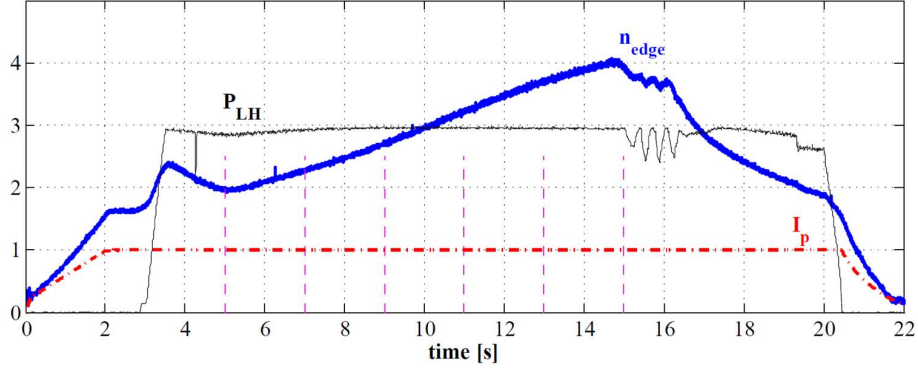


Figure 27: The main plasma parameters are plotted. The vertical dashed pink lines indicates the trigger times at which the data are measured. The LH power  $P_{LH}$  (in MW) and the plasma current  $I_p$  (in MA) appear to be rather constant during trigger times. The plasma edge density  $n_{edge}/10^{19} \text{ m}^{-3}$  varies up to 4.2.

The discharges presented are maintained at roughly the same LH power  $P_{LH} \sim 2.9 \text{ MW}$ , thus we are inspecting the density dependence without power contributions. Fig. 27 illustrates the main plasma parameters. They are rather constant over the time domain except for the edge density  $n_{edge}$  where it varies up to  $4.2 \times 10^{19} \text{ m}^{-3}$ . We use the same three different types of statistical analysis: the PDF and its moments, the frequency spectra  $S(f)$  and the cross-correlation between the two probes that are toroidally 1 cm apart.

This section consists of four parts. First, we show how the average plasma density and the level of fluctuations increase in the SOL as the edge density increases while

the turbulence level remains unchanged. Next, no clear modifications are detected for the skewness and the flatness. Then, we show the modifications of the power spectra and its properties, where the same coherent mode that was detected in the power scan is detected at 1.7 MHz for density scan. Finally, the cross-correlation shows how the SOL turbulent structures are affected.

### **1. First two order moments dependence on $n_{edge}$**

We investigate turbulence SOL properties as a function of  $n_{edge}$  using DFLUC. It shows us the modifications of the turbulent fluctuations in the low frequency range. Hereafter, we will present results for the first two order moments of the PDF, the average value  $\langle I_{sat} \rangle$  and the standard deviation  $\delta I_{sat}$  of the ion saturation current  $I_{sat}$ . Moreover,  $\delta I_{sat}/I_{sat}$  variations as a function of  $n_{edge}$  will show how the turbulence level changes as a function of  $n_{edge}$ .

In Fig. 28(a) the average value  $\langle I_{sat} \rangle$  of the plasma edge density is plotted as function of  $n_{edge}$ . The best fit by a power law gives an exponent equals to 1.5. The same behavior is recorded for the standard deviation in Fig. 28(b).  $\delta I_{sat}/I_{sat}$  is plotted in Fig. 28(c), where it is constant as a function of  $n_{edge}$ . Like the power scan, a similar behavior for  $\langle I_{sat} \rangle$ ,  $\delta I_{sat}$  and  $\delta I_{sat}/I_{sat}$  was noticed as a functions of  $n_{edge}$  using the PAM-launcher on the Tore Supra tokamak [62]. The level of fluctuations recorded was constant and nearly 0.5. The level of fluctuations consequently depends critically on the probe position in the SOL rather than the heating power or average plasma density.

The increase in the average value reflects that more plasma is radially transported from the edge of the confinement zone to the SOL as  $n_{edge}$  increases. A higher level of fluctuations indicates more turbulent structures. The increase in the turbulent structures reflects higher radial transport from the edge to the SOL.

On the Tore Supra tokamak, for the ohmically heated plasmas, the case in which

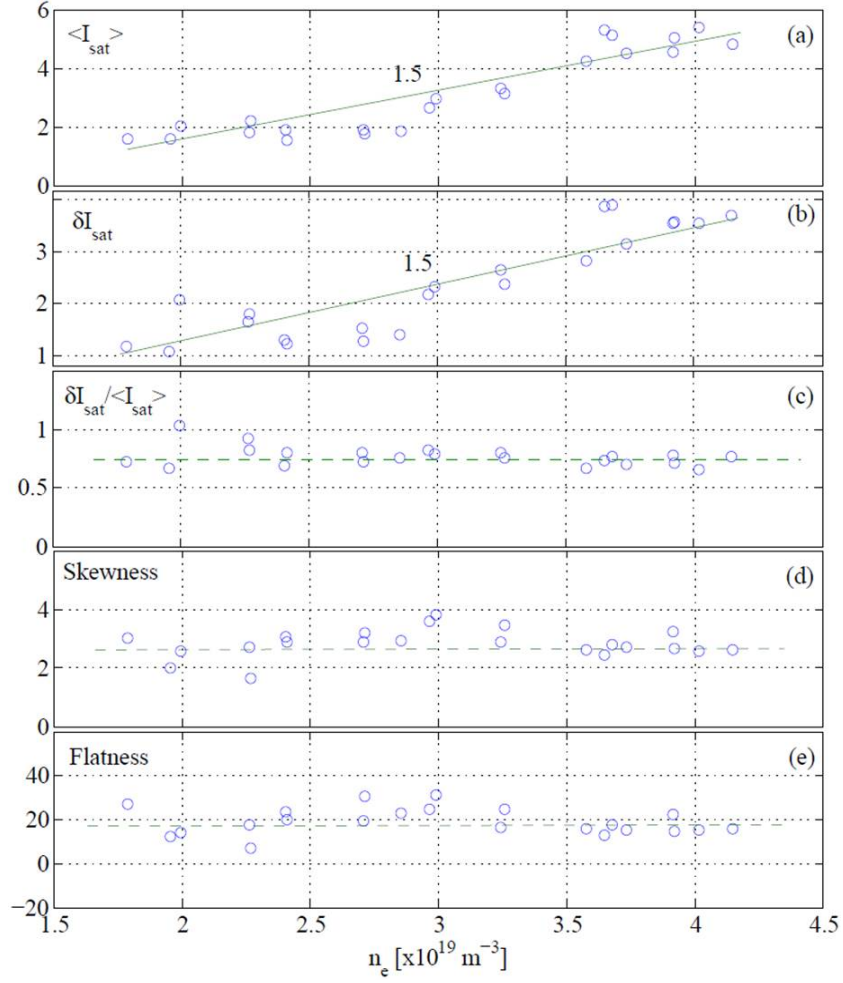


Figure 28: (a), (b) and (c) respectively show the average value, the standard deviation and the normalized level of fluctuations of the ion saturation current as a function of the edge density  $n_{edge}$ . Note that the same linear behavior is noticed for  $\langle I_{sat} \rangle$  and  $\delta I_{sat}$  but with higher slopes, while  $\delta I_{sat} / \langle I_{sat} \rangle$  remains constant at  $\sim 0.7$ . In (d) and (e) the skewness and the flatness are, respectively, plotted as function of  $n_{edge}$  where we note the unchanged behavior of their values.

no additional heating is applied, the increase for  $\langle I_{sat} \rangle$  and  $\delta I_{sat}$  was reported to follow the same slope 1.2 [10], indicating more plasma in the SOL and a slightly higher level of fluctuations. Hence, when applying LH power, a higher rate of increase is obtained,  $\sim 1.5$  for  $\langle I_{sat} \rangle$  and  $\delta I_{sat}$  in comparison to the ohmic case, 1.2. Similar results were reported on MAST tokamak. It was shown that the average value of the ion saturation current  $\langle I_{sat} \rangle$  and the level of fluctuations  $\delta I_{sat}$  increase with increasing normalized density according to the power law  $\sim (n_e/n_G)^{1.5}$  [70].

$\delta I_{sat} / I_{sat}$  is constant, resulting in an unchanged level of turbulence as a function

of  $n_{edge}$ . The value of the level of turbulence as a function of  $n_{edge}$  recorded 0.7 which is roughly the same as in the power scan 0.6. This small difference between the power scan and the density scan is due to the actual probe position in the SOL.

## 2. *The skewness and the Flatness*

The average value of the ion saturation signal is set to 0 in this section by simply applying:  $I_{sat} = I_{sat} - \langle I_{sat} \rangle$ . In order to understand the modifications on the PDF as a function of  $n_{edge}$ , we plot the skewness and the flatness. We recall that the skewness factor reflects the asymmetry of the distribution around the average value as mentioned before. The flatness characterizes the weight of the tail of a certain distribution with respect to the bulk. In a Gaussian distribution, which is symmetric and centered around the mean, the skewness and flatness factors are 0 and 3 respectively.

In figure Fig. 28(d) positive values of the skewness reflects a positively skewed PDF from the normal values. This skewness remains unchanged at a value equals to 3 as  $n_{edge}$  increases. On the other hand, the flatness shows also an unchanged behavior with much higher level than the Gaussian distribution as illustrated in Fig. 28(e). The recorded value of the flatness is around 18.

In Ref. [17, 18] it was found in the ohmic case that SOL turbulence contains intermittent bursts which are caused by large-scale structures that exit the plasma with high radial velocities that reach one-tenth of the sound speed. These bursts result in positively skewed PDFs with skewness and flatness values greater than 0 and 3 respectively. This was confirmed in Ref. [10] where the skewness and flatness factors recorded are 2 and 10 respectively.

The positively skewed values in our case reflect an asymmetric curve that tends to remain asymmetric as  $n_{edge}$  increases. This high level in the skewness and the flatness which is much higher than 0 and 3 respectively quantifies the rate of the intermittent

bursts.

The larger the skewness and the flatness are, the more the PDF is asymmetric with more high-intensity events, thus the radial transport is more dominated by convective transport [17]. Hence, the high skewness and flatness values obtained reflect higher radial transport caused by convection than that caused by diffusion.

### 3. *The power spectra $S(f)$ as a function of $n_{edge}$*

In this section we analyze the power spectra for the normalized ion saturation current. We are interested in the distribution of the turbulent fluctuation frequencies as a function of the frequency and  $n_{edge}$ . In the low frequency range, below 1 MHz, one scaling region in the ohmic L-mode case and even in between ELMs (Edge localized modes) was detected in Ref. [63] with a slope of -1.6, which was shown on the FTU tokamak in [64] and later confirmed on the Tore Supra tokamak in [10].

On the other hand, in the high frequency domain, DCEDRE in our case, it was proven that ICRH wave undergoes a PDI that excites ion sound waves at 1.7 MHz as it interacts with SOL turbulence [65]. This was confirmed in the power scan section of this manuscript. In this section, we show the existence of the ion sound quasi modes at 1.7 MHz when LH waves interact with turbulence in the SOL as a function of  $n_{edge}$ . Moreover, when using DFLUC, we show how turbulent structures are modified, and how turbulent events occurring at high and low frequencies are modified.

In Fig. 29, the integration of  $S(f)$  is plotted using DFLUC. The integration quantifies the behavior of the power spectrum in the two frequency ranges below and above 50 kHz where we have detected a change in the behavior with respect to the power. The integration presented shows how  $S(f)$  is modified as the edge density  $n_{edge}$  increases in the two frequency ranges  $50 \text{ kHz} > f > 0$  and  $0.5 \text{ MHz} > f > 50 \text{ kHz}$ . Fig. 29(a) and (b) illustrate the results of the integration below and above  $f_c = 50 \text{ kHz}$  respectively. No

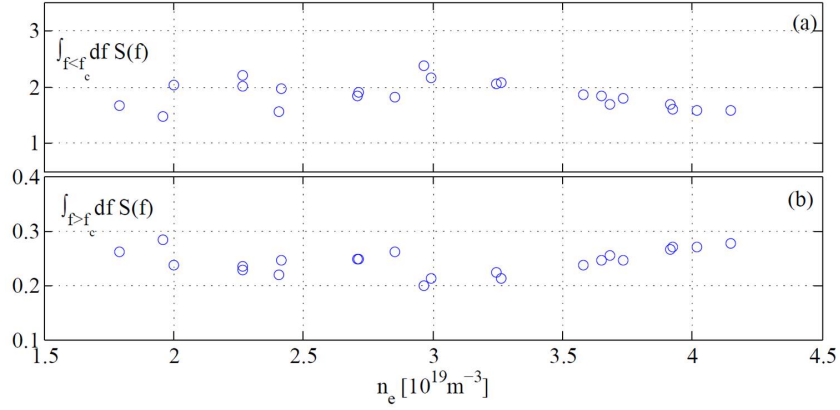


Figure 29: The power integration of the power spectrum below and above  $f_c = 50$  kHz is plotted respectively in (a) and (b) as a function of the edge density. We note that frequencies below 50 kHz decrease while those above 50 kHz increase.

change is detected for both frequency ranges reflecting no dependence on density.

In Fig. 30(a)  $S(f)$  is plotted in the frequency domain using DCEDRE ( $f < 10$  MHz). For the range  $10 < f < 100$  MHz it is verified that no systematic plasma fluctuations are detected that dominate the plasma fluctuations. The major indication that can be noticed from the plot is the appearance of the same coherent mode as in the power scan at 1.7 MHz.

The integration of the power spectra according to

$$1/(f_2 - f_1) \int_{f_1}^{f_2} S(f) df$$

in the 1-3 MHz frequency range  $I_2$ , which is accurately determined by DCEDRE, is plotted in Fig. 30(c). The integration determined by DFLUC in the frequency range 0-0.5 MHz  $I_1$  is plotted in Fig. 30(b). Finally, the normalization of  $I_2$  by  $I_1$  is plotted in Fig. 30(d). We are interested in the relative intensity of the fluctuations around  $f_s$ , obtained by  $I_2$ , with respect to turbulence, determined by  $I_1$ . The ratio  $I_2/I_1$  decreases linearly with a  $-1$  slope. As a function of density, these results reflect that the electrostatic turbulence dominates the coherent mode. The dependence of the level of fluctuations is  $\sim n_{edge}^{1.5}$  whereas for the one associated with the coherent peak it is  $\sim n_{edge}^1$ . Consequently,

a higher dependence on the turbulent fluctuations than on the coherent mode.

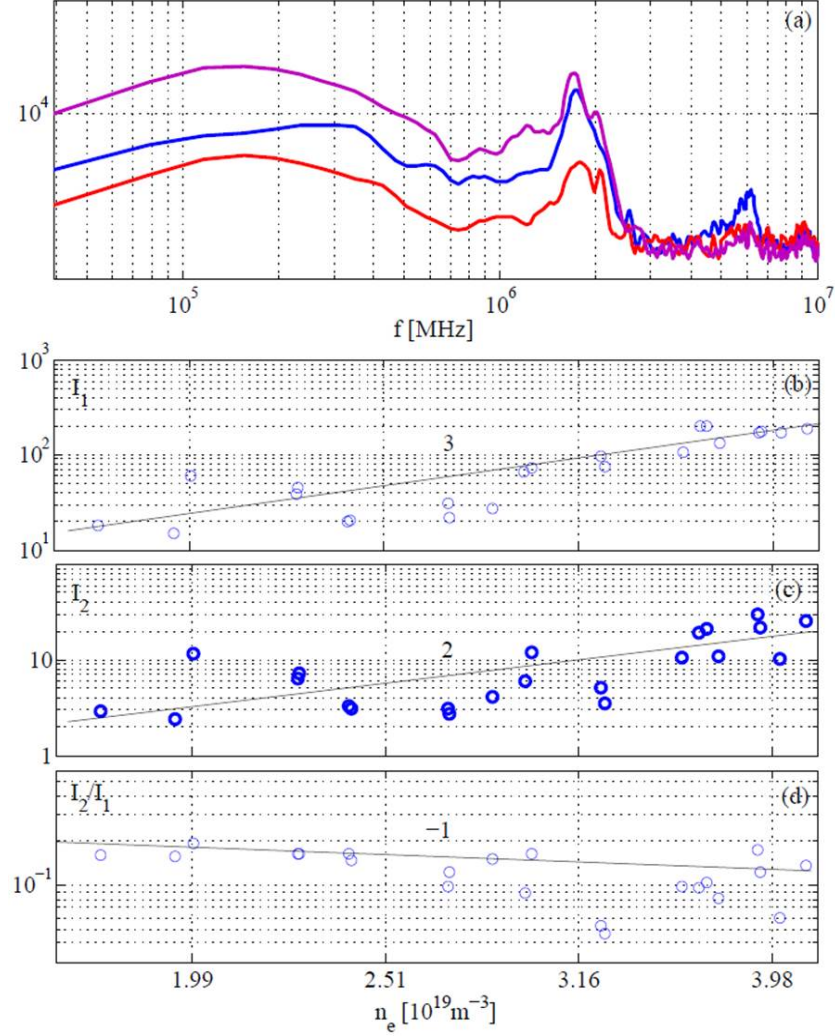


Figure 30: In (a), the power spectrum using DCEDRE for different edge densities in the presence of the LH wave is plotted in frequency range  $0 < f < 10$  MHz. Note the appearance of the coherent mode at 1.7 MHz. (b), (c) and (d) respectively show  $I_1$ : the integration of  $S(f)$  using DFLUC below 1 MHz,  $I_2$ : the integration of  $S(f)$  using DCEDRE 1 and 3 MHz, and  $I_2/I_1$  vs  $n_e$ . We note a higher contribution for turbulence as a function of density.

#### 4. The cross-correlation dependence on the edge density

The cross-correlation coefficient  $Cx_{12}$  shows how turbulent structures are modified as they pass by the two probes which are separated toroidally by a distance  $d = 1$  cm. DFLUC, where the properties of the electrostatic turbulence is investigated, and DCE-

DRE where the properties of the coherent wave at 1.7 MHz are elucidated. We recall that the mean values of  $I_{sat1}$  and  $I_{sat2}$  are set to zero before calculating  $Cx_{12}$ .

In the DFLUC domain, the properties of the cross-correlation are plotted as a function of  $n_{edge}$ . The properties are the  $\tau_0$ ,  $\Delta\tau$  and the cross-correlation maxima  $Max(Cx_{12})$ .  $\tau_0$  appears to be rather unchanged around  $\sim -0.15 \mu s$ . Recall that the distance between the two probes is 1 cm, hence we can calculate the toroidal velocity to be about 67 km/s.

The full width  $\Delta\tau$  estimated at  $Max(Cx_{12})/e$  is shown in Fig. 25(f) where it shows also an unchanged behavior at about  $10 \mu s$ . This almost unchanged behavior agrees with  $\tau_0$ . The unchanged values of  $\Delta\tau$  and  $\tau_0$  reflects no changes in the toroidal velocities of the structures in terms of the edge density.

In Fig. 25(g) we plot the maximum values of  $Cx_{12}$ . It is clear that there are no clear changes detected for the amplitudes. This behavior is in agreement with the results of  $\Delta\tau$  and  $\tau_0$  indicating that no clear modification on the amplitudes is occurring.

In order to understand the properties of the coherent mode that appeared in  $S(f)$  at 1.7 MHz, we plot  $Cx_{12}$  and its properties in Fig. 26. Due to instrumental noise, we filter the signal around 1.7 MHz for the frequency range 1-3 MHz then we plot  $Cx_{12}$  and its properties as a function of  $n_{edge}$ . As mentioned in section 4., the major dramatic feature in Fig. 26(a) is the wave structure of  $Cx_{12}$ . As the coherent mode is at 1.7 MHz, *i.e.*, in the 1-3 MHz range, then this wave form reflects the nature of the coherent mode to be a wave. However, no oscillations are detected for  $f < 1$  MHz as can be noticed in Fig. 25(a).

On the other hand, the negative shifts in the time delay  $\tau_0$  is a major issue in identifying the properties of this mode. It reflects the average time taken by the structure to move from one probe to another caused by either the toroidal or poloidal motion. Fig. 26(d) shows  $\tau_0$  vs.  $n_{edge}$  where it remains unchanged at roughly  $-0.075$  same as the power scan. This will also lead to average toroidal velocities  $u_0 = d/\tau_0 \simeq 1.3 \times 10^5$  m/s. Thus, we can calculate the wavelength at  $f_s = 1.7$  MHz where  $\lambda_s = u_0/f_s \simeq 7.7$  cm.



Same results for the density scan as those of the power scan gives clear indications that the detected mode is an ion sound wave. The detected speed is in the range of the ion sound speed  $1.3 \times 10^5$  m/s. Besides, the calculated wavelength is also in the range of the ion sound wavelength range 6-10 cm, which is about 7.7 cm. Fig. 25(e) shows an almost unchanged  $Cx_{12}$  maxima reflecting same contribution of the detected wave over the density range.

## CHAPTER V

### CONCLUSION

Complicated dynamics are involved in the edge region of magnetically confined plasmas. These dynamics act on a wide range of temporal as well as spatial scales and control the confinement properties of fusion devices. Consequently, understanding the properties of this region is crucial and, as a result, it is so important to approach the problem using various techniques. In this thesis, we study the effect of the lower hybrid waves on the SOL turbulence of the Tore Supra tokamak. Experimental data obtained by fixed Langmuir probes at the edge of the plasma are processed using several statistical tools in order to understand the underlying phenomena occurring in the SOL under the effect of the LH waves.

Chapter 2 introduces the various statistical tools used in analyzing the ion saturation current data  $I_{sat}$ . It presents the information gained from the probability density function (PDF) and its moments, the power spectrum and the cross-correlation. The characterization of the signals allow us to link the data to the physics processes which lead to radial transport. Electrostatic turbulent fluctuations were investigated using DFLUC acquisition frequency range ( $f < 0.5$  MHz), while DCEDRE allowed the study of high frequency fluctuations ( $0.1 < f < 100$  MHz).

In chapter 3, we introduce some key features of the lower hybrid waves and their properties. Several concepts concerning the lower hybrid waves are discussed in this chapter.

**The results that were obtained are new and never obtained before.** Thus they are presented, in chapter 4, as a journal article that is considered for publication. Two parametric dependence studies were done for the data of the ion saturation current,

the LH power scan and the density scan.

The level of fluctuations increases with increasing power according to  $P_T^{0.5}$  reflecting higher radial transport. The normalized level of turbulent fluctuations on the other hand presented no change with increasing LH power. More data analysis is needed to identify the reason behind the increase in the average value of  $I_{sat}$ . The results of the PDF and its moments assess that as the LH power increases, the radial transport is more dominated by diffusive transport rather than convective one. The power spectrum and the cross-correlation analysis show that the average velocities of these turbulent fluctuations are enhanced while their spatial scales remain unchanged.

The particle confinement time is given by  $\tau_p = N_e / \int \nabla \cdot \Gamma(r) dv$ , where  $N_e$  is the total number of plasma electrons and  $\Gamma$  is the radial transport flux. Thus the higher radial transport reflects less particle confinement time.

The density scan for electrostatic turbulent fluctuations detects a higher level of fluctuations than the power scan which was found to increase with the edge density as  $n_{edge}^{1.5}$ . Nevertheless, the level of turbulence remained unchanged. Moreover, it was proven that the radial transport is more dominated by the convective transport unlike the power scan. The power spectrum and the cross-correlation show no modifications on the average velocities or the spatial scales of the turbulent structures.

This increase in the radial transport leads to less confinement with lower particle confinement times  $\tau_p$ .

For high frequency fluctuations, it was shown on the Tore Supra tokamak that the ion cyclotron resonance heating (ICRH) undergo a parametric decay instability that excites ion sound quasi-modes at 1.7 MHz [65]. In this thesis, the existence of the ion sound quasi-modes was confirmed when LH waves interact with SOL turbulence. Moreover, the characteristics of the detected signal, the wavelength and the velocity, assess that the mode is an ion sound quasi-mode where the calculated values fall within the range of the ion sound waves.

We vouch that the origin of this mode is the parametric decay instability. The dependence of the mode on power and density is respectively  $P_T^2$ . This quadratic dependence assures that these waves result from a non-linear instability of the LH wave by Parametric Decay Instability. The relative behavior of the quasi-ion sound mode with respect to the electrostatic fluctuations shows that as a function of power, the mode dominates the fluctuations for higher LH powers. However, electrostatic turbulence dominates the quasi-mode as a function of the edge density since it increases according to  $n_{edge}^3$ .

In conclusion, we confirm that the LH waves undergo a PDI which excites an ion sound quasi-mode at 1.7 MHz when coupled to the SOL turbulence. More is to be done on the properties of these waves generated by the LH waves and the possible link with different phenomena that might occur in the SOL. The amplitude of the mode is also to be considered as where two spikes appear in the frequency spectrum. Furthermore, more data analysis is needed to identify the mechanism responsible for the increase in the average value of  $I_{sat}$  vs. power.

## Appendix

### A. Qualitative theory and principle features of the PDI

We shall proceed by the qualitative analysis described in Ref. [31] of the PDI to understand the physical aspects of such types of instabilities. In oscillatory systems, parametric instabilities are described by the so-called Mathieu equation. It is usually written in the form:

$$\ddot{x} + \omega^2[1 + \varepsilon \cos(\omega_0 t)]x = 0 \quad (104)$$

A natural and simple generalization of this equation to a wave-sustaining media is the equation:

$$\frac{\partial^2 u}{\partial t^2} - V_\Phi [1 + \varepsilon \cos(\omega_0 t)] \frac{\partial^2 u}{\partial x^2} + \hat{\alpha}u = 0 \quad (105)$$

where  $\hat{\alpha}u$  is the linear operator describing the deviation of the wave dispersion. This operator comes from the linear law  $\omega = kV_\Phi$ . In the absence of a term that is proportional to  $\varepsilon$ , equations having the form of equation (105) describe linear properties of waves. For instance, they describe linear properties of acoustic waves in gas dynamics, or magneto-acoustic and Alfvén waves in magnetohydrodynamics. For example, the equations of gas dynamics (including the gas dynamics of isotropic plasma) are:

$$\left\{ \begin{array}{l} \frac{\partial \rho}{\partial t} + \rho_0 \frac{\partial u}{\partial t} = 0 \\ \rho_0 \frac{\partial u}{\partial t} = -\frac{\partial p}{\partial x} \\ \frac{p}{\rho^\gamma} = cte \end{array} \right. \quad (106)$$

where  $\rho$ ,  $u$  and  $p$  are the density, the mass velocity and the pressure respectively.  $\gamma$  is the exponent of the adiabatic curve, while the 0 subscript reflects the undisturbed (Basic) quantities

Hence, the one dimensional approximation of these equations gives:

$$\frac{\partial^2 u}{\partial t^2} - V_{\Phi^2} \frac{\partial^2 u}{\partial x^2} = 0 \quad (107)$$

where

$$V_{\Phi^2} = c_s^2 \equiv \gamma \frac{P_0}{\rho_0} \quad (108)$$

$c_s$  being the speed of sound.

Now, we will focus our study on the low-amplitude Alfven waves. The flow is considered incompressible and hence,  $\nabla \cdot \mathbf{V} = 0$ . Denote by  $\mathbf{h}$  the magnetic field of the wave that propagates in a constant magnetic field  $\mathbf{H}_0$ . We use the following equations:

$$\frac{\partial \mathbf{u}}{\partial t} = \left( \frac{1}{4\pi\rho_0} \right) [\nabla \times \mathbf{h}, \mathbf{H}_0] \quad (109)$$

$$\frac{\partial \mathbf{h}}{\partial t} = \nabla \times [\mathbf{u}, \mathbf{H}_0] \quad (110)$$

From these equations we obtain the following equations:

$$\frac{\partial^2 u}{\partial t^2} - V_{\Phi^2} \frac{\partial^2 u}{\partial x^2} = 0 \quad V_{\Phi^2} = V_A^2 = \frac{H_0^2}{4\pi\rho_0} \quad (111)$$

The  $x$  points presented here are along  $\mathbf{H}_0$  and  $u$  denotes any component of the mass velocity which is perpendicular to  $\mathbf{H}_0$ .

Assume that we have adjusted the density of the medium, the pump wave, by low-amplitude sine wave. Hence we have:

$$c_s^2 = c_{s0}^2 [1 + \epsilon \cos(\omega_0 t - k_0 x)] \quad (112)$$

$$V_A^2 = V_{A0}^2 [1 + \epsilon \cos(\omega_0 t - k_0 x)] \quad (113)$$

$$\varepsilon = \frac{-\delta\rho_0}{\rho_0} \quad (114)$$

where  $\delta\rho_0$  is the amplitude of the pump wave. If we substitute equations (112), (113) and (114) into equations (109), (110) and (111), then we will return to an equation of the same form as equation (105).

Note that if the equations for acoustic or Alfvén waves in media with wave modulation are strictly deduced, then additional terms will obviously appear to describe the whole frame. These terms involve different types of non-linearities. Besides, this will not change the principle conclusions of the presented qualitative analysis.

We start by equation (105). The following will be an example that will illustrate how the parametric coupling arises in a wave doublet of quantities  $(\omega_1, \mathbf{k}_1; \omega_2, \mathbf{k}_2)$  that is described by equation (105). In the absence of the pump wave, i.e.  $\varepsilon=0$ , equation (105) describes plane waves obeying the dispersion relation  $\omega(k) = kV_\Phi + \alpha(k)$ , where  $\alpha(k)$  contributes to the frequency due to the terms generated by the operator in equation (105).

Now, we investigate the parametric coupling of the waves due to the pump wave background. We apply Fourier transforms to spatial variables,  $V_k = \int u(x) \exp(ikx) dx$ , and then we separate the pump wave term. The final result is shown in the following equation:

$$\frac{d^2 V_{k_1}}{dt^2} + \omega^2(k_1) V_{k_1} = \left(\frac{\varepsilon}{2}\right) (k_0 - k_1)^2 V^2_{\Phi_0} V_{k_0 - k_1}^* e^{-i\omega_0 t} - \left(\frac{\varepsilon}{2}\right) (k_0 + k_1)^2 V^2_{\Phi_0} V_{k_0 + k_1}^* e^{-i\omega_0 t} \quad (115)$$

Equation (115) is a set of equations representing the coupled oscillators. According to Oraevsky, if we take into consideration the smallness of the parameter  $\varepsilon$ , this equation can be truncated. For the zeroth approximation of  $\varepsilon$ ,  $V_k$  oscillates in time with eigen frequencies  $\omega(k)$ . For ordinary non-resonant conditions, the wave dynamics is in-



fluenced slightly by a weak coupling. However, if the driving force in the RHS of the equation happens to be in resonance with an eigen frequency, the oscillator may switch to the excitation mode.

For the first term, the resonance condition is

$$\omega_0 - \omega(k_0 - k_1) = \omega(k_1)$$

. While for the second term it is

$$\omega_0 - \omega(k_0 + k_1) = \omega(k_1)$$

It is obvious that the first condition holds. The second term represents the non-resonant term, hence it can be dropped. Note that the degeneration is possible sometimes with both conditions satisfied. Such cases were treated in different papers as in Ref. [71, 72, 73].

As for  $V_{k_1}$  it is described by equation (115). Similarly, for  $V_{k_0-k_1}^*$  it is described by the following equation:

$$\begin{aligned} \frac{d^2 V_{k_0-k_1}^*}{dt^2} + \omega^2(k_0 - k_1)V_{k_0-k_1}^* = & -\left(\frac{\varepsilon}{2}\right)(k_1)^2 V_{\Phi_0}^2 V_{k_1} e^{i\omega_0 t} \\ & - \left(\frac{\varepsilon}{2}\right)(2k_0 - k_1)^2 V_{\Phi_0}^2 V_{2k_0-k_1} e^{-i\omega_0 t} \quad (116) \end{aligned}$$

Note that the second term of this equation is also non-resonant, so we can drop it. Hence, keeping the resonant terms of equations (115) and (116), we reach the following truncated equation for  $V_{k_0-k_1}^*$ :

$$\frac{d^2 V_{k_1}}{dt^2} + \omega^2(k_1) V_{k_1} = \left(\frac{\varepsilon}{2}\right) k_2^2 V_{\Phi_0}^2 e^{(-i\omega_0 t)} V_{k_2}^* \quad (117)$$

$$\frac{d^2 V_{k_2}^*}{dt^2} + \omega^2(k_2) V_{k_2}^* = -\left(\frac{\varepsilon}{2}\right) k_1^2 V_{\Phi_0}^2 e^{(i\omega_0 t)} V_{k_1} \quad (118)$$

where  $k_2 = k_0 - k_1$ . So,  $\omega_0 - \omega(k_2) = \omega(k_1)$  for the right hand side terms to be resonant. Then we can write the decay conditions if we take into account the relation between the vectors:

$$\begin{cases} \omega_0 = \omega(k_1) + \omega(k_2) \\ k_0 = k_1 + k_2 \end{cases} \quad (119)$$

These are the decay conditions, which are the conditions for the phase and frequency matching. The solution can be rewritten according to our previous arguments as follows:

$$V_{k_i} = a_i(t) \exp[-i\omega_i(k_i)t] \quad (120)$$

For slowly varying amplitudes, the equations are:

$$\left\{ \begin{array}{l} -2i\omega_1 \frac{da_1}{dt} = -\left(\frac{\varepsilon}{2}\right)k_2^2 V_{\Phi_0}^2 a_2^* e^{-i\Delta\omega t} \\ 2i\omega_1 \frac{da_2^*}{dt} = -\left(\frac{\varepsilon}{2}\right)k_1^2 V_{\Phi_0}^2 a_1 e^{i\Delta\omega t} \\ \Delta\omega = \omega_0 - \omega_1 - \omega_2 \end{array} \right. \quad (121)$$

Finally, the solution can be written according to our previous arguments as:

$$\left\{ \begin{array}{l} a_1 \sim \exp[-i\frac{\Delta\omega}{2}t + \nu t] \\ a_2^* \sim \exp[i\frac{\Delta\omega}{2}t + \nu t] \\ \nu = \sqrt{\gamma_D^2 - \left(\frac{\Delta\omega}{2}\right)^2} \quad \gamma_D^2 \equiv \frac{\varepsilon^2 k_1^2 k_2^2 V_{\Phi_0}^2}{16\omega_1 \omega_2} \end{array} \right. \quad (122)$$

This solution describes the so-called parametric decay instability. From above equations and when (119) is exactly satisfied, the amplitudes of the  $a_1$  and  $a_2$  waves will grow exponentially with increment  $\nu = \gamma_D$ . The product  $\omega_1 \omega_2$  must then be greater than zero. This leads with the decay conditions (119) to the inequality:

$$\omega_0 > \omega_1, \omega_2$$

It can be deduced from this inequality that the decay instability typically excite lower frequencies. High frequencies are typically excited if degeneracy is considered as in Ref. [71, 72, 73] under these conditions that must be simultaneously satisfied:

$$\begin{cases} \omega_0 - \omega_1 = \omega_2 \\ k_0 - k_1 = k_2 \end{cases} \quad (123)$$

and

$$\begin{cases} \omega_0 + \omega_1 = \omega_3 \\ k_0 + k_1 = k_3 \end{cases} \quad (124)$$

## B. PDI thresholds

We can take into account the wave dissipation and try to find its effect on the PDI. We can do so by a certain method. We introduce small imaginary increments to the natural frequencies. Hence, equations of type (123) and (124) will gain terms  $\omega_i + i\gamma_i$ , where  $\gamma_i$  are the damping decrements for the corresponding waves. Suppose, for simplicity, that  $\Delta\omega = 0$  and performing some mathematical algebra, we reach the PDI increment covering dissipation expression:

$$v_D = -\frac{(\gamma_1 + \gamma_2)}{2} + \sqrt{\gamma_D^2 + \frac{(\gamma_1 - \gamma_2)^2}{4}} \quad (125)$$

This expression gives another expression which stands for the instability threshold:

$$\gamma_{DT}^2 = \gamma_1 \gamma_2 \quad (126)$$

For the above problem formulated with a phase velocity modulation, we can find the modulation amplitude  $\varepsilon$ :

$$\varepsilon_T^2 = \frac{16\omega_1\omega_2\gamma_1\gamma_2}{k_1^2k_2^2V_\Phi^4} \quad (127)$$

Hence, PDI arises when the modulation amplitude  $\varepsilon$  exceeds the value in (127). Moreover, if one of the decrements of the doublet tends to zero, the threshold vanishes.

The whole case discussed in this section till now is for the homogeneous medium approximation and inhomogeneity was considered negligible. In inhomogeneous media, the oscillations drift out of the resonant interaction band, which produces also PDI thresholds.

The frequency is the invariant characteristic for a waves propagating a weakly inhomogeneous medium. From the equation:

$$\omega_i(k_i, x) = \text{constant} \quad (128)$$

we can find the ‘quasi-classical’ value of the wave vector  $k_i$ . With simple modifications of equation (121) from a temporal problem to a spatial problem (see these modifications in Ref. [31]), one can find the spatial increment of the PDI instead of the temporal one as:

$$\kappa^2 = \frac{\gamma_D^2}{(d\omega_1/dk)(d\omega_2/dk)} \quad (129)$$

Now, equation (125) will be replaced by an expression for the spatial PDI increment  $\kappa$ :

$$\kappa = \sqrt{\kappa_D^2 - \left(\frac{\Delta k}{2}\right)^2} \quad (130)$$

where this equation will allow us to solve the wave amplification problem in the interaction band. This problem is determined by the formula  $\Gamma \approx k\Delta x_0$ . We need to calculate the length of the interaction zone with an amplification  $\Delta x_0$ . From equation (130),  $\kappa = 0$  when  $\kappa_D = \frac{\Delta k}{2}$ , where  $\Delta k = \frac{d}{dx}(k_0 - k_1 - k_2)\Delta x_0$ . Hence, simple calculations can lead to:

$$\Delta x_0 \approx 2\gamma_D / \frac{d}{dx}(k_0 - k_1 - k_2) \sqrt{\frac{d\omega_1}{dk} \frac{d\omega_2}{dk}} \quad (131)$$

or for  $\Gamma$ :

$$\Gamma \approx 2\gamma_D^2 / \frac{d\omega_1}{dk} \frac{d\omega_2}{dk} \frac{d}{dx}(k_0 - k_1 - k_2) \quad (132)$$

## BIBLIOGRAPHY

- [1] [www.nuclearfusion.20m.com](http://www.nuclearfusion.20m.com).
- [2] John Wesson. *Tokamaks*, volume 149. Oxford University Press, 2011.
- [3] D Biskamp. *Nonlinear magnetohydrodynamics*, 1993.
- [4] F. Wagner, G. Becker, K. Behringer, D. Campbell, A. Eberhagen, W. Engelhardt, G. Fussmann, O. Gehre, J. Gernhardt, G. v. Gierke, G. Haas, M. Huang, F. Karger, M. Keilhacker, O. Klüber, M. Kornherr, K. Lackner, G. Lisitano, G. G. Lister, H. M. Mayer, D. Meisel, E. R. Müller, H. Murmann, H. Niedermeyer, W. Poschenrieder, H. Rapp, H. Röhr, F. Schneider, G. Siller, E. Speth, A. Stäbler, K. H. Steuer, G. Venus, O. Vollmer, and Z. Yü. Regime of improved confinement and high beta in neutral-beam-heated divertor discharges of the asdex tokamak. *Phys. Rev. Lett.*, 49:1408–1412, Nov 1982.
- [5] [www-fusion magnetique.cea.fr](http://www-fusion.magnetique.cea.fr).
- [6] Richard O Dendy. *Plasma dynamics*. Clarendon Press Oxford, 1990.
- [7] Joseph Michael Dewhurst. *Statistical description and modelling of fusion plasma edge turbulence*. PhD thesis, University of Warwick, 2010.
- [8] Robert J Goldston and Paul Harding Rutherford. *Introduction to plasma physics*, volume 1. CRC Press, 1995.

- [9] G. Y. Antar. Kolmogorov-kraichnan scaling in the inverse energy cascade of two-dimensional plasma turbulence. *Phys. Rev. Lett.*, 91:055002, Aug 2003.
- [10] GY Antar, M Goniche, A Ekedahl, and L Colas. The role of power and magnetic connection to the active antenna in the suppression of intermittent structures by ion cyclotron resonance heating. *Nuclear Fusion*, 52(10):103005, 2012.
- [11] B. LaBombard, R. L. Boivin, M. Greenwald, J. Hughes, B. Lipschultz, D. Mossessian, C. S. Pitcher, J. L. Terry, S. J. Zweben, and Alcator Group. Particle transport in the scrape-off layer and its relationship to discharge density limit in alcator c-mod. *Physics of Plasmas (1994-present)*, 8(5):2107–2117, 2001.
- [12] R Dux and AG Peeters. Neoclassical impurity transport in the core of an ignited tokamak plasma. *Nuclear fusion*, 40(10):1721, 2000.
- [13] SJ Zweben, JA Boedo, O Grulke, C Hidalgo, B LaBombard, RJ Maqueda, P Scarin, and JL Terry. Edge turbulence measurements in toroidal fusion devices. *Plasma Physics and Controlled Fusion*, 49(7):S1, 2007.
- [14] JP Graves, J Horacek, RA Pitts, and KI Hopcraft. Self-similar density turbulence in the tcv tokamak scrape-off layer. *Plasma physics and controlled fusion*, 47(3):L1, 2005.
- [15] YH Xu, S Jachmich, RR Weynants, et al. On the properties of turbulence intermittency in the boundary of the textor tokamak. *Plasma physics and controlled fusion*, 47(10):1841, 2005.
- [16] Kevin P Balanda and HL MacGillivray. Kurtosis: a critical review. *The American Statistician*, 42(2):111–119, 1988.
- [17] GY Antar, SI Krasheninnikov, P Devynck, RP Doerner, EM Hollmann, JA Boedo, SC Luckhardt, and RW Conn. Experimental evidence of intermittent convection in



- the edge of magnetic confinement devices. *Physical review letters*, 87(6):065001, 2001.
- [18] G. Antar, P. Devynck, and G. D. Wang. Response to “comment on ‘the hurst exponent and long time correlation’” [phys. plasmas 7, 5267 (2000)]. *Physics of Plasmas (1994-present)*, 7(12):5269–5271, 2000.
- [19] Suwon Cho and DG Swanson. Dispersion relations for the lower hybrid frequency range. *Physics of Fluids (1958-1988)*, 31(5):1123–1129, 1988.
- [20] A Ekedahl, Yu F Baranov, JA Dobbing, B Fischer, C Gormezano, TTC Jones, M Lennholm, VV Parail, FG Rimini, JA Romero, et al. Profile control experiments in jet using off-axis lower hybrid current drive. *Nuclear fusion*, 38(9):1397, 1998.
- [21] Karin Rantamäki et al. *Particle-in-cell simulations of the near-field of a lower hybrid grill*. VTT Technical Research Centre of Finland, 2003.
- [22] C Gormezano, P Briand, G Briffod, GT Hoang, TK N’guyen, D Moreau, and G Ray. Lower-hybrid plasma heating via a new launcher—the multijunction grill. *Nuclear fusion*, 25(4):419, 1985.
- [23] M Preynas, M Goniche, J Hillairet, X Litaudon, A Ekedahl, and L Colas. Experimental characterization and modelling of non-linear coupling of the lower hybrid current drive power on tore supra. *Nuclear Fusion*, 53(1):013012, 2013.
- [24] Ph Bibet, TK Nguyen, J Achard, G Berger-By, S Berio, M Goniche, G Rey, and G Tonon. Experimental and theoretical results concerning the development of the main rf components for next tore supra lhcd antennae. In *Fusion technology 1994. Proceedings. Vol. 1*. 1995.
- [25] P Froissard, G REY, P BIBET, G BOSIA, L BRUNO, M GONICHE, F KAZARIAN, S KUZIKOV, C PORTAFAIX, G TONON, et al. Lower hybrid heating and

- current drive design for iter and application for present tokamaks. In *SOFT: Symposium on fusion technology*, 1998.
- [26] Ph Bibet and F Mirizzi. Report on iter feat lhcd launcher. *Contract FU05-CT*, 19, 2001.
- [27] V Fuchs, M Goniche, Y Demers, P Jacquet, and J Mailloux. Acceleration of electrons in the vicinity of a lower hybrid waveguide array. *Physics of Plasmas (1994-present)*, 3(11):4023–4035, 1996.
- [28] Xavier Litaudon. *Etude théorique et expérimentale du couplage de l'onde hybride dans Tore-Supra et jet au moyen d'antennes à multijonctions*. PhD thesis, 1990.
- [29] CS Liu and VK Tripathi. Parametric instabilities in a magnetized plasma. *Physics Reports*, 130(3):143–216, 1986.
- [30] Oraevsky V N and Sagdeev R Z. *Sov. Phys.-Tech. Phys.*, 7, 1962.
- [31] SS Moiseev, Victor N Oraevsky, and VG Pungin. *Non-Linear Instabilities in Plasmas and Hydrodynamics*, volume 5. CRC Press, 1999.
- [32] Norman M Kroll. Parametric amplification in spatially extended media and application to the design of tuneable oscillators at optical frequencies. *Physical Review*, 127(4):1207, 1962.
- [33] EJ Woodbury and WK Ng. Ruby laser operation in near ir, 1962.
- [34] LA Artsimovich and RZ Sagdeev. *Fizika plazmy dlya fizikov*. 1979.
- [35] Miklos Porkolab. Theory of parametric instability near the lower hybrid frequency. *Physics of Fluids (1958-1988)*, 17(7):1432–1442, 1974.
- [36] AA Galeev and RZ Sagdeev. Parametric phenomena in a plasma. *Nuclear Fusion*, 13(4):603, 1973.

- [37] Yuichi Takase and Miklos Porkolab. Parametric excitation of ion sound quasi-modes during lower hybrid heating experiments in tokamaks. *Physics of Fluids (1958-1988)*, 26(10):2992–3003, 1983.
- [38] SL Musher, AM Rubenchik, and BI Sturman. Collective effects associated with lower hybrid heating of plasma. *Plasma Physics*, 20(11):1131, 1978.
- [39] KD Harms, G Hasselberg, and A Rogister. Excitation of electrostatic plasma turbulence by a magneto-acoustic wave. *Nuclear Fusion*, 14(2):251, 1974.
- [40] Aihui Zhao and Zhe Gao. Parameter study of parametric instabilities during lower hybrid wave injection into tokamaks. *Nuclear Fusion*, 53(8):083015, 2013.
- [41] Liu Chen. Plasma heating by induced scattering of magnetosonic waves. *Nuclear Fusion*, 16(3):509, 1976.
- [42] V Fiala and VI Sotnikov. Parametric excitation of lower hybrid waves in the vicinity of the resonance cone. *Plasma physics and controlled fusion*, 27(3):321, 1985.
- [43] M Sugawa, R Sugaya, and H Nomoto. Parametric instabilities at unstable electrostatic ion cyclotron waves in an ion beam-plasma system. *Physics Letters A*, 68(5):439–441, 1978.
- [44] R Cesario and A Cardinali. Parametric instabilities excited by ion sound and ion cyclotron quasi-modes during lower hybrid heating of tokamak plasmas. *Nuclear fusion*, 29(10):1709, 1989.
- [45] R Cesario and V Pericoli-Ridolfini. Study of the parametric instabilities in the lower hybrid frequency range in the ft tokamak. *Nuclear Fusion*, 27(3):435, 1987.
- [46] R Cesario, R Bartiromo, A Cardinali, F Paoletti, V Pericoli-Ridolfini, and R Schubert. Density fluctuations and spectral broadening during the lower hybrid current drive experiment on asdex. *Nuclear fusion*, 32(12):2127, 1992.

- [47] R Cesario, A Cardinali, C Castaldo, F Paoletti, W Fundamenski, S Hacquin, et al. Spectral broadening of lower hybrid waves produced by parametric instability in current drive experiments of tokamak plasmas. *Nuclear fusion*, 46(4):462, 2006.
- [48] R Cesario, L Amicucci, A Cardinali, C Castaldo, M Marinucci, F Napoli, F Paoletti, D De Arcangelis, M Ferrari, A Galli, et al. Spectral broadening of parametric instability in lower hybrid current drive at a high density. *Nuclear Fusion*, 54(4):043002, 2014.
- [49] SG Baek, RR Parker, S Shiraiwa, GM Wallace, PT Bonoli, D Brunner, IC Faust, AE Hubbard, B LaBombard, and M Porkolab. Measurements of ion cyclotron parametric decay of lower hybrid waves at the high-field side of alcator c-mod. *Plasma Physics and Controlled Fusion*, 55(5):052001, 2013.
- [50] Nathaniel J Fisch. Confining a tokamak plasma with rf-driven currents. *Physical Review Letters*, 41:873–876, 1978.
- [51] Stefano Bernabei, C Daughney, P Efthimion, W Hooke, J Hosea, F Jobs, A Martin, E Mazzucato, E Meservey, R Motley, et al. Lower-hybrid current drive in the plt tokamak. *Physical Review Letters*, 49(17):1255, 1982.
- [52] Nathaniel J Fisch. Theory of current drive in plasmas. *Reviews of Modern Physics*, 59(1):175, 1987.
- [53] Marshall N Rosenbluth. *New Ideas in Tokamaks Confinement*. Springer, 1994.
- [54] Y Peysson and Tore Supra Team. High power lower hybrid current drive experiments in the tore supra tokamak. *Nuclear fusion*, 41(11):1703, 2001.
- [55] L Chen and RL Berger. Spatial depletion of the lower hybrid cone through parametric decay. *Nuclear Fusion*, 17(4):779, 1977.
- [56] V. K. Tripathi, C. S. Liu, and C. Grebogi. Parametric decay of lower hybrid waves in

- a plasma: Effect of ion nonlinearity. *Physics of Fluids (1958-1988)*, 22(2):301–309, 1979.
- [57] R Cesario, F De Marco, A Cardinali, and M Brambilla. Rf sheath formation and plasma density rise during the ion Bernstein wave heating experiment of tokamak plasmas. *Nuclear fusion*, 34(11):1527, 1994.
- [58] R Cesario, A Cardinali, C Castaldo, F Paoletti, and D Mazon. Modeling of a lower-hybrid current drive by including spectral broadening induced by parametric instability in tokamak plasmas. *Physical review letters*, 92(17):175002, 2004.
- [59] PN Yushmanov, T Takizuka, KS Riedel, OJWF Kardaun, JG Cordey, SM Kaye, and DE Post. Scalings for tokamak energy confinement. *Nuclear Fusion*, 30(10):1999, 1990.
- [60] V.P. Ridolfini. Effect of lower hybrid waves on turbulence and transport of particles and energy in the FTU tokamak scrape-off layer plasma. *Plasma Physics and Controlled Fusion*, 53(11):115001, 2011.
- [61] M Goniche, V Basiuk, J Decker, PK Sharma, G Antar, G Berger-By, F Clairet, L Delpech, Annika Ekedahl, J Gunn, et al. Lower hybrid current drive at high density on Tore Supra. *Nuclear Fusion*, 53(3):033010, 2013.
- [62] T Oosako, A Ekedahl, M Goniche, J Achard, J Decker, Y Peysson, et al. Characterisation of SOL density fluctuations in front of the LHCD PAM launcher in Tore. In *RADIO FREQUENCY POWER IN PLASMAS: Proceedings of the 19th Topical Conference*, volume 1406, pages 239–242. AIP Publishing, 2011.
- [63] G Y Antar, M Tsalias, E Wolfrum, V Rohde, and the ASDEX Upgrade Team. Turbulence during h- and l-mode plasmas in the scrape-off layer of the ASDEX Upgrade tokamak. *Plasma Physics and Controlled Fusion*, 50(9):095012, 2008.

- [64] V Pericoli Ridolfini, ML Apicella, G Calabrò, C Cianfarani, E Giovannozzi, and L Panaccione. Lower hybrid current drive efficiency in tokamaks and wave scattering by density fluctuations at the plasma edge. *Nuclear Fusion*, 51(11):113023, 2011.
- [65] G Antar, M Goniche, A Ekedahl, and L Colas. On the interaction between the ion cyclotron resonance heating and scrape-off layer turbulence via coherent waves. *Nuclear Fusion*, 54(8):083018, 2014.
- [66] C Fenzi, X Garbet, E Trier, P Hennequin, C Bourdelle, T Aniel, G Colledani, P Devynck, C Gil, Ö Gürçan, et al. On plasma rotation with toroidal magnetic field ripple and no external momentum input. *Nuclear Fusion*, 51(10):103038, 2011.
- [67] G. Antar, G. T. Hoang, P. Devynck, X. Garbet, C. Laviron, and M. Goniche. Turbulence reduction and poloidal shear steepening in reversed shear plasmas investigated by light scattering. *Phys. Plasmas*, 8:186, 2001.
- [68] GY Antar, P Devynck, X Garbet, and SC Luckhardt. Turbulence intermittency and burst properties in tokamak scrape-off layer. *Physics of Plasmas (1994-present)*, 8(5):1612–1624, 2001.
- [69] RMO Galvão, G Gnani, L Comberoff, and FT Gratton. Decay of the ion-cyclotron instability in magnetized plasmas with thermally anisotropic minority ions. *Plasma physics and controlled fusion*, 36(10):1679, 1994.
- [70] GY Antar, G Counsell, and J-W Ahn. On the scaling of avaloids and turbulence with the average density approaching the density limit. *Physics of Plasmas (1994-present)*, 12(8):082503, 2005.
- [71] Karpliuk K. S. and Oraevsky V. N. *Pisma. JETP*, 5, 1967.
- [72] Oraevsky V. N. and Tsytovich V. N. *Zh. Exp. Teor. Fiz.*, 53, 1967.
- [73] Oraevsky V N and Pavlenko V P. *Zh. Tekhn. Fiz.*, 39, 1969.

